Doctoral Thesis

Development of High Strength and Corrosion Resistant Magnesium Alloys Using Severe Plastic Deformation Process

February 2018

Graduate School of Seoul National University

Materials Science and Engineering

Bahmani, Ahmad

Development of High Strength and Corrosion Resistant Magnesium Alloys Using Severe Plastic Deformation Process

Academic Advisor: Prof. Shin, Kwang Seon

Submitting a doctoral thesis of materials science and engineering

February 2018

Graduate School of Seoul National University

Department of Materials Science and Engineering

Bahmani, Ahmad

Confirming the doctoral thesis written by Bahmani, Ahmad

December 2017

Chair	**Han, Heung Nam**	(Seal)
Vice Chair	**Shin, Kwang Seon**	(Seal)
Examiner	**Kim, Woo Jin**	(Seal)
Examiner	**Hong, Seong Hyeon**	(Seal)
Examiner	**Lee, Kyung Hoon**	(Seal)

Abstract

In the present work, several Mg alloys as well as pure Mg were produced through different processes including casting, extrusion, screw rolling (SR) and multi directional forging (MDF). The mechanical properties and corrosion behavior of the extruded materials were studied and materials with the best mechanical properties and corrosion behavior were subjected to the SR and MDF. The related processing conditions of SR and MDF were changed and mechanical properties and corrosion behavior of the produced materials were analyzed.

The microstructure was characterized by optical microscopy (OM), x-ray diffraction (XRD) and scanning electron microscope (SEM). The mechanical properties including tensile and compression properties were measured using a R&B, an Instron universal testing system and hardness vickers. The electrochemical, hydrogen evolution and mass loss techniques in a 3.5 wt. % NaCl solution saturated with $Mg(OH)_2$ were used for corrosion studies. Moreover, the scanning kelvin probe force microscopy (SKPFM) was utilized to measure the volta-potential of the matrix and various intermetallic phases.

ZAXM4211 alloy was subjected to both processes of SR and MDF at different temperatures. It was observed that increasing the screw rolling temperature from 220 to 340 ^{o}C results in decreasing the yield strength, while it results in decreasing the corrosion rate up to 300 ^{o}C and increasing it from 300 to 340 ^{o}C. Moreover, it was observed that increasing the screw rolling temperature results in the dissolution of intermetallics and increase in the grain size.

Then, several alloys like ZAXM4211, XM11, ZAXM4411, ZTXM4411 were also subjected to MDF at different temperatures and same trend as SR were obtained. It was also confirmed from the MDF results that, both the mechanical and corrosion properties were improved after MDF. However, increase in MDF temperature decreased the yield strength and increased the corrosion resistance. Yield strength reduction at higher temperatures is due to increase in grain size while corrosion rate

behavior is under control of two parameters including reduction of second phases (galvanic cells) and grain size. A very low corrosion rate material was obtained from XM11 alloy MDFed at 300^{o}C. The corrosion rate of this material was 0.26 mm/y which is even less than that of high purity Mg (0.39 mm/y).

Finally to understand the corrosion rate improvement, all the corrosion rate data which was obtained in this study as well as some available literature were quantitatively analyzed and an experimental formula was proposed to model the corrosion rate using the microstructure parameters. These parameters were related to the composition, grain size, and area fraction of the second phases and volta-potential difference of the second phase relative to the matrix. The experimental data was in a good agreement with the data of the proposed model.

Key words: magnesium alloys, mechanical properties, corrosion behavior, corrosion rate, multi-directional forging, screw rolling, scanning kelvin probe force microscopy, grain size.

Contents

Figures

Tables

Chapter 1: Introduction

Magnesium alloys are very attractive structural materials for biomedical applications, light-weight vehicles and electronic devices due to their high strength-to-weight ratio. Fuel consumption can be decreased by application of Mg alloys in automobiles through lightening the weight. Mg alloys are also interesting as promising biodegradable implants for using in the human body. However, the poor corrosion resistance of Mg alloys limits their wide-spread applications. It is therefore, necessary to understand the important factors to control it, and identify better ways to improve its performance [1-5]. There are two main reasons for their poor corrosion resistance which includes firstly the internal galvanic corrosion caused by second phases, defects or impurities and secondly the quasi passive hydroxide film formed on Mg which is much less stable than the passive films which form on aluminum, titanium and stainless steels [6]. High purity Mg shows the lowest corrosion rate regarding galvanic corrosions [7], but its usage is limited in medical implants due to its low mechanical strength and poor ductility attributed to its hexagonal crystal structure [8, 9]. None of the studied Mg alloys has adequate corrosion resistance in NaCl containing solutions, and no practical alloy has been produced with a corrosion rate in 3.5 wt.% NaCl lower than that of high-purity Mg [10].

Mg alloy components are usually produced by various casting processes. However, wrought alloys are also used in numerous applications. Casting alloys may produce several defects during solidification such as micro- and macro-porosities, double oxide films [11-14] which can be eliminated after deformation process. Recently, there has been growing interest in the automotive industry in looking at potential applications wrought Mg alloys. Wrought Mg alloys have specific advantages, which limit casting defects and hence improving mechanical properties. Nevertheless, these technologies in Mg are considered to be extremely underdeveloped due to lack of suitable alloys and some technological restrictions

imposed by the hexagonal crystal structure of Mg. Therefore, more researches need to be carried out both on alloy development and production technology improvement [15].

There are several microstructural parameters that influence the mechanical and corrosion properties of materials, like composition, lattice defects, orientation, grain size, secondary phases, and so on. Here these parameters have been classified their effects on the materials properties including corrosion and mechanical properties have been explained. Finally an equation has been derived for the first time to predict the corrosion rate using microstructural parameters.

1.1 Effect of alloying elements

In order to develop a new alloy, the role of each alloying element should be considered. Alloying elements are considerably effect on all properties of Mg and their role is very complicated [16]. These days, three elements including Al, Zn, and Sn are widely used in magnesium alloys due to their proper solubility and capability of precipitate hardening [3-5]. Mn has the function of refining the grain size and improving tensile strength of magnesium alloys [17-21]. It has been mentioned that fine particles did lead to a much reduced recrystallized fraction after hot rolling, attributed to a retardation of static recrystallization kinetics. Mn also decreases the corrosion rate of Mg via transforming iron and other impurity elements to the harmless intermetallic compounds. Mn can increase the tolerance limit of Fe contents but some other alloying elements like Al decreases it [22, 23] Moreover, it has been mentioned that Mn can enhance the stability of the surface layer and hence improve the corrosion rate [24].

Ca has a low density (1.55 g/cm3), which endues the Mg-Ca alloy system with the advantage of similar density to bone. According to the Mg-Ca binary phase diagram, the maximum solubility of Ca in Mg at 516.5 K is 1.34 wt.% [25]. The addition of Ca has been found to improve the creep resistance [26]. Bakhsheshi Rad [27, 28] reported the role of the secondary phases in Mg–0.5Ca–xZn alloys. According to their report, the addition of Zn content up to 1 wt. % decreases the

corrosion rate whilst further addition of Zn up to 9% reversed the effect. Moreover, Zhang [29] reported that addition of Ca up to 0.38 wt.% decreased the degradation rate of the Mg-2Zn-0.2Mn alloy immersed in SBF by forming a dense passivation layer while increasing the Ca content to 0.76 and 1.10 wt% increased the degradation rate due to increasing the fraction of second phases.

Sn has low melting point and it is a comparatively economical metal to use. Furthermore, Sn has a reputation of enhancing castability and is beneficial to providing corrosion resistance as well. The Mg–Sn system has a relatively high solubility limit at 561 ^{o}C and a low solubility at ambient temperature [3]. Adding alloying elements to enhance the age hardening response of Mg–Sn system alloys has been studied extensively [30]. Furthermore, the corrosion behavior of Mg–Sn system is influenced by the phases present in these alloys, with Mg_2Sn being the most compatible followed by $Ca_2{-}yMg_xSn$ and finally Mg_2Ca [3].

Al has the most favorable effect on magnesium alloy. It improves strength and hardness, widens the freezing range, and makes the alloy easier to cast. An aluminum content of 6.0 wt% yields the optimum combination of strength and ductility. It has been widely reported that the level of Al plays a significant role in determining the properties of magnesium alloys. In most cases, including or not including other alloying elements, mechanical property data of cast or wrought alloys have been improved [31]. Al content also play important role in the corrosion behavior of the Mg alloys regarding to the intermetallics content and distribution. Several attempts has been done to understand the effect of various Al containing intermetallics on the corrosion behavior. Ben-haroush [4] used scanning kelvin probe force microscopy (SKPFM) technique which depicts the volta-potential distribution of the surface and mentioned that both $Mg_{17}Al_{12}$ (β-phase) and Al_8Mn_5 plays cathodic role for the matrix of AZ80 alloy. Lee et. al [32] studied the corrosion behavior of an as-cast Mg-xAl and Mg-xAl-1Zn alloys focusing on the galvanic corrosion between a precipitate and Mg-rich matrix. They found that that the β-phase that is a typical precipitate in an Mg-xAl alloy is a more potent cathodic phase than in the ternary precipitate in a Mg-xAl- 1Zn alloy. They proposed that the

variation of the Anode-Cathode Area Ratio (ACAR) and the chunk breakage of precipitate during corrosion play the dominant role in the corrosion rate.

Zn is a crucial element for the human body and it is necessary for many biological functions [33]. From materials viewpoint, Zn is known to increase age hardening response as it produces intermetallic compounds and refine the grain size [34]. A small amount of Zn contributes to the strength due to solid solution and precipitation strengthening but the maximum solubility of Zn in pure magnesium is 6.2 wt. % up to this level zinc can be used as solution hardening [35, 36]. Since Zn is more anodic than Fe and Ni that might be present as impurities in Mg alloys, it helps to overcome their harmful corrosion effect [5]. Zinc is reported to improve the mechanical property through the solution hardening mechanism, enhance the corrosion potential of pure magnesium by forming surface protecting layer and making nobler the alloy [35]. Ben-Hamu et. al [37] used SKPFM analysis to understand the effect of intermetallics corrosions of different formed after phases addition of Si and Ca in the Mg–6% Zn–1% Mn and Mg–6% Zn–1% Mn–5% Si alloys, respectively. Four phases were identified in extruded ZSMX magnesium alloy: $MgZn_2$, Mn_5Si_3, CaMgSi and Mg_2Si. All these phases present cathodic behavior relative to the magnesium matrix. They found Mg_2Si intermetallics may have a less strong cathodic behavior than other intermetallics, while CaMgSi intermetallics exhibit strongest cathodic behavior. The size and amount of this intermetallic depend on the calcium content. Finally from these results, it is concluded that the cathodic phases might be effective sites for the initiation of localized corrosion in extruded ZSMX magnesium alloy and so the amount of interemtallics and volta-potential difference of them relative to the matrix play important role in the corrosion rate.

1.2 Severe plastic deformation (SPD)

Severe plastic deformation (SPD) randomizes the texture and uniforms microstructure through ultra-fine grains (UFG) formation by applying force on

different directions. Several SPD techniques such as equal channel angular pressing/Extrusion (ECAP/ECAE) [38-47], accumulative roll bonding (ARB) [48-51], accumulative back extrusion (ABE) [52-56], three roll planetary milling or screw rolling (SR) [9, 57, 58], friction stir welding (FSW) [59-62], high pressure torsion [63-66] and multi directional forging (MDF) [67-77] have been reported. Majority of these researchers worked on changing the process parameters such as strain rate, number of passes and processing temperature to improve the mechanical properties of alloys, but corrosion behavior after these processes, in particular MDF and SR, has been rarely studied.

Mostaed et al. [38] used ECAP process for deforming as-cast ZK60 alloy and reported that even though ECAP can produce UFG and enhance the mechanical properties, this treatment had minor effect on corrosion behavior. However, its main contribution is to make a finer and more homogeneous second-phase dispersion and thereby, depressing the localized corrosion pitting. Moreover, Li et. al [40] by applying ECAP to samples of pure Mg at different temperatures, found that the samples produced at lower temperatures show smaller grains, higher yield strength and higher corrosion rate. The increase in strength at lower temperatures is related to smaller grains size but they also mentioned that higher temperature can release more strain energy and weaken the deformation texture of the sample compared with the samples processed at lower temperature.

Song. et.al [41] also used ECAP for deforming as-cast AZ91D alloy studying the corrosion resistance of the samples produced with different numbers of passes. They found that the ECAPed samples have higher corrosion rate comparing to as-cast samples but increasing the ECAP passes decreased the corrosion rate. They explained that the lower corrosion resistance of ECAPed AZ91D alloy is closely related to the severely deformed α-phase matrix and the refined β-phase. The strains-induced mass crystalline defects, including energetic high-angle grain boundaries and dislocations, offer the α-phase matrix more corrosion activation and weaker corrosion resistance. The change from net-like β-phase into isolated and uniformly distributed fine particles limit its barrier function to the corrosion

propagation in the α -phase matrix. The interaction of two factors also changed the corrosion behavior from pitting into serious uniform corrosion of AZ91D alloy. Macroscopic preferential corrosion and filiform corrosion have been observed in the ECAPed AZ91D Mg alloys. The former phenomenon results from inhomogeneous strains distribution in ECAPed samples, and the latter correlates with the stored energy on the deformed grain boundaries.

Multi directional forging is reported effectively control the properties of alloys by controlling the microstructure paramters. Highest yield strength among Mg alloys was achieved by MDF of AZ61 combined with aging treatment [74]. Fatigue properties, in addition to tensile strength has also been improved after 3 passes of MDF of AZ61 [75]. MDF has effectively weakened the texture of the extruded alloy while after 8 passes of MDF a fullty random texture was achieved.

Despite several reports for improving the mechanical properties of Mg alloys by MDF, effect of MDF on corrosion behavior have not been reported yet. So, in this work MDF process at different temperatures has been utilized to manufacture an alloy with a high corrosion resistance and mechanical property and it was found that MDF not only can control the mechanical properties but also can significantly control the corrosion behavior.

1.3 Parameters Influencing on Corrosion Behavior

There are several parameters which determine the corrosion rate of Mg alloys; they can be classified to the effects of composition, matrix (grain size) and second phases (intermetallic area fraction and volta-potential difference).

1.3.1 Composition

1. Some alloying elements can mitigate the detrimental effect of impurities on Mg corrosion. For example, Zr can remove Fe and purify Mg alloys by precipitation of Fe_2Zr or $FeZr_2$ from the alloy melt [10, 78]. Mn, Al and Si can also decrease the Fe content and decrease the corrosion rates of Mg

alloys, but not as effectively as Zr [23, 79]. So by analyzing the second phases, this effect can be studied

2. Some alloying elements can significantly alter the surface film of a Mg alloy, and thus affect the corrosion behavior. For example, two Al^{3+} ions can replace three Mg^{2+} ions in tetrahedral $Mg(OH)_2$ lattice in the surface film on Mg-Al alloys [80]. So by analyzing the passivation behavior this effect can be studied.
3. Some alloying elements can modify the exchange current density of the cathodic or anodic reaction on Mg alloys, which could either increase (e.g. Cu) or decrease (e.g. Al, Lu and As) the corrosion rate [81-83]. These effect also can be considered by analyzing the corrosion potential of the matrix or second phase.
4. When the alloying element exceeds its solubility in Mg, a second phase containing this element may precipitate from the Mg matrix. The second phase typically accelerates the corrosion rate due to the micro-galvanic effect between the second phase and the Mg matrix [10] .
5. Some alloying elements can alter the characteristics of an existing phase, forming a different second phase, which is less detrimental to the Mg corrosion behavior. [10]

So it can be seen that the effect of composition can be considered through few parameters that affect microstructure, second phase distribution and their potential difference, or altering the possible forming passive layer.

1.3.2 Passivation

Passivation is creation of an outer layer of shield material that is applied as a micro coating, created by chemical reaction with the base material, or allowed to build from spontaneous oxidation in the air. As a technique, passivation is the use of a light coat of a protective material, such as metal oxide, to create a shell against

corrosion. Passivity in a Mg alloy might be produced through a non-equilibrium technique with a sufficiently-high concentration of a strong passivating element supersaturated in the matrix phase [10]. The oxide, MgO, on the surface has a Pilling-Bedworth ratio <1 resulting in an incomplete coverage of the surface oxide or a porous film [81]. High-purity Mg does not exhibit passivity [84]. In fact, high-purity Mg is active in all experimental conditions except in chromic acid solution [7, 85].Some alloying elements may form oxide films with Pilling-Bedworth ratio>1, but the oxides often have too high solubility in aqueous solutions to form a stable and protective surface film on Mg, or the alloying elements cannot be easily dissolved in Mg to form a solid solution with Mg. Therefore, no successful corrosion resistant Mg alloy has been reported so far. Nevertheless, a more corrosion resistant Mg alloy remains a research goal.

Another aspect that can be discussed with regard to general corrosion resistance is the cohesive energy E_{coh}, which can be considered as a measure of the overall chemical stability of the material. A higher E_{coh} would therefore imply that more energy is required to break the primary chemical bonds of the compound during chemical reaction. Since, Y, Al and Ca hydroxides are characterized by a higher cohesive energy than $Mg(OH)_2$, It has been assumed that these three elements can positively affect the corrosion resistance of the alloys when exposed to the chemically reactive environment in contrast to what is observed in the present study for the case of pure hydrolysis of the alloyed forms with pure water. The value of the cohesive energy E_{coh} thus could serve as a qualitative criterion for comparing and selecting materials that would likely exhibit better resistance to decomposition than pure magnesium hydroxide [86].

The passivity behavior is related to the several parameters where the most important ones are their formation gibbs free energy (or enthalpy in fixed temperature), cohesive energy which shows their stability [86], pilling-bedworth ratio which shows their compactness and also their coherency with the matrix.

1.3.3 Grain size

Grain size is one the most important factors that determine mechanical properties and also corrosion behavior of the materials. In the case of mechanical properties, yield strength and hardness is related to the grain size through the hall-petch equation. However, the effect of grain size on the corrosion properties is more complicated and there are several controversial reports where some reported increasing grain size increases the corrosion rate and some reports vice versa. However, majority of the researches in the case of pure metals [87] including pure Mg reported that corrosion rate decreases by decreasing the grain size. Increasing the grain size reduces the grain boundary length. Grain boundaries have been formed from series of dislocations. To measure dislocations density, XRD peak profiles can be evaluated to analyze the dislocations density which is mainly related to peak width, described as full width at half maximum (FWHM) [75, 88, 89].

Fig. 1. shows the effect of grain size on the corrosion rate of different alloys. As one can see, there is no single trend for this relationship. It seems that regarding to the type of alloy, distribution of the second phase, processing route of changing the grain size, researchers have obtained different trends. So for understanding the real effect of grain size on the corrosion rate, we will classify these studies into two major groups including pure Mg and alloys.

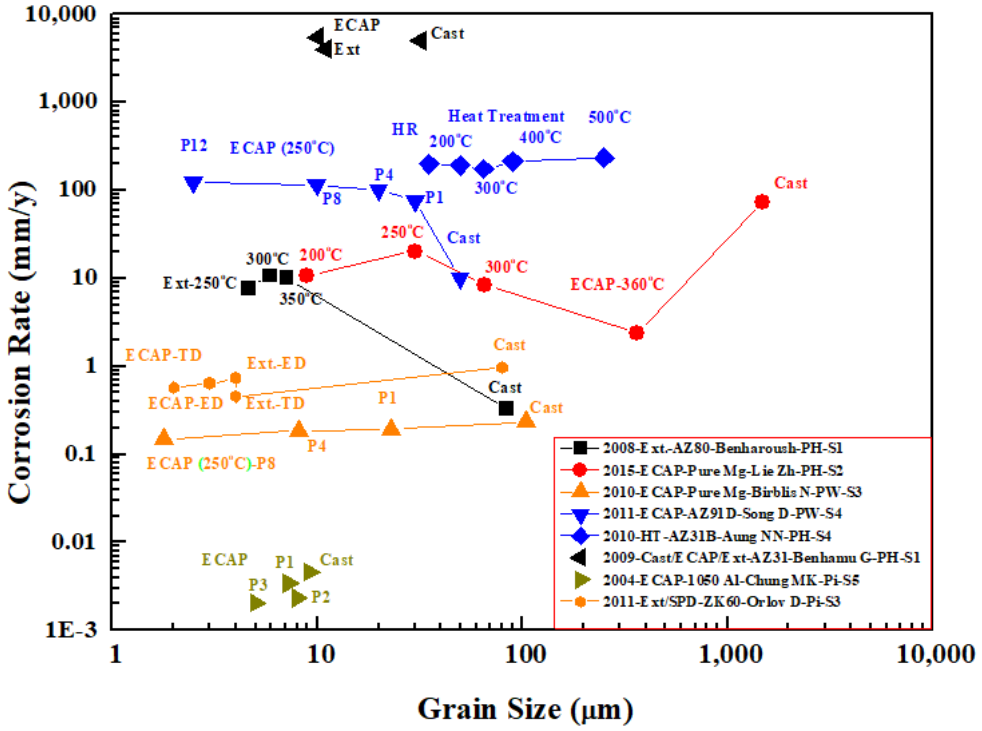

Fig. 1. Literature review about the effect of grain size on the corrosion rate [4, 39-42, 90-92]. S1: 3.5 wt.% NaCl + $Mg(OH)_2$, S2: SBF, S**3**: 0.1 M NaCl, S4: 3.5 wt.% NaCl, S**5**: 0.1M Na_2SO_4, S**6**: 3 wt.% NaCl

Effect of grain size on the corrosion rate of pure Mg

Fig. 2. depicts the corrosion rate versus grain sizes of pure Mg obtained from different studies. It seems that even in pure Mg, there is no single trend. While in some cases corrosion rate increases with grain size increase and in some cases vice versa. As a matter of fact, grain boundaries are the high energy sites and so the corrosion initiates from these sites. With assumption of no defect in the material, grain boundaries should increase the corrosion rate. That is why a single crystal material with the packed orientation like basal plane exposed to the corrosion has a very lower corrosion rate (~0.5 mm/y in SBF for 1d immersion of basal pure Mg) [82]. But adding grain boundaries and decreasing the grain size, increases the corrosion rate by localization of the corrosion and breaking down the surface layer. However, in majority of the cases, corrosion rate has been decreased by decreasing the grain size. Researchers reported that this corrosion improvement by decreasing the grain size is related to the more coherent and stable passive layer which can be formed on the exposed surface of the metals with more grain boundaries. In fact, grain boundaries, by providing more dislocations, compensate the mismatch of the hydroxide/oxide layer with the base metal [87, 90, 93, 94]. This behavior has also been proved through the corrosion study of other pure materials like Al, Fe and Ni [95-99].

So it can be concluded that in the case of large grain size like single crystals or bi-crystals the corrosion rate increases with increasing the grain size, while in very fine grains (may be less than 50 μm in Fig. 2) the corrosion rate decreases by decreasing the grain size. However, the possibility of the passivation regarding to the solution property should be considered. The less aggressive solutions like 0.1 M NaCl will probably increase the range of passivation, so the grain size tolerance to provide passivating layer increases. A literature review about the effect of grain size on

corrosion rate, especially for pure metals has been prepared and mentioned in the supplementary data, Table S4.

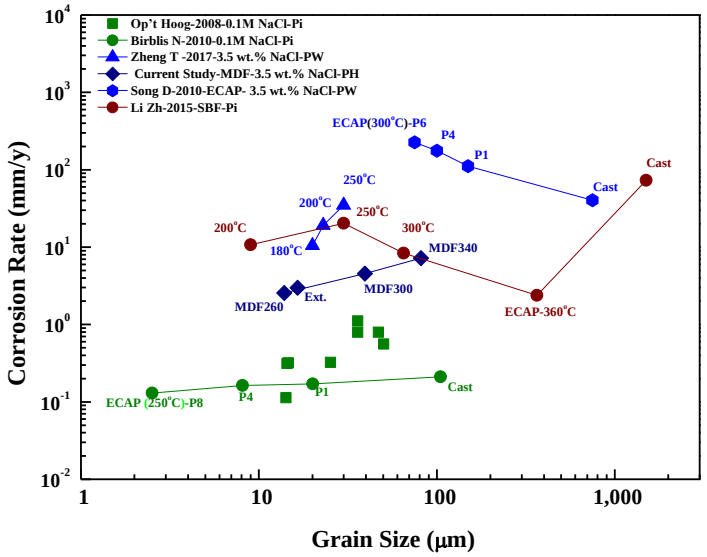

(a)

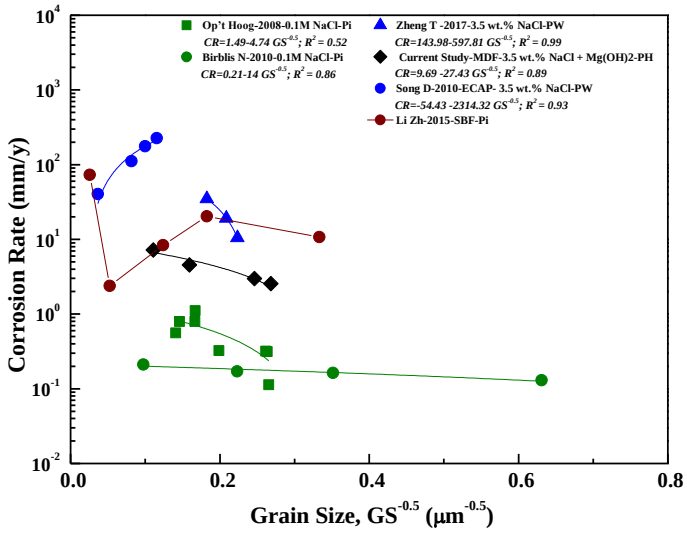

(b)

Fig. 2. Effect of Grain size on i_{corr} (corrosion rate) of the pure Mg [40, 90, 100-103]. (a) corrosion rate vs. grain size, D (μm) and (b) corrosion rate versus grain size $D^{-0.5}$ ($\mu m^{-0.5}$) where the fitted lines has been also mentioned.

Effect of grain size on the corrosion rate of alloys

Galvanic cells that form through the formation of the intermetallic compounds are one of the main factors determining the corrosion behavior. The distribution of the secondary phases, as well as their potential difference with the matrix determines the electron current density in these galvanic cells. It should be considered that within grain size change by changing the processing conditions (such as temperature or strain rate changes), the fraction and distribution of second phases change. So that is why for investigation about the grain size, researchers should be very careful about the influence of other parameters change on the corrosion rate.

Fig. 3 shows the effect of Al addition in the corrosion behavior of Mg-Ca alloy. Since Mg_2Ca is anode and matrix is cathode in the Mg-Ca system, addition of Al forms $(Mg, Al)_2Ca$ and Al_2Ca which are cathode relative to the matrix. So if the second phase is a continuous anodic phase, it will be degraded during corrosion and the electrolyte will introduce into the material and accelerates the corrosion, but in the case of continuous cathodic second phase, it functions as a barrier for the electrolyte and will not allow the corrosion to progress into the material and finally more uniform corrosion occurs [104]. So within severe plastic deformation, not only grain size decreases, but also the continuous net-shape second phase breaks into isolated particles and the corrosion mechanism will totally be changes. So one, cannot simply says that corrosion rate increases with decreasing the grain size.

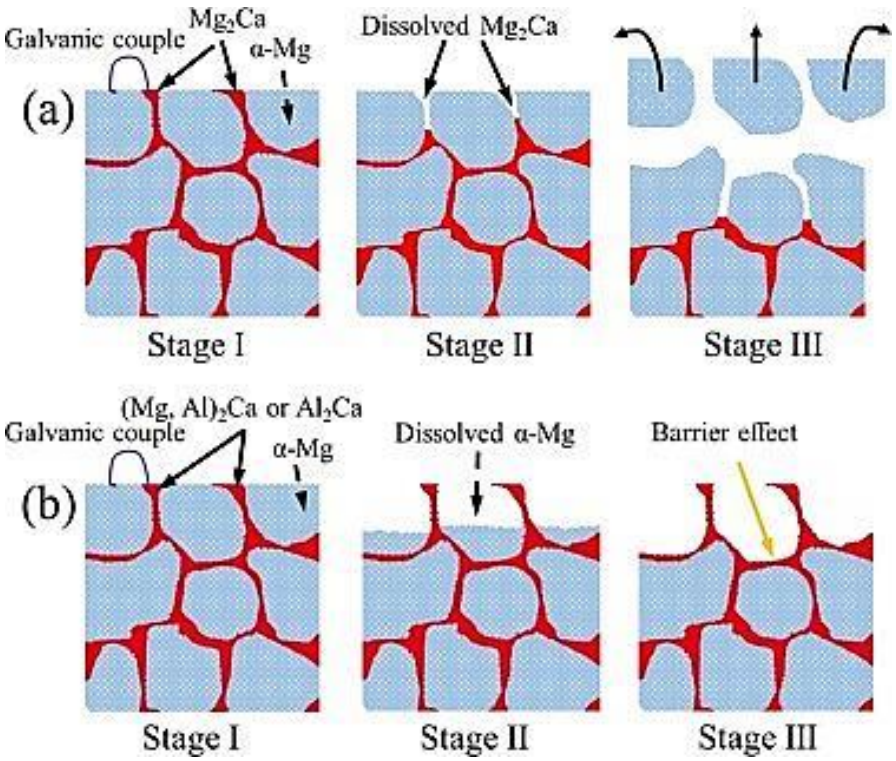

Fig. 3. Schematic illustration of the role of continuous second phases in the Mg-Al-Ca alloys where their distribution is continuous: (a) when the secondary phase is Mg_2Ca, (b) when the secondary phase is $(Mg, Al)_2Ca$ or Al_2Ca [104].

Ben-haroush et. al [4] extruded the as-cast AZ80 alloy at 250, 300 and 350 ^{o}C. They reported that corrosion rate of the extruded alloy was more than cast alloy regarding to breaking down the interconnected β-phase to isolated shape, They mentioned that increasing the temperature from 250 to 300 ^{o}C (in a trend that grain size increases) increased the corrosion rate regarding to the increasing dislocation density. This concept seems not be correct, because dislocation density like grain boundary length decreases by increasing the temperatures. They measured the dislocation density using TEM analysis which is a very local analysis and it cannot be extrapolated to the whole sample. The corrosion rate was slightly decreased from 300 to 350 ^{o}C, but no specific reason was mentioned here.

Song et. al [41] analyzed the corrosion rate of AZ91D after different pass numbers of ECAP in 3.5 wt.% NaCl solution. The ECAP process was carried out at 250 ^{o}C. They found a trend which is totally different from that of obtained by ECAP of pure Mg at 250 ^{o}C [90] while here increasing the passes number and hence decreasing the grain size resulted in increasing the corrosion rate. They emphasized that ECAP results in severe deformed ultra-fine grains (UFG), α-phase matrix and the refined β-phase. The strains-induced mass crystalline defects, including energetic high-angle grain boundaries and dislocations, offer the α-phase matrix more corrosion activation and weak the corrosion resistance of α-phase matrix (This theory is also against the theory which was mentioned by Birbilis [90] and it is against the pure Mg studies). The change from net-like β-phase into isolated and uniformly distributed fine particles bereaves its barrier function to the corrosion propagation in the α-phase matrix. According to [41], the interaction of two factors also caused the corrosion behavior changing from pitting corrosion into serious uniform corrosion of AZ91D alloy.

Aung et al. [91] using heat treatment on a hot rolled AZ31B alloy at temperatures from 200 to 500 ^{o}C with 100 ^{o}C intervals and immersion study in 3.5 wt.% NaCl, found out that corrosion rate decreases from 200 to 300 ^{o}C but increases from 300 to

500 ^{o}C. They mentioned that twins are dominant in as-received and HT-200 ^{o}C sample while they have been disappeared in HT-300 ^{o}C. Grain boundaries act as corrosion barrier so increasing grain size decreases this barrier. This trend (optimum corrosion rate at 300 ^{o}C) is similar to that of obtained in the current study. However, these researched didn't discuss about the effect of second phases.

Chung et al [42] ECAPed the 1050 Al alloy and measured the corrosion rate after different pass numbers. They found that more pass numbers decrease the corrosion rate as well as decreasing the grain size. They reported that the size of the Si-containing impurities decreases with increasing ECAP pass numbers, N. In addition, with increasing N, the impurities are spread more uniformly. The ECAPed AA 1050 forms a relatively stable oxide layer. The results of the EIS test after forming pitting at the oxide layer shows that the polarization resistance increased with increasing the number of ECAP pass times. The SEM and EDS observations of the sample surface after potentiostatic test show that the Si-containing impurities exist at the sample surface of the ECAPed AA 1050. The size of the Si-containing impurities decreased with increasing ECAP pass number, N. In addition, with increasing N, the impurities are spread uniformly. The pit forming mechanism of the ECAPed AA 1050 is related to formation of the local micro-galvanic cell between Al matrix (anode) and Si-containing impurities or mixed oxide containing Si (cathode). Hence, using the ECAP technique, the size of the Si-containing impurities was decreased and the area of cathode is reduced. Thus, the pitting resistance can be increased with increasing the number of ECAP pass times.

By the way, the role of grain size in the alloys is more complicated than pure metals, because the second phases as well as added elements in the matrix play important role in corrosion behavior by formation of galvanic cells and changing the hydroxide/oxide layer property. Changing the grain size by any process condition like temperature, number of process passes, direction of applying deformation, cooling rate and so on will change the second phase and matrix concentration and so these effects also need to be considered in corrosion behavior. Therefore, grain

boundary effect on the corrosion rate is more reliable when it is studied in the pure metals.

Finally, it can be concluded that in the case of large grain size like single crystals or bi-crystals the corrosion rate increases with increasing the grain size, while in very fine grains (may be less than 50 μm in Fig. 2) the corrosion rate decreases by decreasing the grain size. However, the possibility of the passivation regarding to the solution property should be considered. The less aggressive solutions like 0.1 M NaCl will probably increase the range of passivation, so the grain size tolerance to provide passivating layer increases.

1.3.4 Texture

Several studies have been done to understand the effect of texture on the corrosion rate. Different crystallographic planes have different atomic density and so have different corrosion rates. Single crystal studies shows the basal planes and after that prismatic II and then prismatic I planes have the higher corrosion resistance comparing to the other intermediate planes [82]. Moreover it has been reported that any misorientation from the packed planes including basal and prismatic planes increases the corrosion rate [105]. Basal planes have the highest corrosion resistance, due to close packed atomic structure and prismatic II and then prismatic I have lower corrosion resistance, respectively [82, 105-112].

1.3.5 Second phase (phase fraction and volta-potential)

One of the most important factors in corrosion behavior of the alloys is the galvanic cell corrosion. Galvanic corrosion can be formed between the intermetallic phases and matrix. The potential difference between the intermetallic phase and matrix is the driving force of the electrons to move from anode to cathode and form the galvanic cells. In addition, the fraction of the intermetallic phase can determines the effective surface involves in the electron current density.

The potential difference between intermellic phases and matrix can be obtained through the direct measurement of the potential of each phase using open circuit potential (OCP) [113] or using scanning kelvin probe force microscopy (SKPFM) [114] or first principle calculation through measuring the surface potential and work function [115].

Fig. 4 shows the volta-potential difference of various intermetallics with the matrix which is obtained from the literature. The related values with the references have been mentioned in the Table 1. Since Mg is one of the most active elements in the series of standard electrode potential and also its work function is less than majority of alloying elements, most of the intermetallics phases act as cathode for the Mg-

rich matrix. But if the matrix potential increases or allowing elements with low work function values like Ca (WF=2.8), Ce (WF=3.1), Nd (WF=3.2) or Y (WF = 3.1) comparing to Mg (WF=3.66) is used, the anodic intermetallic phases can be formed. As it can be seen in the following image Mg-Ce, Mg-Nd-Y and Mg_2Ca phases showed the anodic behavior relative to the matrix. But the rest of intermetallics showed the cathodic behavior.

1.4 Research Objectives

As it was mentioned, Mg alloys are very attractive structural materials for biomedical applications, light-weight vehicles and electronic devices due to their high strength-to-weight ratio. High purity Mg has theoretically the lowest corrosion rate but it's very low strength limits its usage in different applications. So it is necessary to produce a light-metal alloy with high strength and corrosion resistance. Therefore in this study it was tried to produce a light weight material using various parameters including alloying, casting, extrusion and severe plastic deformation process. In this regard various elements, including Mn, Ca, Al, Sn and Zn added to the commercial pure Mg with different percentages and their effect on both mechanical and corrosion properties was analyzed. Then, the alloys with high corrosion resistance and mechanical properties was subjected to severe plastic deformation processes including multi directional forging (MDF) and screw rolling (SR). The process conditions like strain rate and temperature was changed to find out their effect on mechanical and corrosion properties. Moreover, one of the ambiguous problems in the corrosion area is that there are several parameters that control the corrosion behavior and researchers will use some of them to explain the dominant factor on the corrosion behavior of their materials. There is also same problem for the yield strength area but there exist some equations like hall-petch that explains the yield strength of the materials. So such equation is required for the corrosion area. So to understand the mechanism of the corrosion resistance a quantitative analysis was done with all affecting parameters, an experimental model

was proposed and it was validated with the current obtained data as well as literature data.

Finally the objectives of this research can be classified as follows.

a. Developing a high strength and corrosion resistance material
b. Optimizing the process conditions
c. Analyzing the effects of alloying elements and processing conditions on strength and corrosion rate of materials
d. Quantitative analyzing the parameters affecting on corrosion rate
e. Developing a new experimental model to predict the corrosion rate of the materials

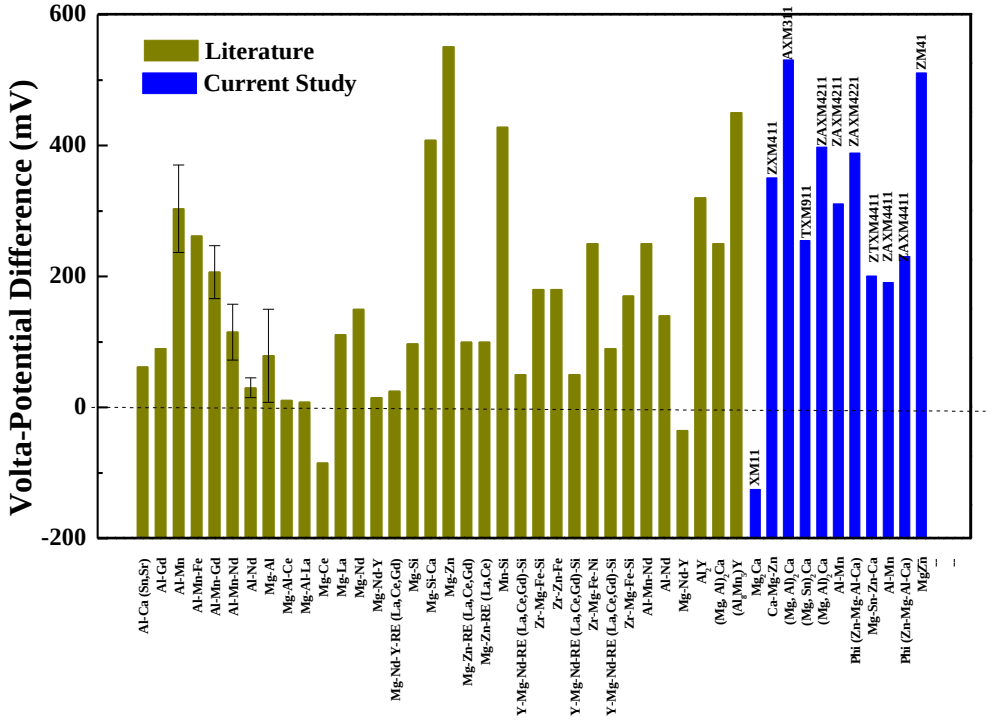

Fig. 4. Volta-potential difference of intermetallics with the matrix for the magnesium alloys.

Table 1. Volta-potential difference of different intermetallics with the matrix for the magnesium alloys.

Phase	Pot. Diff.	Alloy	Ref.	Phase	Pot. Diff.	Alloy	Ref.
Al-Ca (Sn,Sr)	62	Mg-Al-Ca	[116]	Zr-Zn-Fe	180	ZE41	[117]
Al-Mn	303±66	-	[4, 118-121]	Y-Mg-Nd-RE(La,Ce,Gd)-Si	50	WE54-T6	[117]
Al-Gd	90	AM50Gd	[122]	Zr-Mg-Fe-Ni	250	WE54-T6	[117]
Al-Mn-Gd	206±40	--	[121, 122]	Al-Mn-Nd	250	AZ91-Nd	[123]
Al-Mn-Nd	115	AM50Nd	[124]	Al-Nd	140	AZ91-Nd	[123]
Al-Nd	30	--	[118, 125]	Mg-Nd-Y	-35	EW75	[126]
Mg-Al	78±71	--	[4, 37, 117, 118, 121, 127]	Al_2Y	320	EW75	[126]
Mg-Al-Ce	11	AMCe	[127]	$(Mg, Al)_2Ca$	250	AZCW6110	[128]
Mg-Al-La	8	AMLa	[127]	$(Al_8Mn_5)Y$	450	AZCW6110	[128]
Mg-Ce	-85	Mg-2Ce	[124]	Mg_2Ca	-130	XM11	This Study
Mg-La	111	Mg-1La	[124]	Ca-Mg-Zn	350	ZXM411	This Study
Mg-Nd	150	Mg-2.6Nd	[129]	Al-Mn	190	ZAXM4411	This Study
Mg-Nd-Y	15	WE43-T6	[117]	Φ (Zn-Mg-Al-Ca)	230	ZAXM4411	This Study
Mg-Si	97	AZ80	[130]	$(Mg, Al)_2Ca$	397	ZAXM4211	This Study
Mg-Si-Ca	408	ZSM651+0.8Ca	[124]	Al-Mn	310	ZAXM4211	This Study
Mg-Zn	551	ZSM651+0.8Ca	[124]	Φ (Zn-Mg-Al-Ca)	388	ZAXM4221	This Study
Mg-Zn-RE (La,Ce,Gd)	100	ZE41	[117, 124]	$(Mg, Sn)_2Ca$	254	TXM911	This Study
Mg-Zn-RE (La,Ce)	100	ZE41	[117]	Mg-Sn-Zn-Ca	200	TZXM4411	This Study
Mg-Si	428	ZSM651+0.8Ca	[37]	Φ (Zn-Mg-Al-Ca)	388	ZAXM4221	This Study
Y-Mg-Nd-RE(La,Ce,Gd)-Si	50	WE43-T6	[117]	$(Mg, Al)_2Ca$	533	AXM211	This Study
Zr-Mg-Fe-Si	180	WE43-T6	[117]	MgZn	510	ZM41	This Study

Chapter 2: Experimental procedure

2.1 Extrusion

Different alloys as well as pure Mg were prepared in the in an electric furnace under a mixture of CO_2 and SF_6 gases in a steel mold with 80 mm diameter. Cylindrical billets were machined and then kept in a heating furnace at for 12 h, followed by quenching into air. Prior to the extrusion, the samples were pre-heated at 280 °C for 0.5 h in a resistance furnace. Then the billet was transferred quickly to the extrusion machine chamber and indirect extrusion was carried out at 260 °C. The Mg-xMn series was carried out with the extrusion ratio of 10:1 and 5 mm/s ram speed while the final cross section was 22 ×22 mm for the alloys were supposed to be MDFed, 25 mm diameter for the alloys were supposed to be SRed. For the case of Mg-xMn series the extrusion mold with the diameter of 15 mm was used.

2.2 MDF

Rectangular cubes with the size of 22×22×28 mm were cut off from the extruded sample and subjected into MDF using an Instron 5582 machine at an initial strain rate of 3×10^{-3} s^{-1} to a cumulative strain of $\sum \bar{\varepsilon} = 2.7$ through 9 passes. During MDF, the sample was placed at the furnace to provide the desired temperature. A schematic representation of the current MDF is shown in Fig. 5. After each pass, the forged sample was rotated 90^{o} and the surface was abraded with abrasive papers up to 1200 for recovering the deformed surface.

Moreover, Electron Back-Scattered Diffraction (EBSD) and X'Pert Pro XRD were used to analyze the texture of different samples.

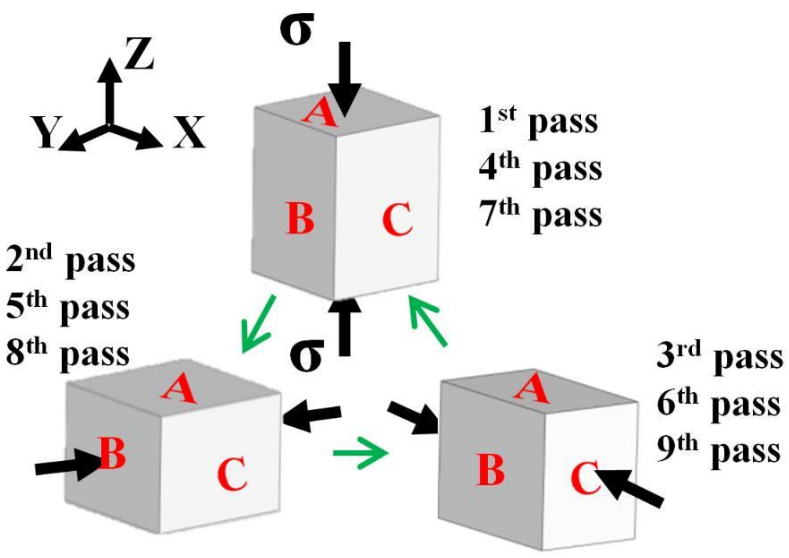

Fig. 5. Schematic representation of the MDF process.

2.3 Screw rolling (SR)

Cylindrical bars with 70 mm length were cut off from the extruded bar and were subjected to the screw rolling process (Fig. 6). The diameter of extruded bar was reduced to 15 mm through 6 passes while the sample was preheated in the screw rolling temperature for 30 min before each pass. The samples were designated as Ext., related to extruded sample and SR220, SR260, SR300 and SR340 related to screw rolled samples processed at 180, 220, 260, 300 and 340 ^{o}C, respectively.

Samples for further analysis were cut perpendicular to the extrusion direction which is the same as the screw rolling direction. Furthermore, samples were etched in a solution of acetic picral (10 ml of acetic acid, 4.2 g of picric acid, 10 ml of water and 70 ml of ethanol) to observe microstructure and grain size.

`

2.4 Microstructure

To observe microstructure and measure the grain size with optical microscopy, samples were etched in a solution of acetic picral (10 ml of acetic acid, 4.2 g of picric acid, 10 ml of water and 70 ml of ethanol).

The surface morphologies (bare or immersed) were observed by a Merlin compact field emission scanning electron microscopy (FE-SEM) with an accelerating voltage range of 15.0 kV and working distance of 10 mm and a JEOL-JSM-6360 SEM with same working distance and accelerating voltage. XRD analysis was carried in D8-Bruker machine with 2θ scan range from 10^{o} to 80^{o} for investigating the formed phases. The XRD was used aslo for measuring the dislocation density. In this regard, the Scherer equation tool in the X'Pert Highscore Plus, version 2.1 software was used to measure the crystallite size and lattice strain, then using the equation of $\rho_{\perp}=1/D^{2}$ [131], the dislocation density was obtained.

2.5 Mechanical properties

The tensile and compression tests were performed with a strain rate of 2×10^{-4} s^{-1}. A R&B universal machine was used to test the MDFed samples where the gauge length of the samples were 10 mm with the thickness of 1 mm. A 5582 instron universal machine was used for tension test according to the ASTM standard B557M. A Fischer indenter was used for measuring the Vickers hardness values.

2.6 Corrosion studies

Square samples with the dimensions of 20×20×2 mm (length×width×thickness) for the extruded and MDFed samples and round samples with the diameter of 15 mm and thickness of 3mm for the screw rolled samples were cut to measure the corrosion rate by hydrogen evolution, weight loss and electrochemical method in 3.5 wt. % NaCl solution saturated with $Mg(OH)_2$ at 24±1 °C. The immersion experiments were set up according the experiments of Arthanari et. al [132]. Besides, in order to reduce the surface roughness effect on the corrosion performance, the exposed surfaces of all samples were polished successively with 400-2000 grit SiC abrasive papers and then ultrasonicated in ethanol. Corrosion rate of different materials have been obtained and compared using electropotential, hydrogen evolution and weight loss methods. The corrosion rate using polarization method, P_i (mm/y), was evaluated using Eq. (1) [1, 7, 133, 134].

$$P_i = 22.85\, i_{corr} \quad (1)$$

Where i_{corr} (mA/ cm^2) is the corrosion current density obtained from Tafel analysis. The corrosion rate using hydrogen evolution method, P_H (mm/y) was measured using Eq. (2) [1, 7, 133, 134].

$$P_H = 2.088\, V_H / At \quad (2)$$

Where V_H (mL) is the volume of evolved hydrogen, A is the sample surface area (cm^2) and t (d) is the immersion duration. Finally, the corrosion rate using weight loss method, P_w (mm/y), was calculated using Eq.(3) [1, 7, 133, 134].

$$P_w = 2.1 \frac{W_a - W_b}{At} \quad (3)$$

Where W_a (g) and W_b (g) are the sample weights after and before immersion, respectively. Moreover, A (cm^2) and t(d) are the sample surface area and immersion duration, respectively.

The potential distribution on the surface was measured by cypher AFM using the scanning Kelvin probe force microscopy method (SKPFM) in air at room temperature. The scan height above the sample was 100 nm and the scan frequency was 1.0 Hz. For all measurements, commercially available silicon tips coated with Pt/Ir were used.

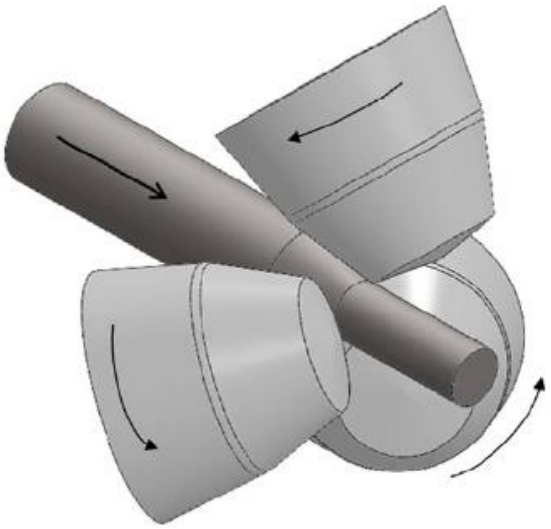

Fig. 6. Schematic representation of a screw rolling process [9].

Chapter 3: Results and discussions

3.1 Objective

The objective of the current project is to manufacture a low corrosion rate material with high strength. So in this regards several methods were utilized including alloy design by changing alloying elements, processing with different techniques like extrusion, multi directional forging and screw rolling and changing the processing conditions like temperature and strain rate.

The machines that used for the manufacturing has been shown in Fig. 7. So first extruded materials was tested and the effect of the elements like Mn, Ca, Al, Sn, and Zn was analyzed and later on the effect of each process and related processing conditions were explained.

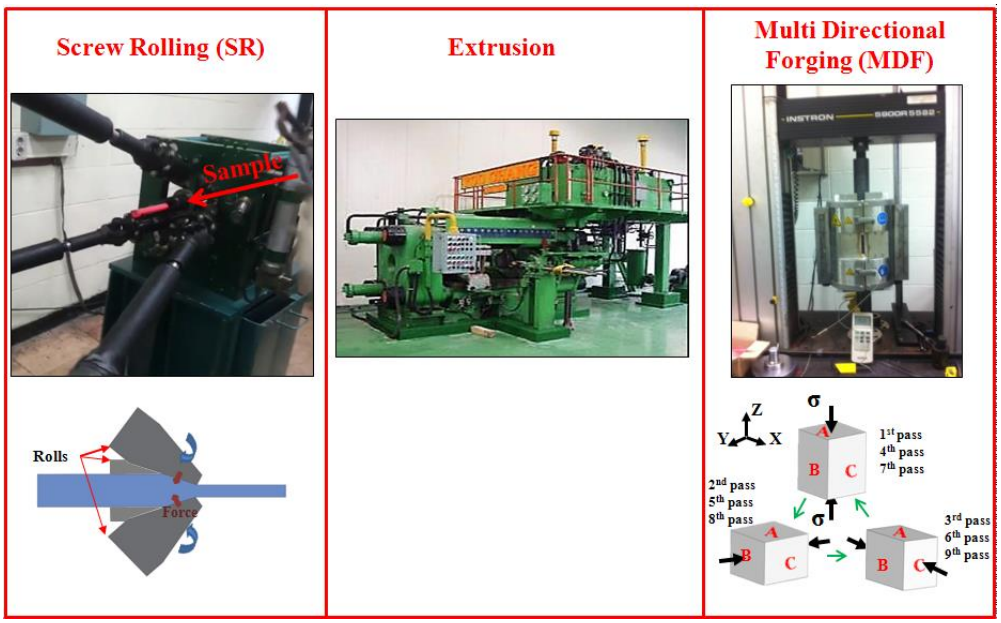

Fig. 7. Three different processing methods used in this work to produce high strength low corrosion rate materials including screw rolling (SR), extrusion and multi directional forging.

3.2 Extrusion

Chemical composition of the all studied materials have been shown in the Table 3.First of all, five alloys including pure Mg, Mg-0.1 wt.% Mn, Mg-0.3 wt.% Mn, Mg-0.5 wt.% Mn, Mg-1.0 wt.% Mn was manufactured with 25:1 extrusion ratio with final diameter of 15 mm to compare the effect of Mn addition on the corrosion behavior and mechanical properties. It was found that 0.5 wt. % Mn have the best combination of hardness and corrosion behavior on Mg. So for all other alloys the percentage of Mn was fixed on approximately 0.5 wt. %. Then Ca, Al, Sn and Zn with different percentages were added to find out the best combination of mechanical properties and corrosion behavior.

Table 2. Chemical composition of the studied alloys.

1	Designation	Al	Zn	Mn	Fe	Ca	Sn	Mg	Extrusion Ratio
2	Pure Mg	-	-	0.0167	0.0026	-	-	Bal.	25:1
3	Mg-0.1Mn	-	-	0.1166	0.0032	-	-	Bal.	25:1
4	Mg-0.3Mn	-	-	0.3269	0.0025	-	-	Bal.	25:1
5	Mg-0.5Mn	-	-	0.5108	0.0031	-	-	Bal.	25:1
6	Mg-1Mn	-	-	0.986	0.0033	-	-	Bal.	25:1
7	Pure Mg	-	-	0.0112	0.0030	0.0056	-	Bal.	10:1
8	XM11	-	-	0.5297	0.0041	0.6450	-	Bal.	10:1
9	ZXM411	-	3.5237	0.5630	0.0053	0.7163	-	Bal.	10:1
10	TXM911	-	-	0.5495	0.0047	0.7450	9.1400	Bal.	10:1
11	ZTXM4411	-	3.4357	0.5620	0.0047	0.6847	3.7750	Bal.	10:1
12	AXM211	2.3830	-	0.4803	0.0053	0.6803	-	Bal.	10:1
13	ZAXM4211	1.7390	3.6853	0.4556	0.0040	0.6480	-	Bal.	10:1
14	ZM41	-	3.6190	0.4357	0.0034	-	-	Bal.	10:1
15	ZAXM4221	2.0405	3.9330	0.5409	0.0057	1.2255	-	Bal.	10:1
16	ZAXM4411	3.8160	3.8385	0.5115	0.0075	0.5841	-	Bal.	10:1
17	ZAM421	1.9328	3.6878	0.4960	0.0050	-	-	Bal.	10:1

3.2.1 Effect of Mn on mechanical properties and corrosion behavior of pure Mg

As explained in the experimental procedure, the Mg-xMn alloys were produced by extrusion with 25:1 extrusion ratio with the final diameter of 15 mm. The corrosion studies were performed in SBF solution at 34^{o}C. The hardness Vickers values with corrosion rate (obtained from hydrogen evolution technique) has been shown in the Fig. 9 (a). It can be seen that the alloy contains 0.5 wt.% Mn has the lowest corrosion rate. Regarding to solubility of iron in Mn, the corrosion rate of Mg can be improved by addition of Mn but the solubility of Mn in the Mg is limited, so after 0.5 wt.% Mn the corrosion rate was increases again.

Grain refinement which is caused by adding Mn, resulted in the hardness enhancement, where a hall-petch equation can be written for the relationship between hardness and grain size Fig. 9 (b).

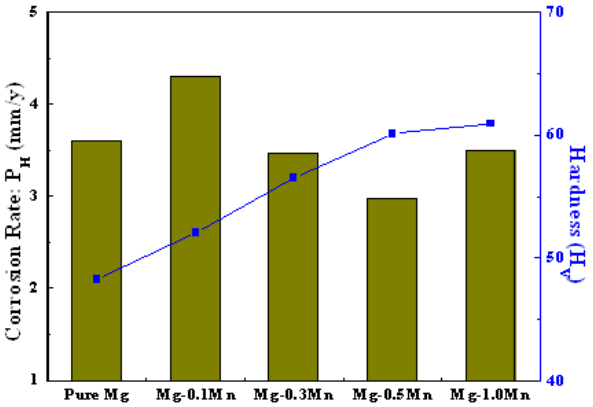

(a)

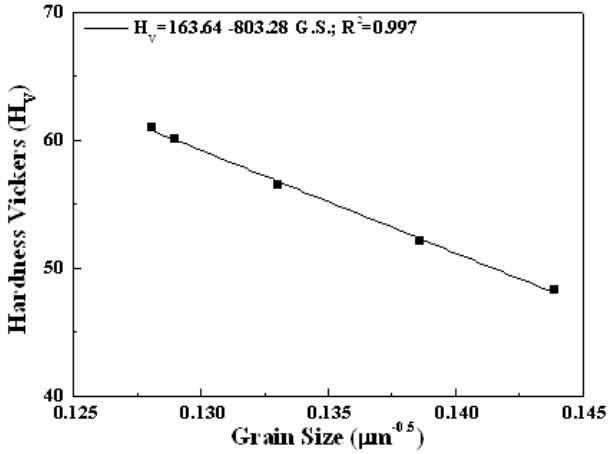

(b)

Fig. 8 Effect of Mn addition on (a) corrosion rate and (b) hardness of pure Mg.

3.2.2 Microstructure

The grain distribution of the studied alloys has been presented in the Fig. 9. The average grain size is reported in the

Table 3.The following results can be mentioned about the effect of alloying elements on the microstructure.

Addition of Al in ZXM411 alloy led to finer and more uniform grains distribution (See Alloys: ZXM411, ZAXM4211, and ZAXM4411)

Addition of Ca in ZAM421 alloy effectively refined the grains however abnormal grains still exist. (See Alloys ZAM421, ZAXM4211, and ZAXM4221).

In the next parts mechanical properties and corrosion behavior of the alloys will be discussed.

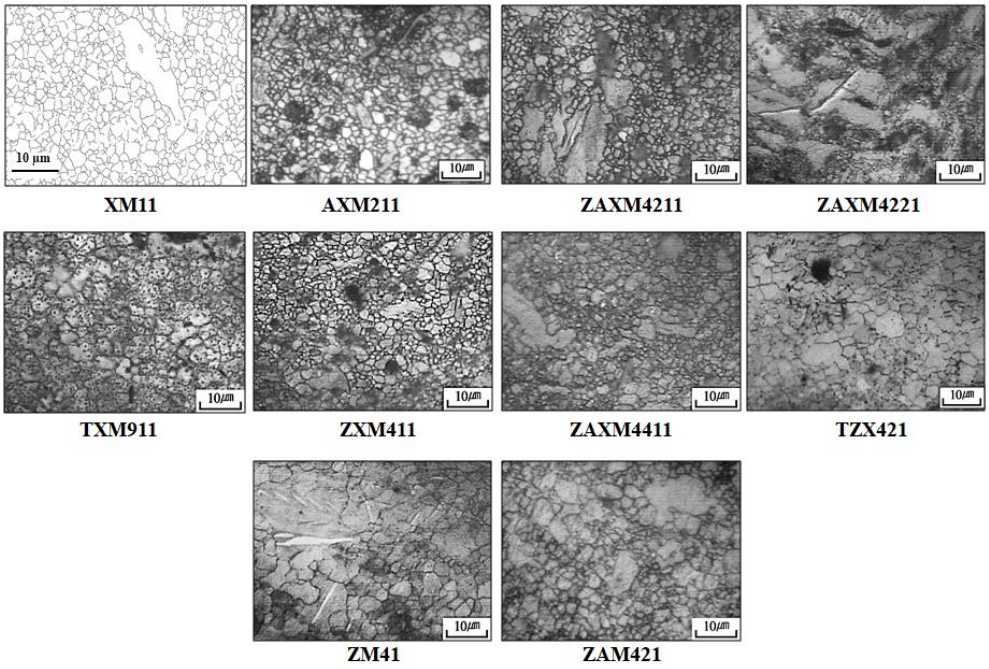

Fig. 9. The microstructure of the extruded alloys with the extrusion ratio of 10:1.

3.2.3 Mechanical Properties

To find out the best combination of the mechanical properties and corrosion behavior of the materials and comparing the effect of alloying elements, some alloys were designed as mentioned and designated in the Table 2 and then produced by extrusion. So from the mentioned alloys we can pick the best alloys with the best combination of mechanical properties and corrosion behavior to apply the later deformation process such as SR and MDF. The produced alloys can be studied in the following trends.

- Pure Mg
- Effect of Al, Zn, and Sn on XM11 (0.7 wt.% Ca – 0.5 % wt.% Mn)
- Effect of Ca (0.0, 0.7, 1.3 wt. % Ca) on ZA42 (3.8 wt. % Zn – 2.0 wt. % Al)
- Effect of Al (0.0, 1.8, 3.8 wt. % Al) in ZXM41
- Effect of Al (0.0, 1.8 wt. % Al) in ZM41
- Effect of Sn (0.0, 3.9 wt. % Sn) on the ZXM411

The mechanical properties of the studied alloys have been presented in the Fig. 10. The highest yield strength among the extruded alloys was obtained from ZAXM4221 alloy showing Ca is very effective on the yield strength of Mg alloys by reducing the grain size and formation of the secondary phases. The grain size of extruded alloys as well as their mechanical properties has been shown in the

Table 3.

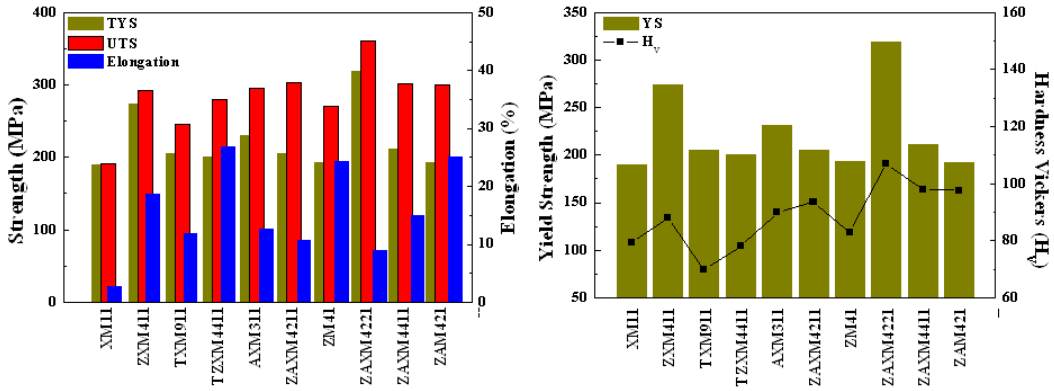

Fig. 10. Mechanical properties of the extruded alloys.

Table 3. Mechanical properties of the extruded alloys.

Designation	Grain Size (μm)	Hardness Vickers (H_V)	Y.S. (MPa)	U.T.S. (MPa)	El. (%)
XM11	2.70	79.26	189.51	190.91	2.71
ZXM411	2.47	88.01	274.06	293.08	18.73
TXM911	2.91	69.83	205.69	246.28	11.94
TZXM4411	2.65	78.04	200.62	280.24	26.75
AXM211	1.85	89.91	230.81	295.04	12.64
ZAXM4211	2.32	93.66	205.34	303.85	10.72
ZM41	2.94	82.88	193.21	270.59	24.37
ZAXM4221	1.76	107.07	318.44	360.155	8.93
ZAXM4411	2.04	97.93	211.52	302.16	14.99
ZAM421	2.47	97.65	192.00	300.66	25.10

3.2.4 Corrosion behavior

Corrosion rate of the seven day immersed extruded alloys in the 3.5 wt. % NaCl solution saturated with $Mg(OH)_2$ has been shown in the Fig. 11 and the related values have been presented in the Table 4. It can be seen that the XM11 has the lowest corrosion rate while TXM911 and ZAXM4221 have the highest value. The effect of allowing elements have been discussed in this study with a methodology based upon the volta-potential difference and microstructure parameters to explain and quantify the corrosion behavior of materials.

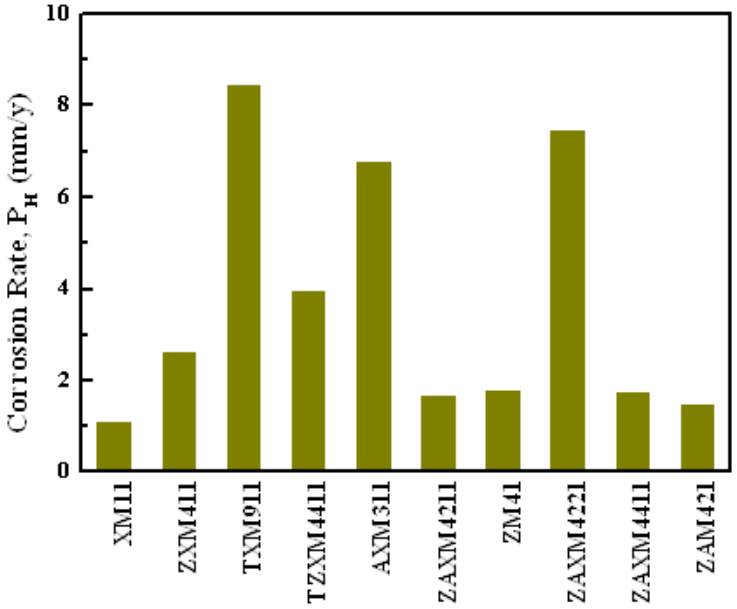

Fig. 11. Corrosion rate of the extruded alloys obtained by hydrogen evolution method after seven day immersion in 3.5 wt. % NaCl saturated with $Mg(OH)_2$.

Table 4. Corrosion values of the extruded alloys after seven day immersion in 3.5 wt. % NaCl saturated with $Mg(OH)_2$.

Alloy	**Evolved Hydrogen (ml/cm^2)**	**Corrosion Rate P_H (mm/y)**	**Weight Loss ($mg/cm^2/day$)**	**Corrosion Rate P_W (mm/y)**
Pure Mg	9.97	2.98	-	-
XM11	3.65	1.09	0.80	1.69
ZXM411	8.67	2.59	2.00	4.20
TXM911	28.26	8.43	4.18	8.77
ZTXM4411	13.14	3.92	2.85	5.99
AXM211	22.64	6.76	4.12	8.66
ZAXM4211	5.53	1.65	1.23	2.56
ZM41	5.93	1.77	1.90	3.99
ZAXM4221	24.99	7.46	4.01	8.21
ZAXM4411	5.81	1.73	1.48	3.10
ZAM421	4.94	1.47	1.30	2.74

The effects of alloying elements on mechanical properties and corrosion behavior of the extruded alloys can be summarized as below:

- Increasing Mn up to 0.5 wt.% decreased the corrosion rate and increased the hardness value.
- Ca addition in ZM41 and ZAM421 alloy decreases the grain size and increases the fraction of second phase and hence increases the yield strength, hardness and UTS. However, Ca addition decreases the tensile elongation. Addition of Ca in the ZAM421 from 0.0 to 0.6 wt.% didn't change the corrosion rate significantly while the addition of this element from 0.6 to 1.2 wt.%, increased the corrosion rate suddenly which is attributed to the increasing the second phase and hence galvanic corrosion.
- Zn addition in XM11 alloy, decreased the grain size and hence yield strength, UTS and elongation was increased. Actually, no plasticity was observed in the XM11 extruded alloy and so addition of Zn, like Al and Sn (as it will be discussed after this) enhanced the plasticity. However the corrosion rate of the XM11 alloy after addition of Zn was increased due to the formation of the second phases.
- Al addition in the ZXM411 alloy slightly decreased the grain size but decreased the yield strength from 0.0 to 2.0 wt.% Al due to texture randomization and increased the yield strength and elongation from 2.0 to 4.0 wt.% Al, however UTS was not changed significantly.
- Sn addition in ZXM411 alloy increased the grain size slightly and hence decreased the yield strength and UTS but increased the elongation and increased the corrosion rate.

3.3 Corrosion behavior and mechanical properties of Mg-Mn-Ca Alloy: influences of Al, Sn and Zn

3.3.1 Objective

To understand the effect of Al, Sn and Zn on the XM11 alloy, mechanical properties and corrosion behavior of this alloy was compared with three other alloys 2.4 wt.%, (2.0 at.%) Al, 9.1 wt. % (2.0 at.%) Sn and 3.6 wt.% (1.5 at.%) Zn and designated as AXM211, TXM911 and ZXM411, respectively.

3.3.2 Microstructure analysis

The formed phases during solidification were calculated using PanDat commercial software considering the Scheil equation (Fig. 12). The XM11 alloy contains α_{Mg} and Mg_2Ca after solidification. The predicted phases after solidification of AXM211 includes α_{Mg}, $Mg_{17}Al_{12}$, $(Al, Mg)_2Ca$, Al_4Mn, Al_8Mn_5 and $Al_{11}Mn_4$ compounds. The Sn containing alloy has the highest liquid temperature and it includes α-Mg, $(Ca, Mg)_2Sn$ and Mg_2Sn. Finally Zn containing alloy has the lowest liquid temperature and includes α-Mg, α-Mn, MgZn and $Ca_2Mg_6Zn_3$. However, these phases have been thermodynamically calcualted for the solidification process, it should be considered that the related phases can be transformed to other phases during other homogenization and high temperature extrusion. So the final formed phases were identified using XRD and SEM/EDS analysis.

Fig. 13 shows the XRD profile of different alloys. The XM11 alloy contains α_{Mg}, Mg_2Ca, and α_{Mn}. In the AXM211 alloy, in addition to α phase, $(Mg, Al)_2Ca$ and Al_8Mn_5 were also distinguished. In the TXM911 alloy, observed peaks belong to α_{Mg} and $(Mg, Ca)_2Sn$ compounds. Finally, α_{Mg} and $Ca_2Mg_6Zn_3$ were formed in the ZXM411 alloy.

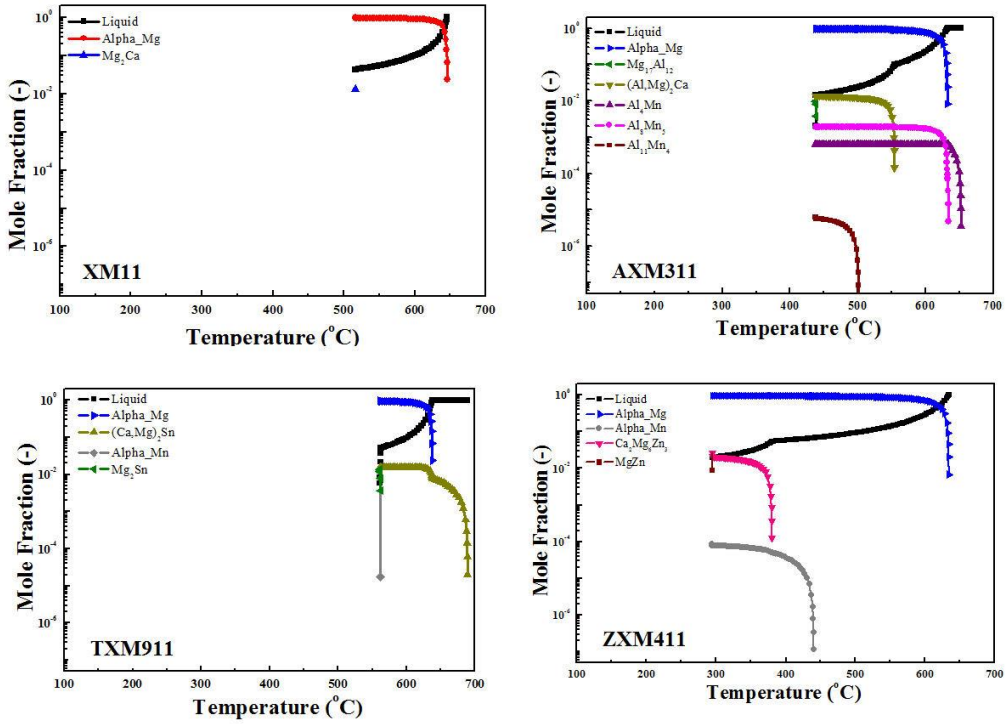

Fig. 12. Predicted phases during solidification using Scheil equation.

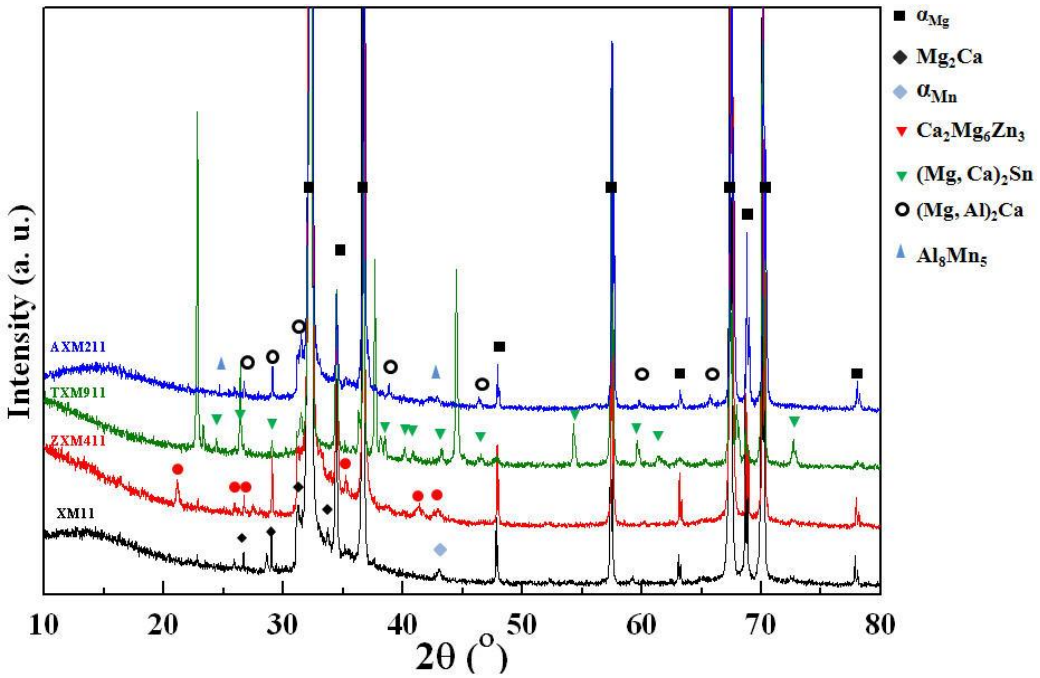

Fig. 13. XRD of extruded alloys of extruded alloys.

SEM/EDS analysis was also utilized as shown in the Fig. 14 to see the morphology and measure the phase fraction of the formed phases. Mg_2Ca and α_{Mn} phase in addition to α_{Mg} as a matrix was seen in XM11 alloy. Al containing alloy includes Al-Mn compounds and $(Mg, Al)_2Ca$ beside α_{Mg}. The Sn containing alloy includes some large and very fine $(Mg, Ca)_2Sn$ phases and finally Zn containing alloy includes some spherical and vermicular $Ca_2Mg_6Zn_3$. The fraction of the phases also was obtained using image analysis of five images from each sample and the related values are listed in the Table 5.

Fig. 15 illustrates the microstructure of the extruded alloys where the extrusion direction is parallel to the normal vector of the observed microstructure plane. It can be seen that Sn addition resulted in many fine particles located inside the grains. The grain size of the alloys as well as their mechanical properties is listed in the Table 3. The grain sizes of different alloys except TXM911 alloy are approximately same while the mentioned alloy has larger grains than the other alloys.

3.3.3 Mechanical properties

Tensile test results of extruded alloys have been shown in Fig. 16 and the related values were listed in the Table 6 Zn containing alloy shows the highest yield and ultimate tensile strength which is related to the role of Zn in grain refinement due to formation of Mg-Zn-Ca compounds which form during solidification of this alloy. Moreover the elongation of Zn containing alloy is higher than that of other alloy which makes it having best mechanical properties among all compared alloy. Another point needs to be considered is that all added alloys increased the elongation of XM11 alloy. In fact, the XM11 alloy did not show any considerable plasticity where it has been softened after yielding unlike other alloys. The lowest yield and ultimate strength belongs to XM11 and after that TXM411 alloys.

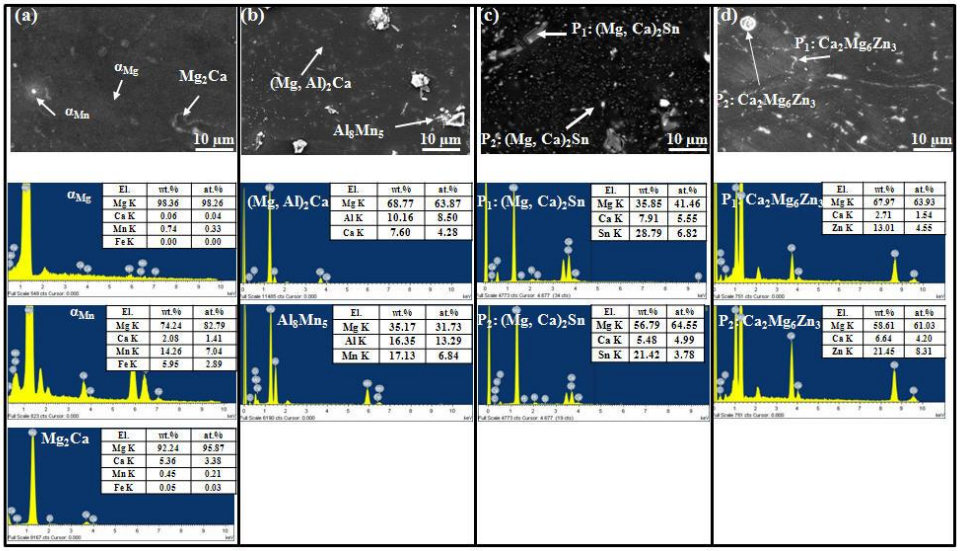

Fig. 14. SEM-EDS analysis of different extruded alloys: (a) XM11, (b) AXM211, (c) TXM911 and (d) ZXM411.

Table 5. Area fraction of the various phases in different studied alloys obtained by image analysis.

	Intermetallic	**$f_{A,i}$**
XM11	Mg_2Ca	0.021±0.003
	α_{Mn}	0.002±0.001
AXM211	$(Mg, Al)_2Ca$	0.076±0.008
	Al_8Mn_5	0.004±0.003
TXM911	$(Mg, Sn)_2Ca$	0.231±0.040
ZXM411	$Ca_2Mg_6Zn_3$	0.087±0.011

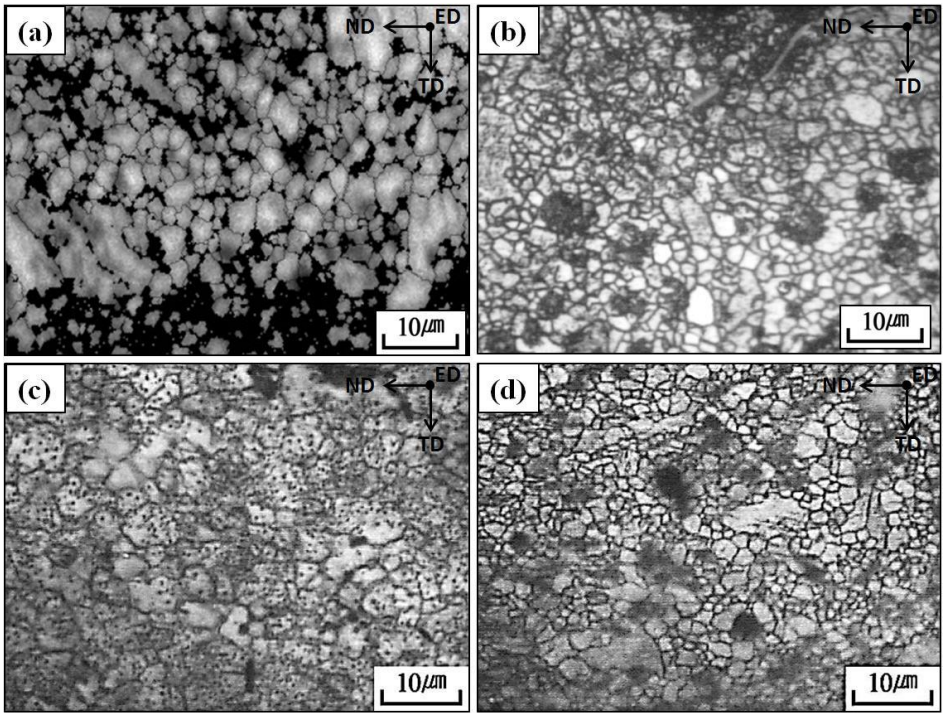

Fig. 15. Microstructure of extruded alloys: (a) XM11 (obtained by EBSD technique), optical microscopy of (b) AXM211, (c) TXM911 and (d) ZXM411.

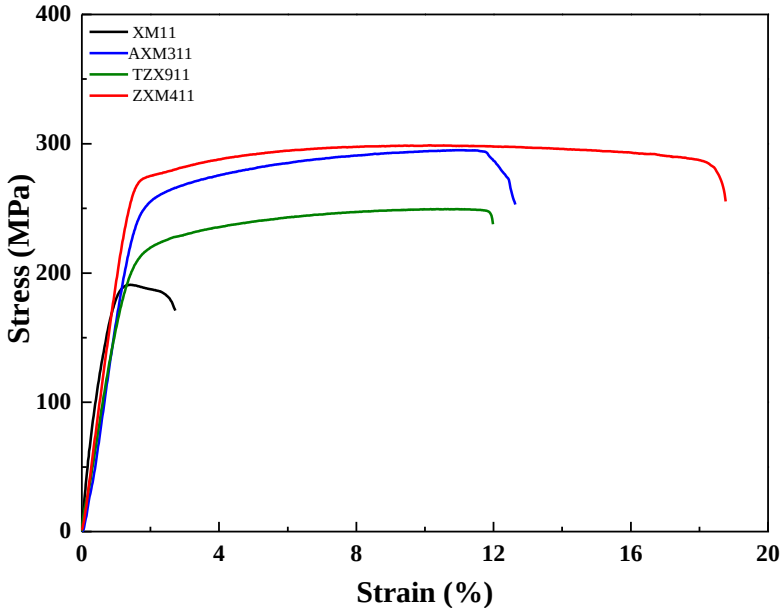

Fig. 16. The strain-stress curved of different extruded alloys.

Table 6. The strain-stress values.

Designation	G.S. (μm)	HV (H_V)	TYS (MPa)	UTS (MPa)	El. (%)
XM11	2.03	79.26	189.5	190.91	2.71
AXM211	2.03	89.91	230.81	295.04	12.64
TXM911	3.81	69.83	205.69	246.28	11.94
ZXM411	1.91	88.01	274.06	293.08	18.73

3.3.4 Corrosion behavior

Fig. 17 shows the hydrogen evolution and corresponding corrosion rate of the studied extruded alloys in seven days. Sn containing alloy have the highest corrosion rate while the lowest values are related to XM11 alloy which can be mainly explained through the lower amount of secondary phases and hence lower amount of galvanic cells. Table 7 also shows all results of corrosion rates through hydrogen evolution, weight loss and Tafel studies where the same trend of corrosion rate was observed for all alloys. Fig. 18 depicts the surface appearance of alloys immersed for seven days after removing corrosion products by a solution of 200 g/l CrO_3 and 10g/l $AgNO_3$ mixed with distilled water. As can be seen, the XM11 alloy has the most unchanged surface after immersion while AXM211 has suffered several pits. Alloy TXM911 have been corroded severely from all parts. The surface of the alloy ZXM411 looks less corroded comparing to AXM211 and TXM911 alloys. However some signs of pits can be observed in SEM image.

Current density can be considered as a parameter representing the corrosion rate as shown in the Eq. (1). Regarding to the Tafel curves it is obvious that XM11 and ZXM411 alloys have the lower corrosion current density comparing to TXM911 and AXM211. The very low anodic slopes of these two alloys show their high anodic activities and magnesium matrix dissolution. Moreover all three alloys of AXM211, TXM911 and ZXM411 are nobler than XM11 showing three elements of Al, Sn and Zn makes the alloy nobler.

The related values of hydrogen evolution, weight loss and Tafel study have been listed in Table 7. As can be seen there exist an agreement between the trend of corrosion resistance which have been obtained by different methods while it is in the sequence of XM11, ZXM411, AXM211 and TXM911.

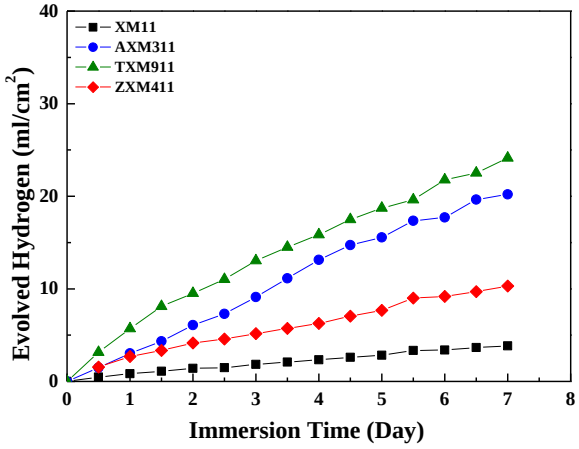

(a)

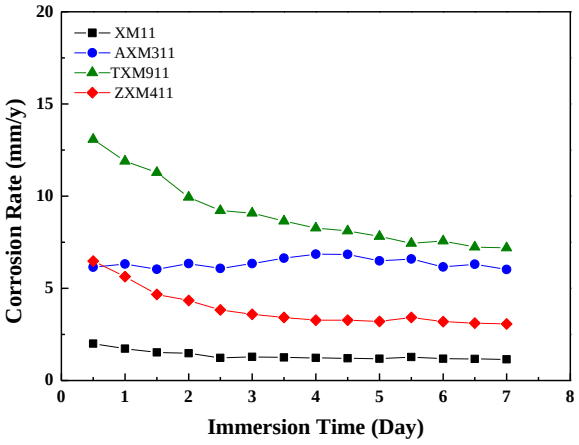

(b)

Fig. 17. Immersion study of the studied extruded alloys: (a) hydrogen volume and (b) related corrosion rates.

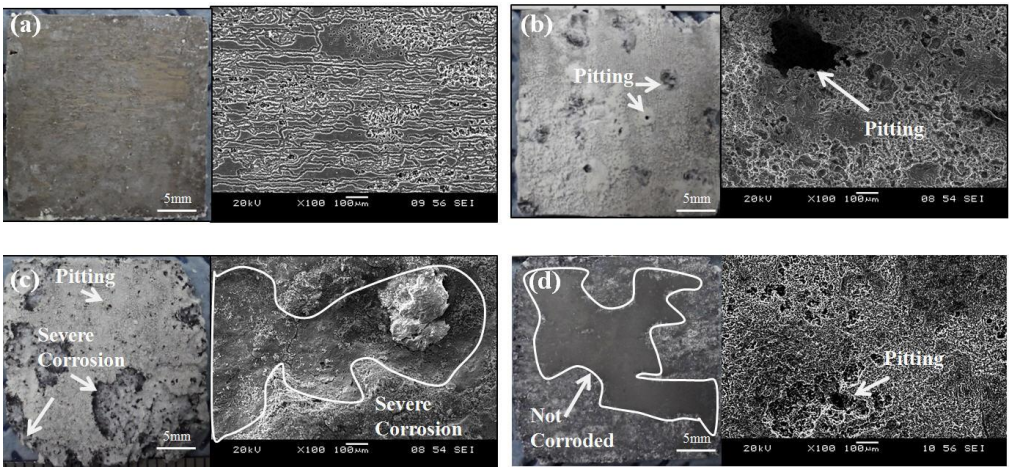

Fig. 18. Surface appearance after immersion testing for 7 days of different alloys after removing corrosion products for: (a) XM11, (b) AXM211, and (c) TXM911 and (d) ZXM411.

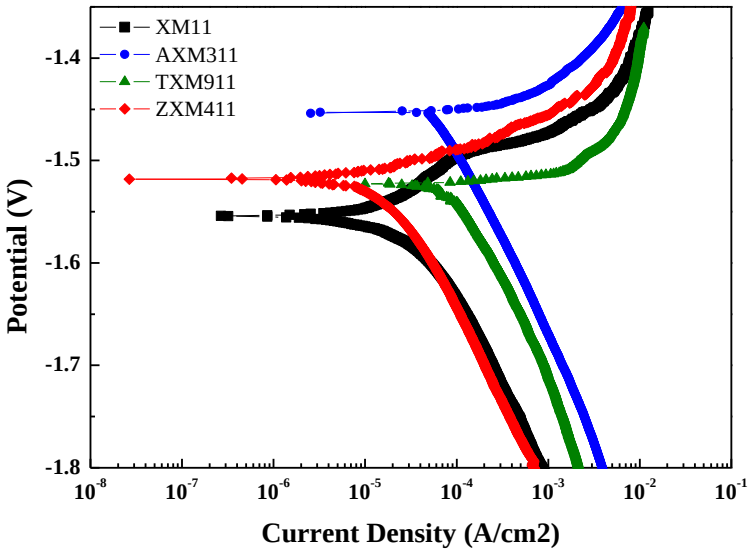

Fig. 19. Polarization curves in the 3.5% NaCl solution saturated with $Mg(OH)_2$.

Table 7. Corrosion values of alloys using hydrogen evolution, weight loss and electrochemical methods.

	Hydrogen Evolution		**Weight Loss**		**Electropotential**		
Alloy	**Evolved Hydrogen (ml/cm2)**	**Corrosion Rate: P_H (mm/y)**	**Weight Loss (mg/cm^2/ d)**	**Corrosion Rate: P_W (mm/y)**	**i_{corr} ($\mu m/cm^2$)**	**E_{corr} (V)**	**Corrosion Rate: P_i (mm/y)**
XM11	3.84	1.14	0.80	1.69	23.3	-1.552	0.53
AXM211	20.21	6.03	4.12	8.66	51.4	-1.452	1.83
TXM911	21.12	7.19	4.18	8.77	86.5	-1.522	1.97
ZXM411	10.30	3.07	1.73	3.63	27.5	-1.518	0.62

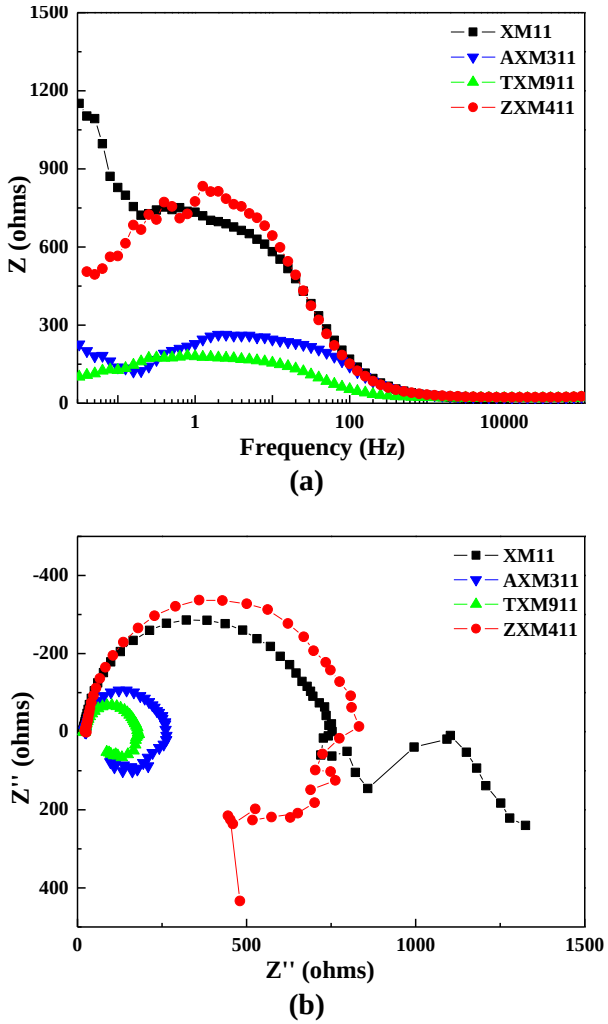

Fig. 20. Bode and nyquist plots for the corrosion of alloys in 3.5 wt. % NaCl saturated with $Mg(OH)_2$.

The EIS plots for the corrosion of different alloys have been shown in the Fig. 20. In this graph higher radius of imaginary versus real resistance, is related to corrosion resistance of the alloy. The XM11 and ZXM411 alloys have higher radius than that of Sn and Al containing alloys. However, it can be seen than ZXM411 alloy have higher resistance than XM11 alloy in high frequencies but at low frequencies its resistance has been decreased where the resistance of XM11 has been increased. It shows that in low frequencies, the surface layer of this alloy has been corrupted regarding to pitting phenomena. In a same trend the surface bod plot of TXM911 and AXM211 alloys show a surface layer corruption in low frequencies.

According to phase formation calculated by Pandat software, Mn containing particles such as Al_8Mn_5 form at the early stages of solidification and so they distribute through the as-cast matrix while $(Mg, Al)_2Ca$ intermetallic compounds form later on steps of solidification and hence locate on grain boundaries of as-cast sample, through the deformation process they can be rearranged as a continuous phases alongside the extrusion direction as a continuous galvanic cells and hence introduce the corrosive solution into the metal. Mn containing intermetallic compounds has cathodic effect for the matrix [4] but due to their low fraction, they do not accelerate the corrosion rate effectively. Sn containing compounds functions as cathodic compounds due to their high potential difference with matrix. Since these Sn containing fine particles have been distributed very well in the matrix the corrosive solution can be introduced into the metal very fast. The droplet test was carried out on different alloys to understand their corrosion behavior. In the case of AXM211, it can be seen that corrosion is propagates through the matrix dissolving the $(Mg, Al)_2Ca$ anodic compounds while Al-Mn compounds acts as a cathodic site and caused the matrix to be dissolved around these compounds. Very fine Mg-Sn-Ca distributed in the matrix of TXM911 alloy also played an anodic role and their close distance caused the corrosion to be accelerated by dissolving these compounds. The corrosion behavior of ZXM411 alloy can be explained through the dissolution of $Ca_2Mg_6Zn_3$ compounds which have been elongated alongside the

extrusion direction. As can been seen in the Fig. 21, solution has changed its progression path to another elongated $Ca_2Mg_6Zn_3$ phase.

For quantifying the corrosion rate (based upon the hydrogen evolution) of the materials with the structural parameters, SKPFM method was utilized to measure the volta-potential of intermetallics and matrix of different materials. Moreover, image analysis technique using ImageTools software was used to measure the phase fraction of the intermetallics. So based upon the galvanic corrosion which happened between intermetallic compounds and matrix, the corrosion rate versus $f_{A,i} \times |\Delta E|$ was drawn in the Fig. 23. The related values also have been listed in the Table 8.

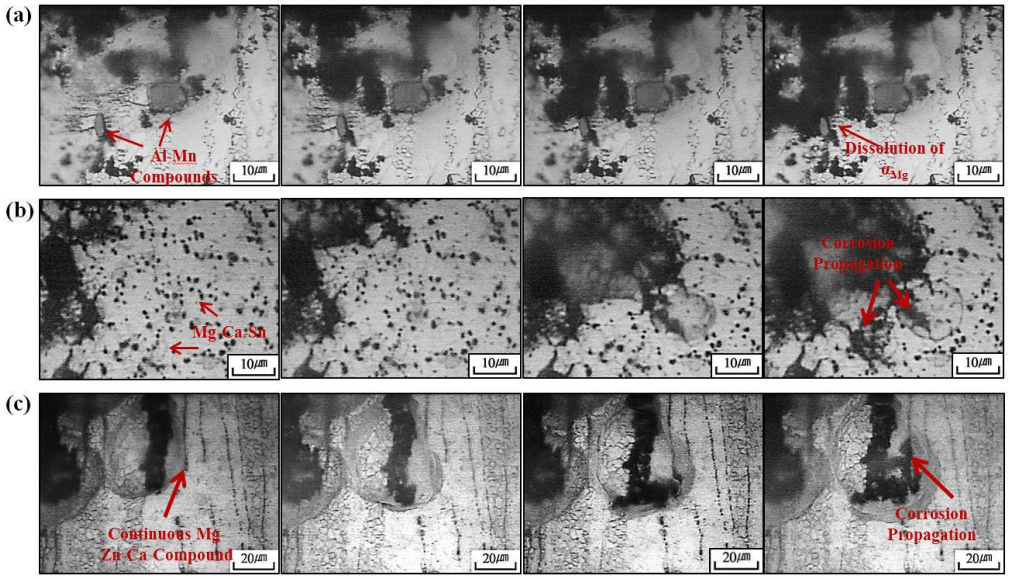

Fig. 21. Progression of corrosion in 3.5 wt.% NaCl saturated with $Mg(OH)_2$: (a) ZXM411, (b) TXM911 and (c) AXM211 alloys.

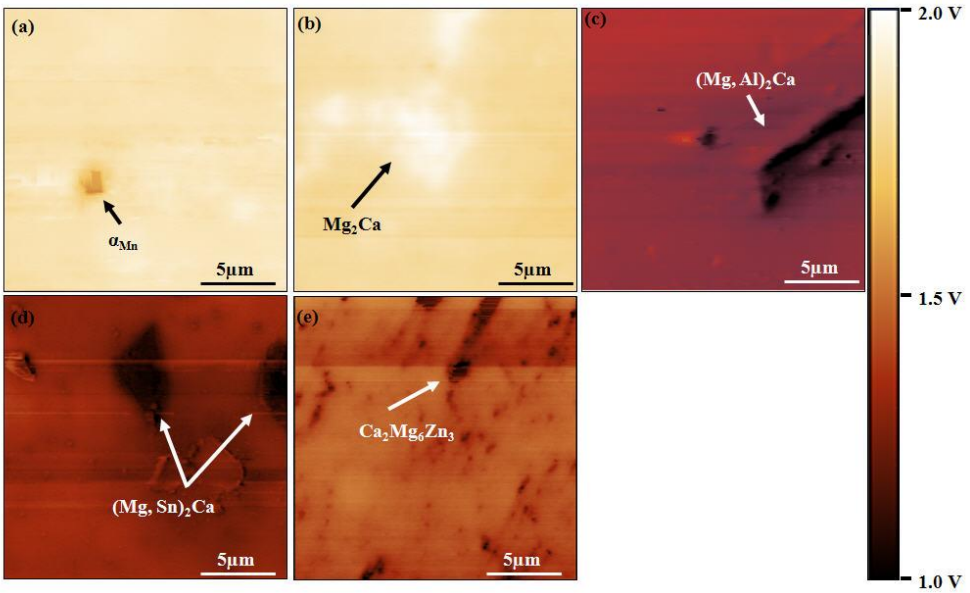

Fig. 22. SKPFM images: (a) and (b) XM11, (c) AXM211, (d) TXM911, (e) ZXM411.

Table 8. The volta-potential values of XM11, AXM211, TXM911 and ZXM411 alloys.

	Intermetallic	**E_α**	**E_i**	**$\Delta E = E_\alpha - E_i$**	**$f_{A,i}$**	**$f_{A,i} \times \lvert\Delta E\rvert$**
Platinum	-	210.26±10	-	-	-	-
Pure Mg	-	1720.23±25	-	-	-	-
XM11	Mg_2Ca	1810.98±13	1936.40±20	-126.42	0.021	2.65
AXM211	$(Mg, Al)_2Ca$	1303.33±35	770.01±70	533.33	0.076	40.67
	Al_8Mn_5		963.10±70	340.23	~0.004	
TXM911	$(Mg, Sn)_2Ca$	1276.66±07	1021.75±33	254.92	0.231	58.63
ZXM411	$Ca_2Mg_6Zn_3$	1456.31±64	1060.72±94	396.05	0.087	32.87

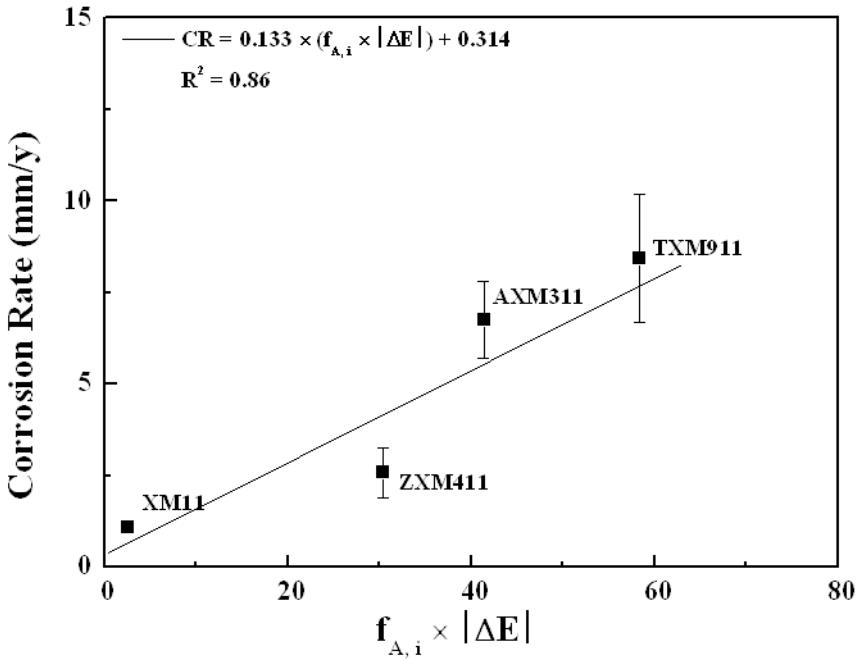

Fig. 23. Relationship between corrosion rate and Volta-potential difference and intermetallic phase fraction of extruded and MDFed alloys.

According to the volta-potential and phase fraction study (Table 8 and Table 5) it can be seen that Mg_2Ca in the XM11 alloy is anodic relative to the matrix because Ca has a work function value less than that of Mg. But addition of the alloying elements such as Al, Sn and Zn changed the identity of the intermetallics to cathodic against the matrix because all of these three elements have work function than that of Mg. So during the corrosion process, Mg_2Ca dissolves first and protect the matrix against corrosion. The other important factor need to be considered is the potential difference between the matrix and intermetallics, because this parameter determines the rate of degradation around intermetallics. Since the intermetallic compounds in the AXM211, TXM911 and ZXM411 alloys are cathodic, the matrix around the intermetallics would be degraded regarding to the potential difference and also the fraction of the intermetallics. $(Mg, Al)_2Ca$ in the AXM211 alloy show the highest difference with the matrix among all measured intermetallics. That is why the corrosion rate of this alloy is high and very deep pits have been formed in this alloy (Fig. 18). $(Mg, Ca)_2Sn$ in the TXM911 alloy has low potential difference with the matrix but the fraction of this phase is high and so the total area which is affected by the corrosion is more than other alloys. Therefore surface appearance of the TXM911 after seven day immersion (Fig. 18) depicts severe corrosion which is not localized. So the unstable passive layer in the AXM211 and TXM911 alloys which was observed in the Fig. 20 is related to high volta-potential difference of the $(Mg, Al)_2Ca$ and high area fraction of the $(Mg, Ca)_2Sn$, respectively. The $\Sigma(f_{A,i} \times |\Delta E|)$ value of the ZXM411 alloy is less than that of AXM211 and TXM911 alloys and so ZXM411 alloy corrodes less than them.

3.4.1 Summary

Four alloys namely XM11, AXM211, TXM911 and ZXM411 with almost similar grain size produced using extrusion and their mechanical properties and corrosion behavior were studied. The best combination of corrosion properties and mechanical properties was found in ZXM411 alloy however, XM11 alloy has the best corrosion resistance due to the presence of relatively small amount of secondary phases. The following results were obtained:

-The tensile yield strength of the alloys decreased in the order of ZXM411, AXM311, TXM411 and XM11 and the corrosion resistance of them decreased in the order of XM11, ZXM411, AXM311 and TXM911.

-Zn, Al and Sn improved the yield strength of XM11 regarding to formation of more second phase based on precipitate hardening mechanism.

-The volta-potential study using SKPFM and phase fraction measurement using image analysis showed that Mg_2Ca in XM11 alloy is anode relative to the matrix while other intermetallics in the other alloys are cathode. The study shows that increase in the area fraction of second phase and therefore galvanic cells after addition of 9.0 wt. % (2.0 at. %) Sn is responsible for the high corrosion rate of TXM911 alloy while addition of 2.4 wt. % (2.0 at. %) Al resulted in the formation of $(Mg, Al)_2Ca$ with high volta-potential difference and so this alloy also has a high corrosion rate. In the case of ZXM411, the $f_{A,\,i} \times |\Delta E|$ (intermetallic area fraction × absolute value of volta-potential difference) value is lower than that of AXM211 and TXM911 and so this alloy has lower corrosion rate.

-The corrosion rate of the alloys after seven day immersion was quantitatively compared with the fraction and volta-potential difference between intermetallic and matrix and a proportionally good agreement was found.

3.6 Effect of Ca on mechanical properties and corrosion behavior

As shown in the Fig. 24, Ca addition in ZAM421 alloy, resulted in decreasing the grain size and hence increasing the yield strength, hardness and UTS. In an opposite trend, the elongation was decreased. In the case of corrosion behavior, addition of Ca in the ZAM421 from 0.0 to 0.6 wt.%, no significant change was observed , but the addition of this element to 1.2 wt.% increased the corrosion rate suddenly while in the same way the yield strength was suddenly also increased. The corrosion rate versus $\Sigma(f_{A,i}\times|\Delta E|)$ has been drawn in the Fig. 25. A proportionally good agreement can be find here, showing the corrosion rate increase by adding Ca is related to the increase in the fraction of the second phase and increasing the number of galvanic cells.

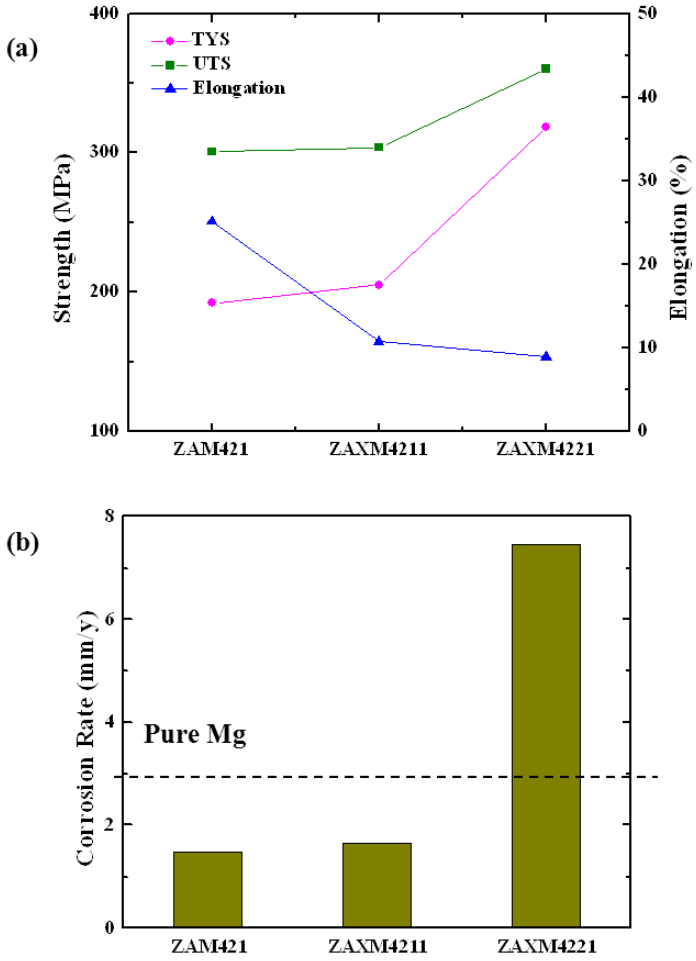

Fig. 24. Effect of Ca on mechanic properties and corrosion behavior of ZAM421 alloy: (a) mechanical properties and (b) corrosion rate.

Table 9. Volta-potential study of ZAM421, ZAXM4211 and ZAXM4221.

	Intermetallic	E_α (mV)	E_i (mV)	$\Delta E = E_\alpha - E_i$ (mV)	$f_{A,i}$ (%)	$\Sigma(f_{A,i} \times \lvert\Delta E\rvert)$
ZAM421	Al_8Mn_5	1225.41±70	820.10±85	405.31	0.016	6.32
ZAXM4211	$(Mg, Al)_2Ca$	1297.67±23	910.12±34	387.55	0.053	21.63
	Al_8Mn_5		980.53±18	317.14	0.005	
ZAXM4221	Φ ($Al_5Mg_{11}Zn_4$) + $(Mg, Al)_2Ca$	1556.67±56	1168	388.67±56	0.147	57.25
	Al_8Mn_5		910.12±34	-	0.005	

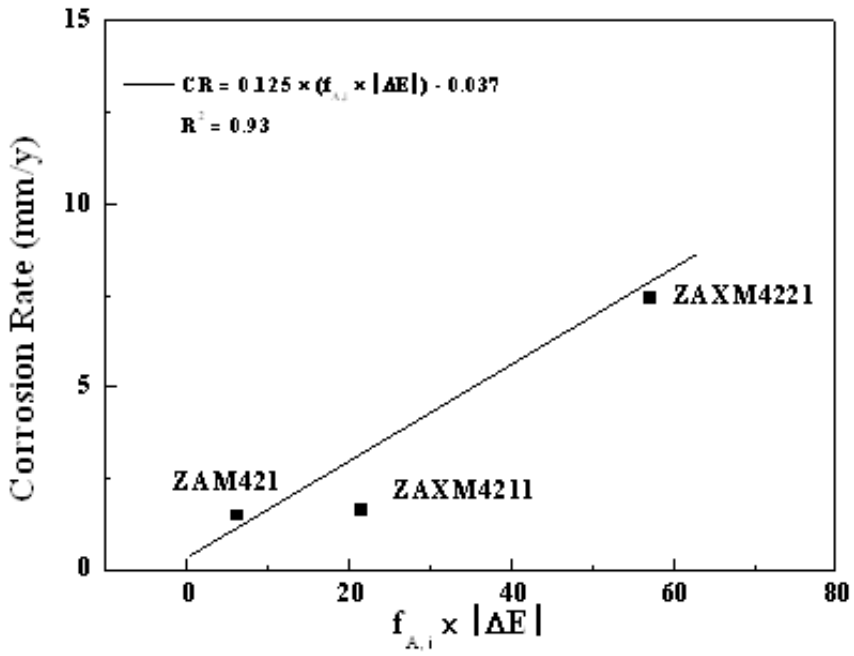

Fig. 25. The relationship between corrosion rate and $f_{A,i} \times |\Delta E|$.

3.7 Improvement of mechanical properties and corrosion behavior of a magnesium alloy using screw rolling (SR)

3.7.1 Microstructure

To know the different formed secondary phases, XRD, thermodynamic calculation and SEM/EDS analysis were utilized. Fig. 26 shows the XRD profile of ZAXM4211 alloy which consist of α_{Mg}, $(Mg, Al)_2Ca$,, MgZn and Al_8Mn_5 phases.

Moreover, steady state thermodynamic calculations (Fig. 27) shows ZAXM4211 alloy contains $(Mg, Al)_2Ca$, MgZn and Al-Mn compounds. MgZn phase is not stable at high temperature and it disappears at temperatures higher than 180 ^oC. The fraction of $(Mg, Al)_2Ca$ gradually decreases with increasing the temperature because the solubility of Al and Ca in the matrix increases. Fig. 27 (b) shows the solubility of the elements in the α_{Mg}. Zn content does not change in the temperature range in which SR have been carried out, while Al and Ca content gradually increases with SR temperature increase.

SEM/EDS analysis was also utilized as shown in Fig. 28 to see the morphology and measure the phase fraction of the formed phases. The phases includes $(Mg, Al)_2Ca$ with MgZn and Al_8Mn_5 phase in addition to α_{Mg}. It was found using SEM that all Mn excluding phases includes Mg, Al, Ca and Zn. The Al_8Mn_5 compounds have sharp morphology with flat interface with the matrix and in this regard, they can be distinguished from $(Mg, Al)_2Ca$+ MgZn phases.

Second phase and grains distribution of the extruded sample in addition to those screw rolled at different temperatures have been presented in

Fig. 29. As it can be seen grains have been refined effectively at lower temperatures and enlarged at higher SR temperatures due to dynamic recrystallization and growth phenomena. Moreover the second phase amount was reduced by increasing the SR temperature due to dissolution of the added elements into the matrix. The area fraction of the second phases after image analysis by ImageTools software was

shown in the Table 10. The average area fractions have been obtained by measuring five images from each sample. The results shows that intermetallic phases like ((Mg, $Al)_2Ca$ and MgZn) dissolve into the matrix, because they have more solubility in the matrix at higher SR temperatures.

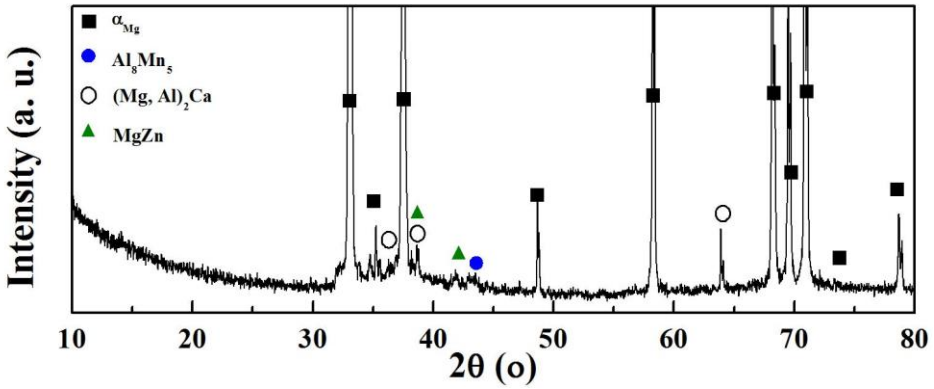

Fig. 26. XRD profile of the ZAXM4211 alloy.

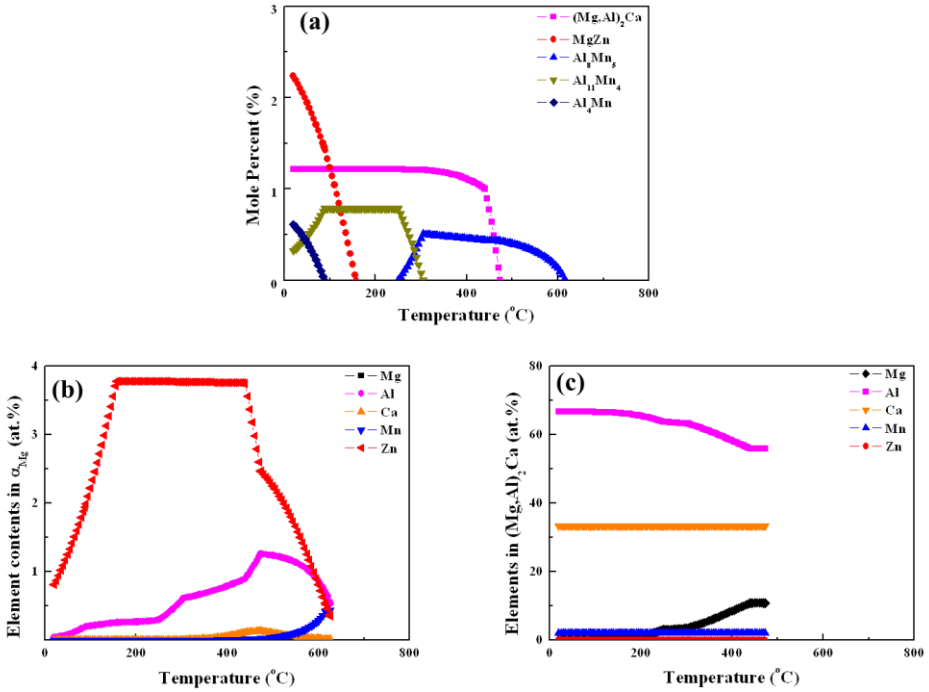

Fig. 27. Phases percent in different temperatures: (a) steady state thermodynamic calculation using JMatPro commercial software, (b) phases percent obtained by image analysis technique using ImageTools software.

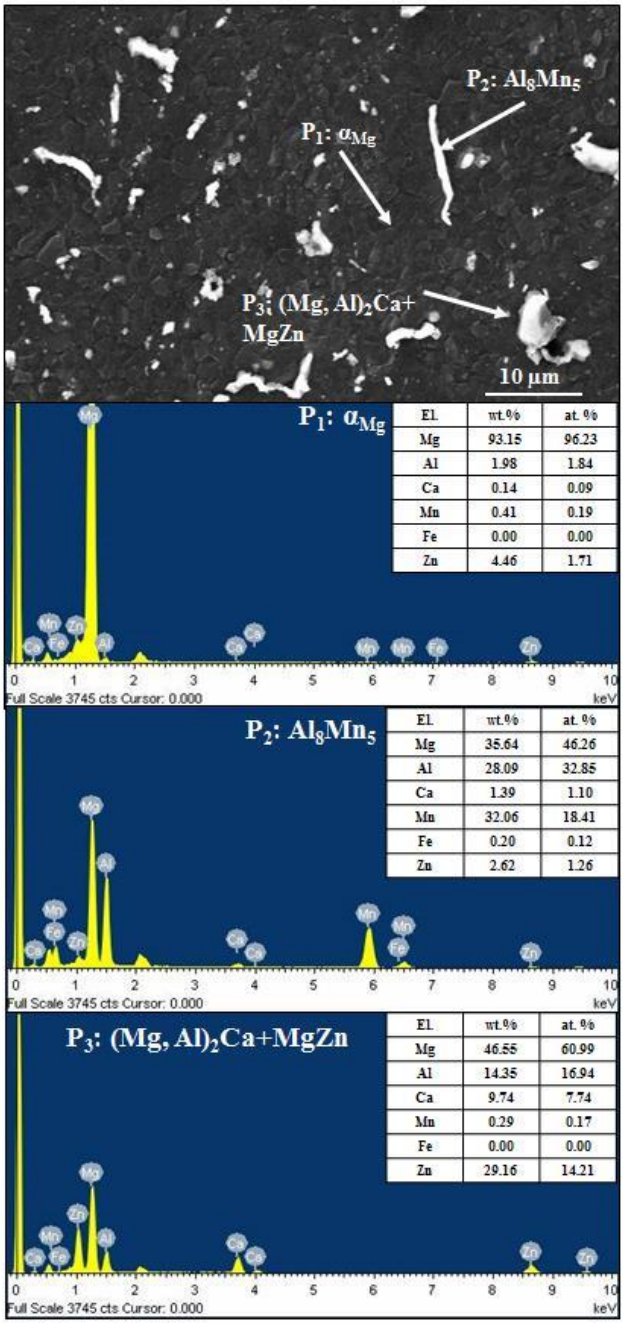

Fig. 28. SEM/EDS analysis of the phases formed in the ZAXM4211 alloy.

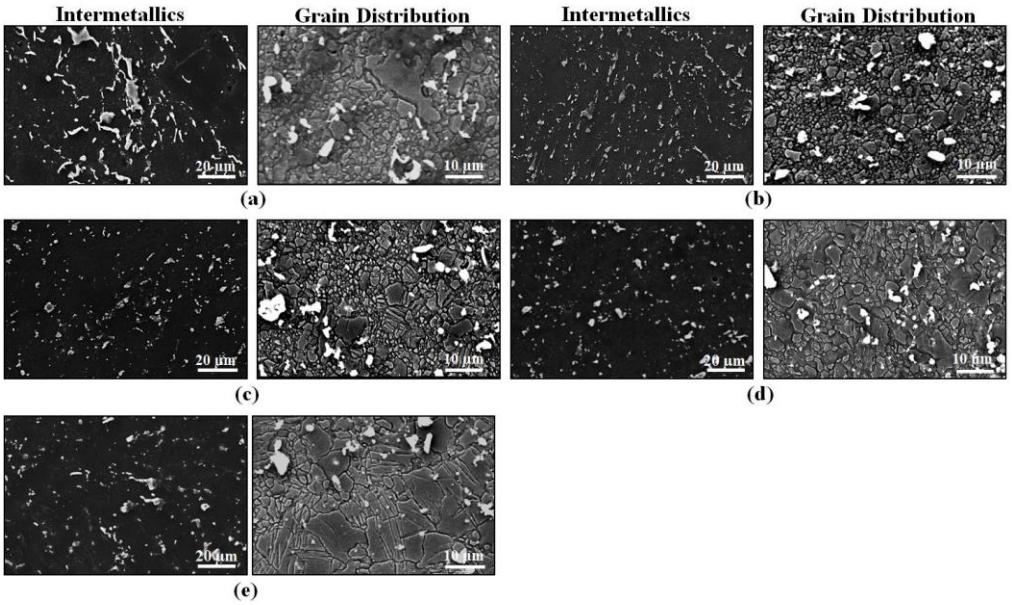

Fig. 29. Grain and second phase distribution: (a) Extrusion, (b) SR220, (c) SR260, (d) SR300 and (e) SR340.

Table 10. Area fraction of the formed phases in the extruded and SRed ZAXM4211 alloy.

	Intermetallic	$\mathbf{f_{A,\,i}}$
ZAXM4211/ Extrusion	**$(Mg, Al)_2Ca$+MgZn**	**0.088**
	Al_8Mn_5	**~0.005**
ZAXM4211/ SR220	**$(Mg, Al)_2Ca$+MgZn**	**0.074**
	Al_8Mn_5	**~0.005**
ZAXM4211/ SR260	**$(Mg, Al)_2Ca$+MgZn**	**0.065**
	Al_8Mn_5	**~0.005**
ZAXM4211/ SR300	**$(Mg, Al)_2Ca$+MgZn**	**0.052**
	Al_8Mn_5	**~0.005**
ZAXM4211/ SR340	**$(Mg, Al)_2Ca$+MgZn**	**0.0461**
	Al_8Mn_5	**~0.005**

3.7.2 Mechanical Properties

The tensile curves of extruded and screw rolled samples have been shown in Fig. 30 and the related properties have been listed in Table 11. As it can be seen, tensile yield strength and Vickers hardness values have been increased by grain size reduction. Grain boundaries play an important role in impeding dislocations propagation and in this regard SR220 sample having the most grain boundaries, showed the highest yield strength, ultimate tensile strength and hardness.

3.7.3 Corrosion Behavior

Fig. 32 shows the hydrogen evolution and corresponding corrosion rate of extruded and screw rolled alloys in seven days. The evolved hydrogen and hence corrosion rate of screw rolled samples are obviously less than that of extruded alloy and among screw rolled samples, those produced at 300 ^{o}C show lowest corrosion rate. The corrosion rate of the alloys using hydrogen evolution and weight loss methods have been listed in

Table 12 showing same trend of corrosion rate for both methods.

SEM Images of the seven day immersed samples have been shown in Fig. 33. It can be seen that the corrosion products at the surface of SR300 sample is less voluminous than the other samples where there are areas with less corrosion products. The less corroded areas which formed in SR260 and SR300 samples are specified by a line around them. Moreover the areas with voluminous corrosion products are shown using small vectors.

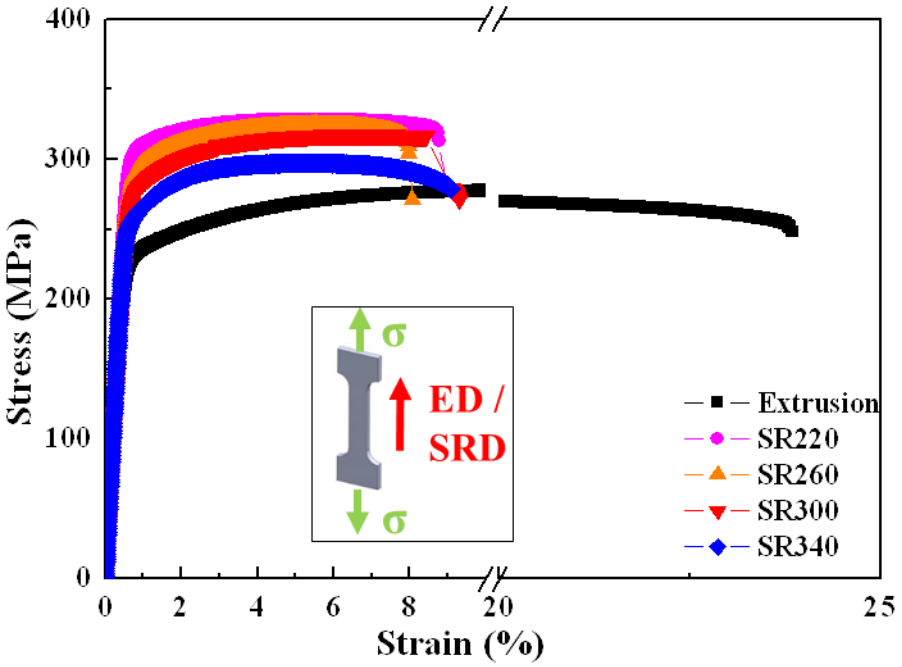

Fig. 30. Mechanical properties of the screw rolled samples.

Table 11. Mechanical properties of the screw rolled samples.

Sample	D(μm)	Hardness (H_V)	YS (MPa)	UTS (MPa)	El. (%)
Extrusion	2.8	87.9	225.3	278.0	23.9
SR220	1.7	124.9	308.6	327.4	8.3
SR260	2.0	115.8	289.4	322.1	7.7
SR300	2.5	113.5	272.7	317.1	8.3
SR340	5.9	85.4	255.4	295.6	8.5

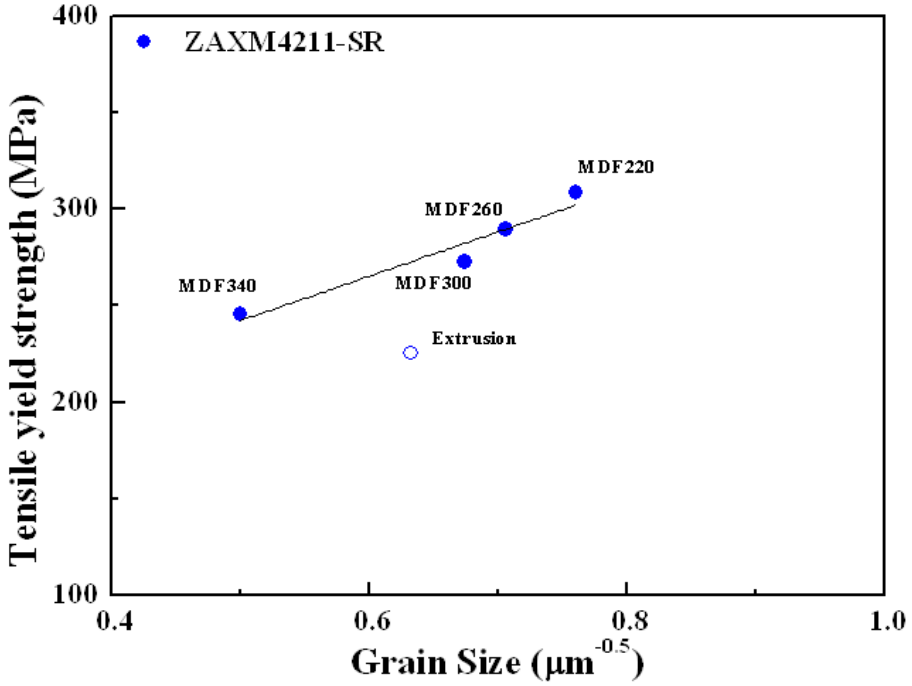

Fig. 31. The relationship between tensile yield strength and grain size of screw rolled samples.

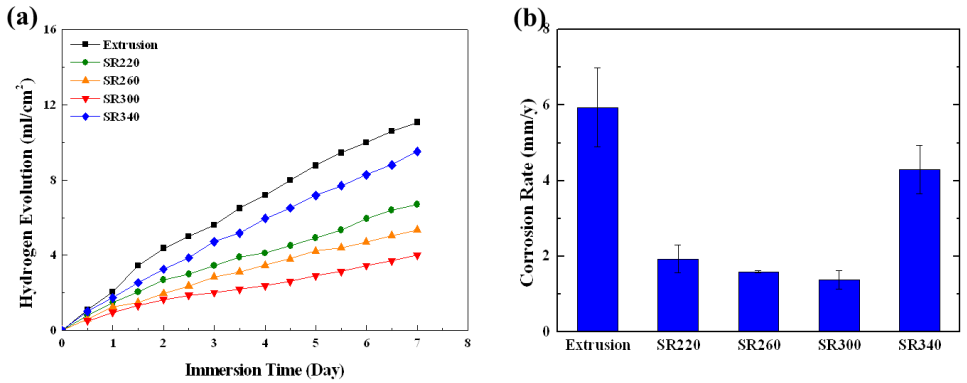

Fig. 32. Immersion study in 3.5 wt. % NaCl with saturated $Mg(OH)_2$: (a) volume of evolved hydrogen during immersion and (b) average corrosion rate.

Table 12. Hydrogen volume and weight loss study data of extruded and SRed samples in the 3.5 wt. % NaCl solution saturated with $Mg(OH)_2$ (P_H and P_W are the corrosion rates measured by hydrogen evolution and weight loss methods, respectively).

Sample	**Evolved Hydrogen (ml/cm^2)**	**Corrosion Rate P_H (mm/y)**	**Weight Loss ($mg/cm^2/d$)**	**Corrosion Rate P_W (mm/y)**
Extrusion	19.91	5.94	3.72	7.82
SR220	6.47	1.93	2.38	4.99
SR260	5.33	1.59	1.42	2.99
SR300	4.61	1.38	1.24	2.60
SR340	14.40	4.30	2.63	5.52

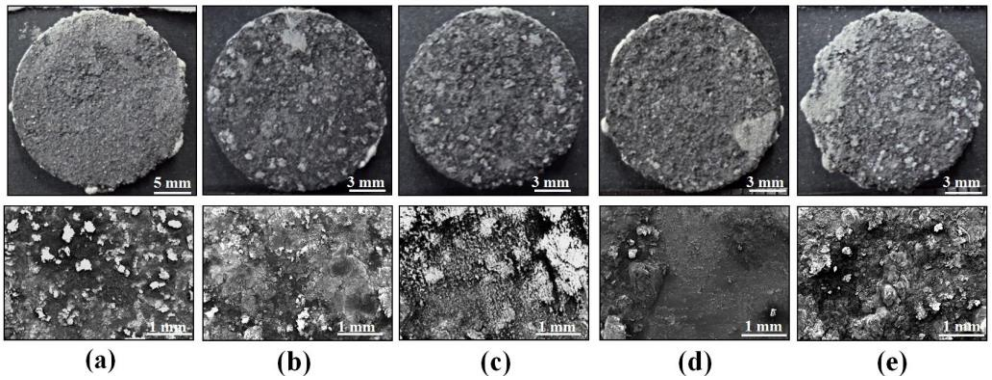

Fig. 33. Photographic and SEM images after corrosion: (a) Extrusion, (b) SR220, (c) SR260, (d) SR300 and (e) SR340.

Potentiodynamic polarization studies were carried out and the Tafel plots have been shown in Fig. 34. As it was mentioned through the Equation 1, i_{corr} shows alloy corrosion rate regarding to degradation of Mg atoms. The i_{corr} values obtained from Tafel shows that screw rolled samples significantly improved the corrosion resistance of this alloy which had been proved through hydrogen evolution and weight loss studies (

Table 12). The samples screw rolled at higher temperatures have less corrosion rate and the minimum corrosion rate was obtained on the sample processed at 300 ^{o}C, however the corrosion rate was increased again for the sample processed at 340 ^{o}C which is in agreement with the hydrogen evolution and weight loss methods.

The Nyquist plot has been shown in Fig. 34 (b). The capacitive loop at the high frequency region indicates the charge transfer reaction on the sample surface and electrolyte, and the dimension of capacitance loop determines the charge transfer resistance. The diameter of high frequency capacitance loop of screw rolled samples except SR340 are larger than that of the extruded, indicating that the charge transfer resistance has remarkably decreased after screw rolled and in particular after high temperature screw rolling, however it has been significantly reduced after screw rolling at 340 ^{o}C. The bode plot (Fig. 34 (c)) shows a drop for all samples in low frequencies except SR300 which is related to passive layers being locally destroyed. It can be seen in SR300 sample the resistance of surface layer has been increased even in low frequencies showing more resistance of this materials against destroy of surface layer.

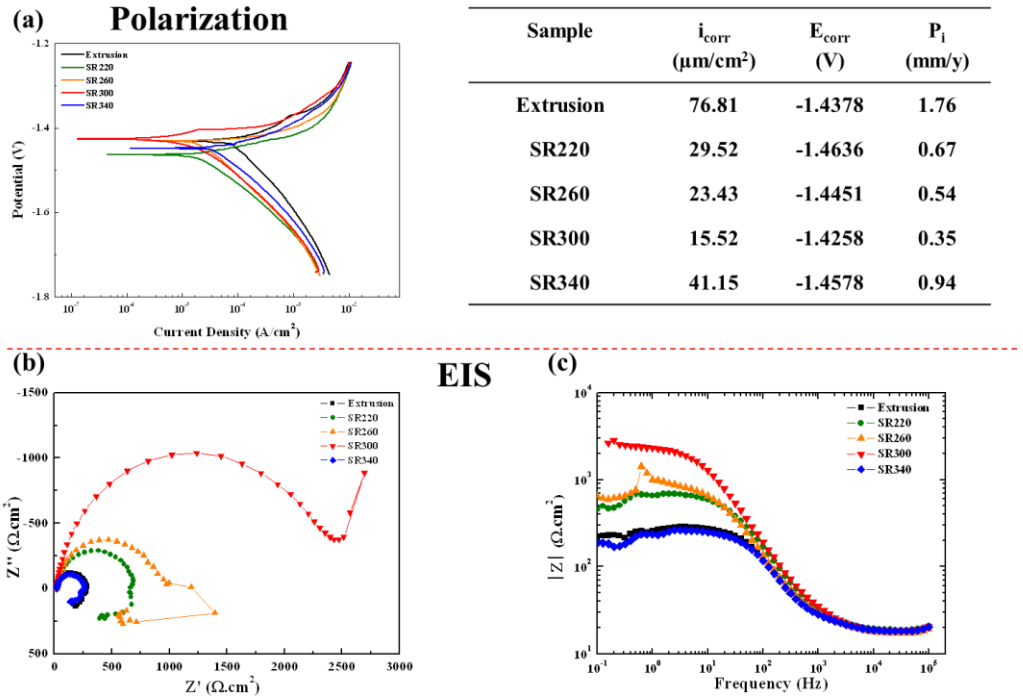

Sample	i_{corr} (µm/cm²)	E_{corr} (V)	P_i (mm/y)
Extrusion	76.81	-1.4378	1.76
SR220	29.52	-1.4636	0.67
SR260	23.43	-1.4451	0.54
SR300	15.52	-1.4258	0.35
SR340	41.15	-1.4578	0.94

Fig. 34. Electrochemical study of extruded and SRed ZAXM4211 alloy: (a) Tafel, (b) Bode and (c) Nyquist plots.

For analyzing the mechanism of the corrosion modification, SKPFM method was utilized to measure the volta-potential difference of the intermetallics and matrix. Moreover, image analysis technique using ImageTools software was used to measure the phase fraction of the intermetallics. The volta-potential of the (Mg, $Al)_2Ca$+MgZn and Al_8Mn_5 and their volta-potential difference with the matrix have been shown in the Fig. 35.

Comparing the result with a pure Mg and Pt (Table 13) it can be seen that both types of precipitates are nobler than matrix and so they function as a cathode against matrix.

To see the corrosion progress and their reaction with the intermetallic phases, samples were immersed for 3 h in a 3.5 wt.% NaCl solution saturated with $Mg(OH)_2$ and then corrosion products was removed using the solution of 200 g/l CrO_3 and 10g/l.

Fig. 36 shows the FE-SEM images of these surfaces in two magnifications. The SEM images of the 3h immersed samples confirm SKPFM results while all precipitates are cathodic relative to the matrix and make the matrix be corroded. So corrosion initiates from the interface between intermetallics and α_{Mg}, then hydroxide layer form on the exposed surface and hence decreases the corrosion rate of that region. Therefore corrosion propagates on the matrix surface as a filiform corrosion between the intermetallics while the grain boundaries are being corroded and hydroxide film is being formed. After the surface was fully covered by the protective hydroxide film, the corrosion rate reduces and gets stable. It should be considered not only the galvanic corrosion between intermetallic and matrix determines the corrosion behavior, but also the matrix microstructure plays an important role in the corrosion behavior of the mg alloy. As it was mentioned in the section of introduction, majority of the researches in the corrosion property of pure Mg and in general pure metals prove that corrosion rate increases with increasing the grain size regarding to the formation of a more coherent and uniform film on the surface of pure magnesium as well as other pure metals. So it can be concluded that

there are two controversial effects when processing temperature increases. First one is a decrease in the area fraction of the second phase via dissolution of the intermetallics into the matrix and hence decrease in the galvanic corrosion and the second one is an increase the grain size and hence formation of less coherent surface film.

To evaluate the effect of both parameters in the corrosion, corrosion rate versus grain size (D) and $\sum(f_{A,i}\times|\Delta E|)$ was drawn in the Fig. 37. Here, $f_{A,i}$ is the area fraction of intermetallic and $|\Delta E|$ is the absolute value of the volta-potential difference between intermetallic and matrix. It can be seen that corrosion rate increases when $\sum(f_{A,i}\times|\Delta E|)$ increases (Fig. 37 (a)), but in the case of SR340, even though the fraction of the second phases has been reduced, the corrosion rate has been increased. The effect of corrosion rate versus D (Fig. 37(b)) also depicts that increase in the grain size by increasing the SR temperature from 220 to 300 ^{o}C, decreases the corrosion rate while increasing the grain size by increasing the SR temperature from 300 to 340 ^{o}C increases the corrosion rate. Finally the corrosion rate was drawn versus the combination of the mentioned parameters (Fig. 37 (c)) where both parameters can be explained through one linear curve. In overall, it can be concluded that corrosion rate of the studied alloys is under the control of two main factors including the area fraction of the intermetallics and grain size that both of them changes by changing the temperature.

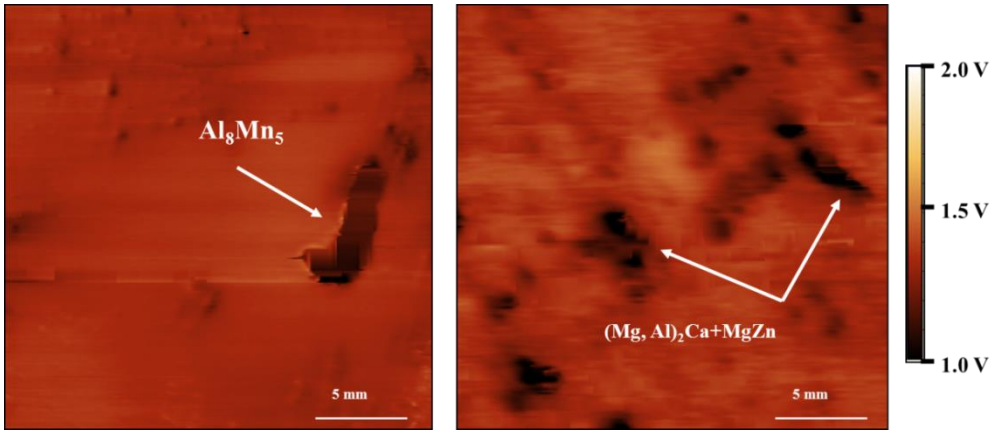

Fig. 35. Volta-potential distribution on the samples surface: (a) Al_8Mn_5 phase, (b) $(Mg, Al)_2Ca$+MgZn of the SKPFM images.

Table 13. Volta-potential study of extruded and screw rolled ZAXM4211alloy.

	Intermetallic	**E_α**	**E_i**	**$\Delta E=E_\alpha-E_i$**	**$f_{A,i}$**	**$f_{A,i}\times\sum\lvert\Delta E\rvert$**
Platinum	-	210.26±10	-	-	-	-
Pure Mg	-	1720.23±25	-	-	-	-
ZAXM4211/ Extrusion	$(Mg, Al)_2Ca$+MgZn	1405±23	913±54	492	0.088	43.59
	Al_8Mn_5		1060±34	345	0.005	
ZAXM4211/ SR180	$(Mg, Al)_2Ca$+MgZn	1406±36	913±39	505.5	0.088	44.93
	Al_8Mn_5		-	-	0.005	
ZAXM4211/ SR220	$(Mg, Al)_2Ca$+MgZn	1471.88±55	965±42	501	0.054	33.09
	Al_8Mn_5		1110±36	340	0.005	
ZAXM4211/ SR260	$(Mg, Al)_2Ca$+MgZn	1504±38	997±82	507	0.065	29.90
	Al_8Mn_5		-	-	0.005	
ZAXM4211/ SR300	$(Mg, Al)_2Ca$	1451.88±61	965±42	486.72	0.052	25.62
	Al_8Mn_5		1110±36	341	0.005	
ZAXM4211/ SR340	$(Mg, Al)_2Ca$	1520.30±23	1133±34	487.55	0.0461	18.18
	Al_8Mn_5		-	-	0.005	

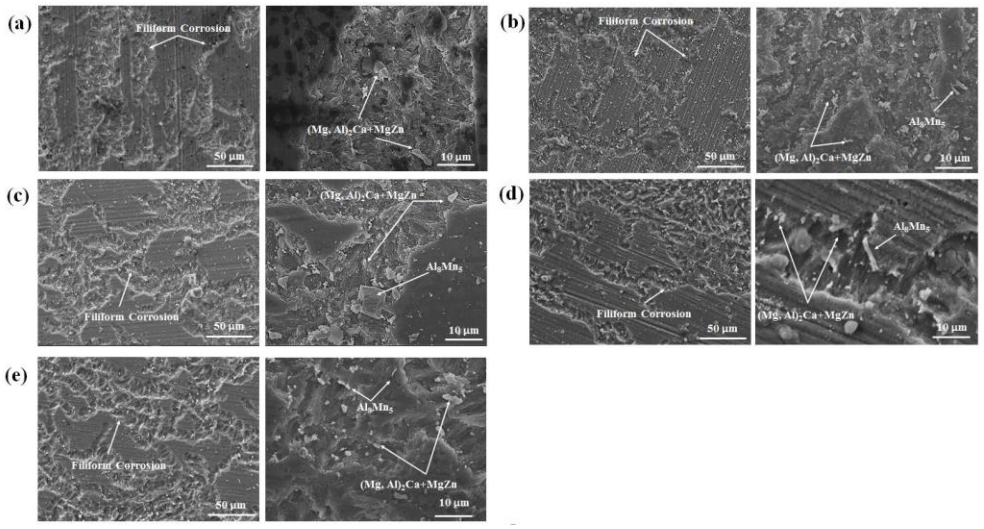

Fig. 36. SEM images of the 3 h immersed samples in 3.5 wt. % NaCl saturated with Mg(OH)2: (a) Extrusion, (b) SR220, (c) SR260, (d) SR300 and (e) SR340.

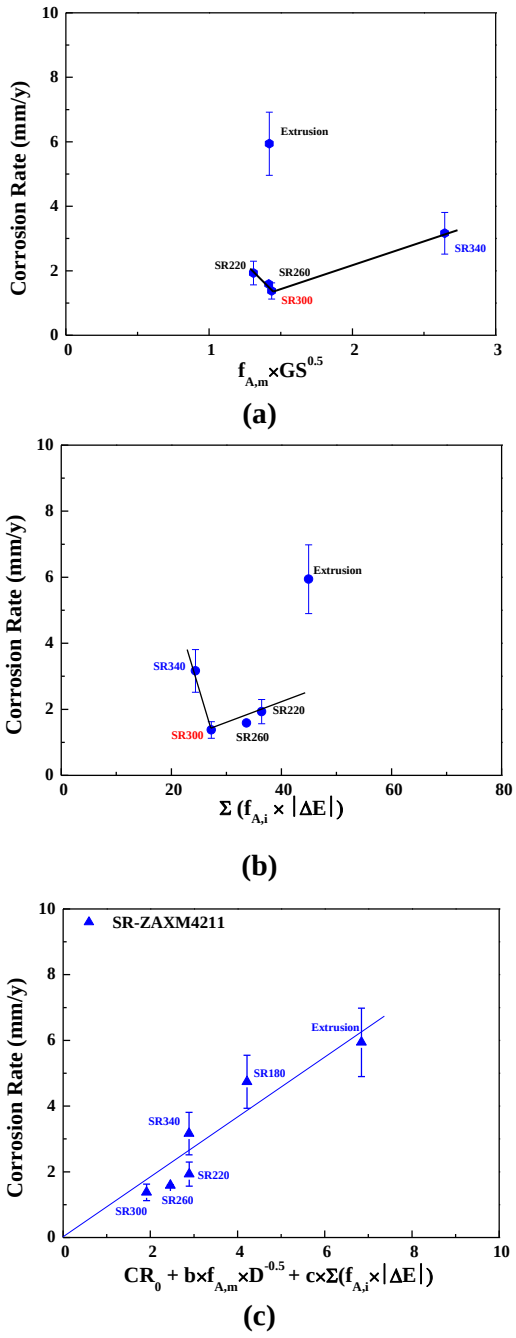

Fig. 37. The relationship between corrosion rate, grain size, volta-potential and phase fraction: (a) corrosion rate versus phase fraction and volta-potential difference, (b) corrosion rate vs. grain size and (c) corrosion rate versus combined parameter.

3.7.4 Summary

The ZAXM4211 alloy produced by extrusion and screw rolling and their mechanical properties and corrosion behavior were studied. The following results were obtained:

1. Microstructures of the samples processed at lower temperatures are finer. Decreasing the temperature of screw rolling increased hardness, UTS and YS, regarding to the grain refinement and dissolution of the secondary phases.

2. Area fraction of intermetallics gradually decreases with increasing the temperature.

3. Increasing the temperature has two controversial effects including dissolution of the secondary phase into the matrix and increasing the grain size. Dissolution of the secondary phases into the matrix results in decreasing galvanic cells and corrosion rate, while increasing the grain size results in increasing the corrosion rate.

4. A model based upon volta-potential difference, phase fraction and grain size was proposed which can model all the SR corrosion results (R^2= 0.96).

Based upon the current study, to produce lowest corrosion rate material, best combination of grain size and fraction of the secondary phase can be found in the SR300.

3.9 Effect of multi-directional forging on mechanical properties and corrosion behavior of ZAXM4411 alloy

Fig. 38 shows a comparison between the corrosion rate and yield strength of materials produced in the present work with the other reported magnesium alloys. Atrens et al. [1, 7, 133, 134] produced several Mg alloys series including high purity magnesium using different processing routes comparing their corrosion rates. Here, the yield strength and corrosion rate of the current materials have been compared with the mentioned alloys including their best corrosion resistant ones. The measuring conditions of yield strength and corrosion rate have been listed in the Table 14.Table 14. The conditions of corrosion and mechanical properties study of current and reviewed literature. As shown in the Fig. 38, a very good combination of corrosion resistance with yield strength has been achieved in the present work using MDF.

3.9.1 Microstructures

In order to identify the formed secondary phases, XRD, thermodynamic calculations using JmatPro commercial software, TEM and SEM/EDS analysis have been used in the present investigation. Fig. 39 shows the XRD patterns of ZAXM4411 alloy consisting of α_{Mg}, Φ ($Mg_{11}Al_5Zn_4$), $(Mg,Al)_2Ca$ and Al_8Mn_5 compounds. Here the samples have been also compared with the annealed sample. In the Fig. 39 (b) the XRD profile in 2θ between 40^o and 50^o has been redrawn while it shows the peaks width which is called FWHM is broader in extruded and MDF180 samples comparing to MDF300 and annealed samples. According to the Scherer's equation, the mean size of the ordered domains which is called a crystallite is inversely related to the FWHM. So it is clear that the average size of intermetallic phases is smaller for extruded and MDF180 samples.

Steady state thermodynamic calculations in Fig. 40 shows the Φ phase is stable in low temperature but it disappears at high temperatures, while $(Mg,Al)_2Ca$ and Al-Mn compounds are stable even at high temperatures.

SEM/EDS results in Fig. 41 show that intermetallic compounds mainly include Al_8Mn_5 and Mg-Zn-Al-Ca phase. However TEM image in the Fig. 42 shows that Mg-Zn-Al-Ca phase contains two different phases including Φ ($Mg_{11}Al_5Zn_4$), and

$(Mg,Al)_2Ca$. Since $(Mg,Al)_2Ca$ phase is stable in higher temperature, it forms during solidification and cooling and later on Φ phase forms on that at the eutectic temperature. So these two phases appear together in the SEM images.

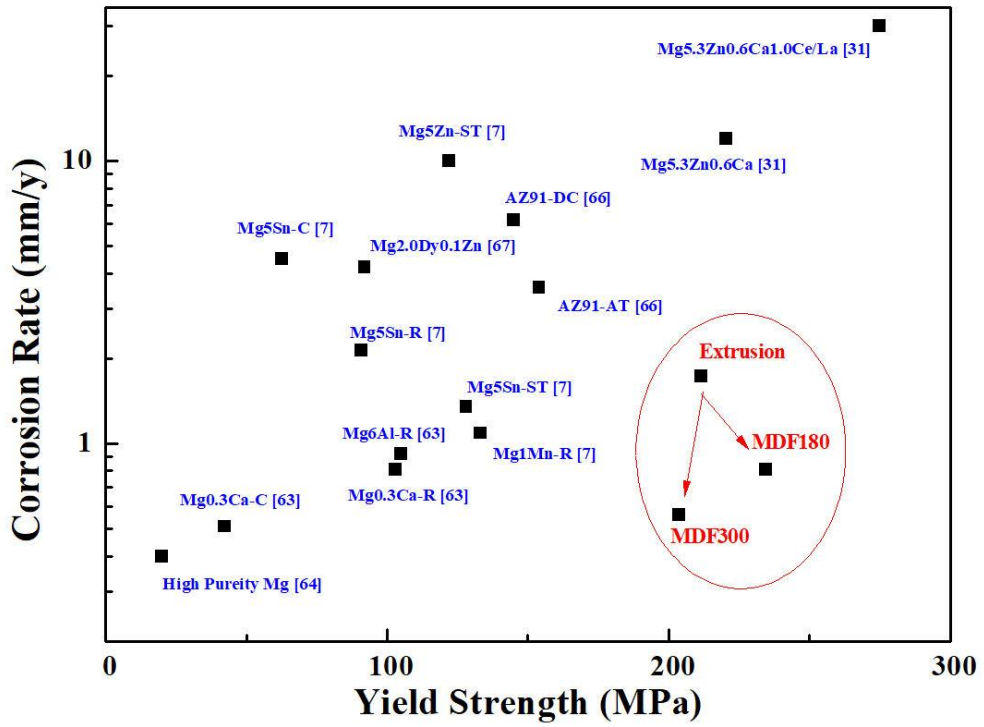

Fig. 38. The comparison of yield strength and corrosion rates of the current samples with the available Mg alloys. The corrosion rate of the current study has been obtained through the hydrogen evolution method.

Table 14. The conditions of corrosion and mechanical properties study of current and reviewed literature.

Reference	Processing method	Solution	Corrosion rate measurement	Strain rate
Current study	Extrusion and MDF	3.5 wt.% NaCl with saturated ($Mg(OH)_2$)	Hydrogen evolution	2×10^{-4} s^{-1}
[1, 7, 133, 134]	C: Casting R: Wrought H: Solution heat treatment	3.5 wt.% NaCl with saturated ($Mg(OH)_2$)	Hydrogen evolution	Stress rate: 7.0×10^{-5} MPa s^{-1}
[135]	Extrusion	3.5 wt% NaCl	Weight loss	1.67×10^{-3} s^{-1}
[66]	DC: Die Cast AT: Age Treatment	3.5 wt% NaCl	Weight loss	N/A
[136]	High pressure die cast	3.5 wt% NaCl	Weight loss	10^{-3} s^{-1}

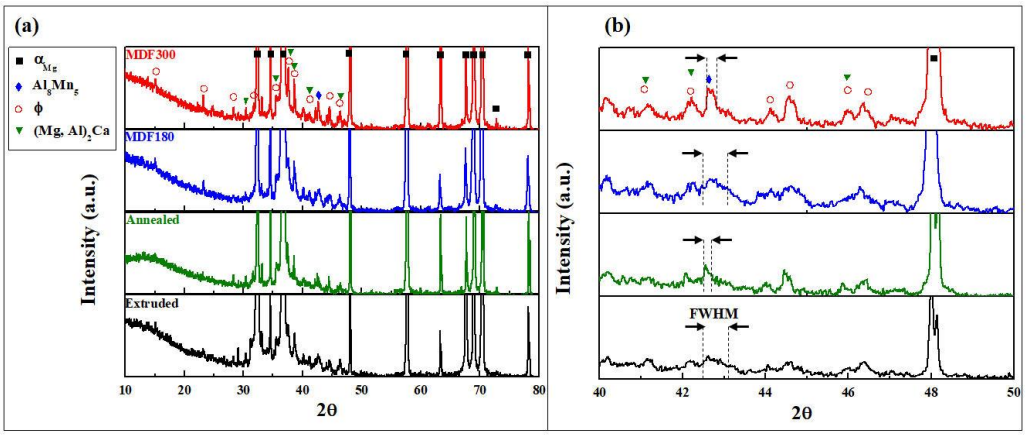

Fig. 39. XRD patterns of ZAXM4411 alloy: (a) 10-80^o and (b) 40^o-50^o.

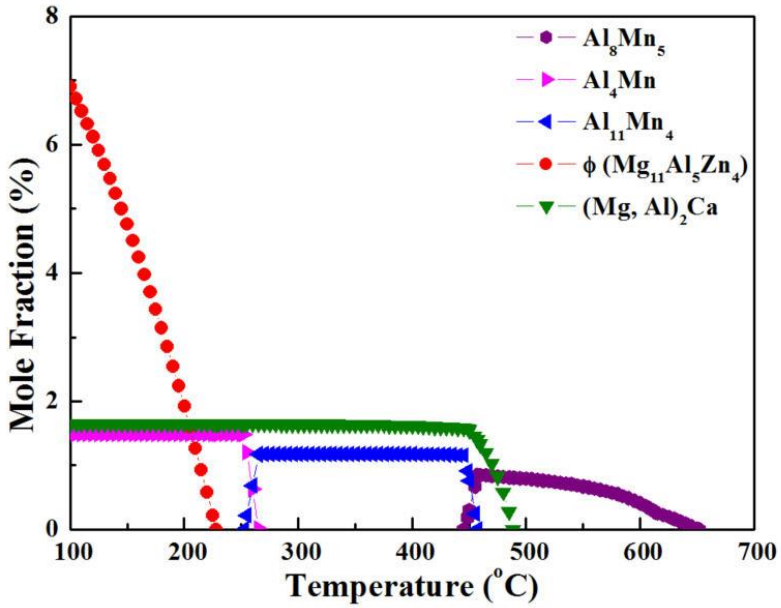

Fig. 40. Phase fraction prediction using thermodynamic calculation.

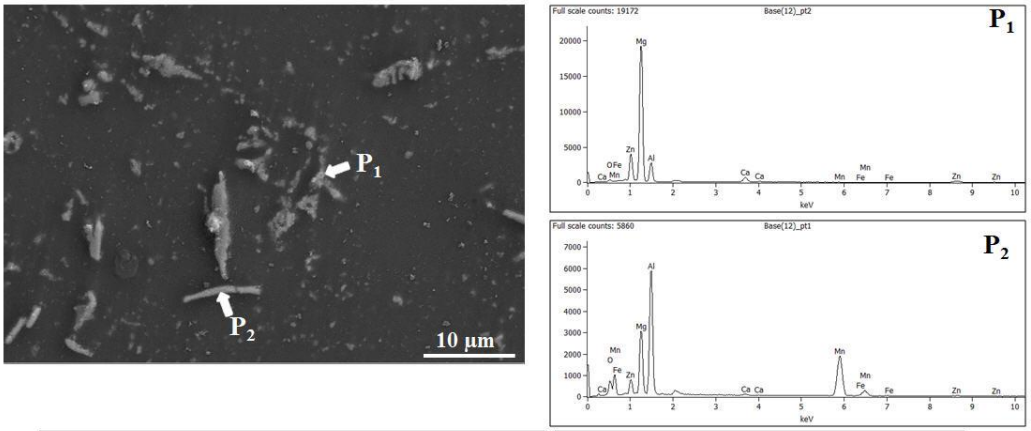

Points		Mg-K	Al-K	Ca-K	Mn-K	Zn-K
P_1:Φ + $(Mg, Al)_2Ca$	wt%	33.55	20.58	6.05	0.10	34.01
	at%	43.51	24.04	4.76	0.06	16.40
P_2: (Al_8Mn_5)	wt%	8.75	38.61	0.07	49.98	1.11
	at%	12.80	50.88	0.06	32.35	0.61

Fig. 41. SEM/EDS analysis of the intermetallic compounds.

The phase distribution on the surface A and B (Fig. 5) have been shown in Fig. 43. Large and fine precipitates are observed in all the samples. However, fine precipitates are more observable for MDF180 and less for MDF300. Moreover, Φ+$(Mg,Al)_2Ca$ transformed from solid particles (See Extruded and MDF180) into the globular shape for MDF300. Quantitative analysis showed that the area fraction of the Φ+$(Mg, Al)_2Ca$ phase in extruded, MDF180 and MDF300 samples are 6.4, 6.1 and 3.7% respectively and the area fraction of the Al_8Mn_5 are 1.4, 1.5 and 1.0 %, respectively.

Phase distribution in the surface parallel to the extrusion direction and 7^{th} pass of MDF (Surface B in Fig. 5) showing the phases have been arranged alongside the extrusion direction and even after MDF, the extrusion direction is distinguishable for both MDF180 and MDF300. However, regarding to the perpendicular forces applied on the other surfaces, the phase morphology has been changed. Φ+$(Mg,Al)_2Ca$ phases are soft and can be folded or bended via the deformation especially at 300 ^oC while Al_8Mn_5 is a hard phase which is broken into smaller pieces instead of folding. So it can be mentioned that low temperature MDF resulted mainly on the fragmentation of the intermetallics to several fine particles. However, the Φ+$(Mg,Al)_2Ca$ have been dissolved in the grain boundaries and matrix through the dynamic recrystallization and grain growth, because Zn and Al can be dissolved more into the α_{Mg}. That is why fine precipitates are less observable in the matrix.

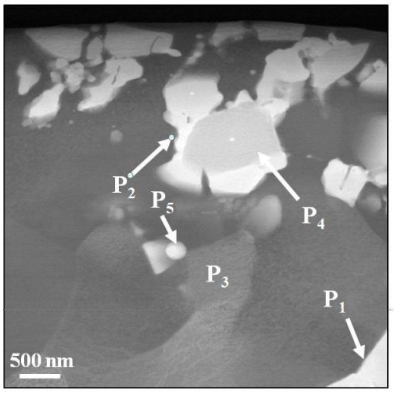

Points		Mg-K	Al-K	Ca-K	Mn-K	Zn-K
P_1:Φ	wt. %	20.29	24.89	7.24	-	47.56
	at. %	31.32	34.60	6.77	-	27.29
P2: Φ	wt. %	20.99	24.43	8.31	-	45.25
	at. %	31.92	34.83	7.66	-	25.57
P_3: α_{Mg}	wt. %	97.64	1.48	-	-	0.87
	at. %	98.32	1.34	-	-	0.32
P_4: $(Mg, Al)_2Ca$	wt. %	1.89	42.81	18.39	-	36.90
	at. %	2.89	59.03	17.07	-	20.99
P_5: Al_8Mn_5	wt. %	17.64	47.79	1.03	28.87	3.98
	at. %	23.25	56.74	0.82	16.83	1.95

Fig. 42. Dark field TEM/EDS in the extruded ZAXM4411 alloy.

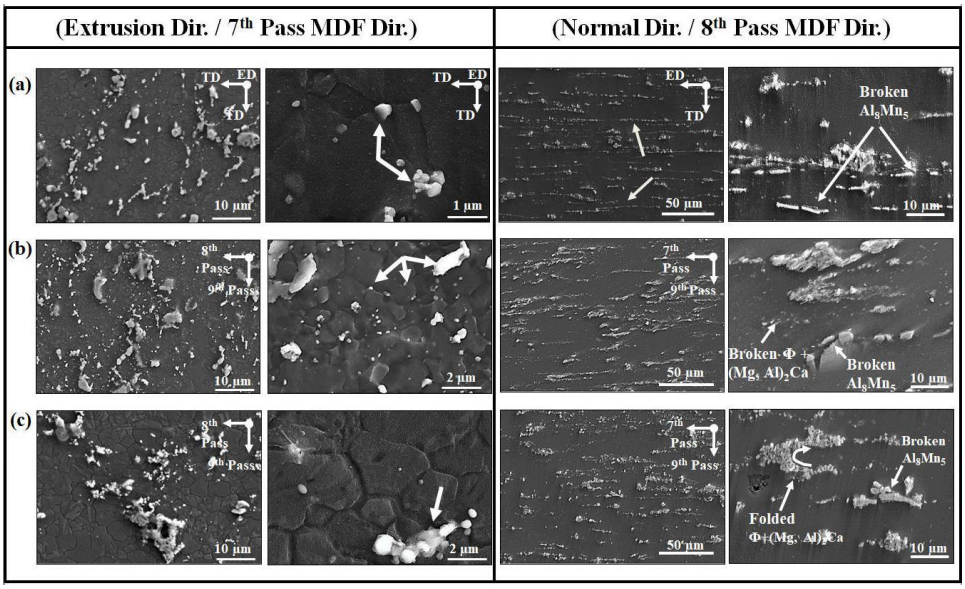

Fig. 43. SEM images of samples showing the secondary phases distribution perpendicular and parallel to the extrusion direction: (a) Extruded, (b) MDF180 and (c) MDF300.

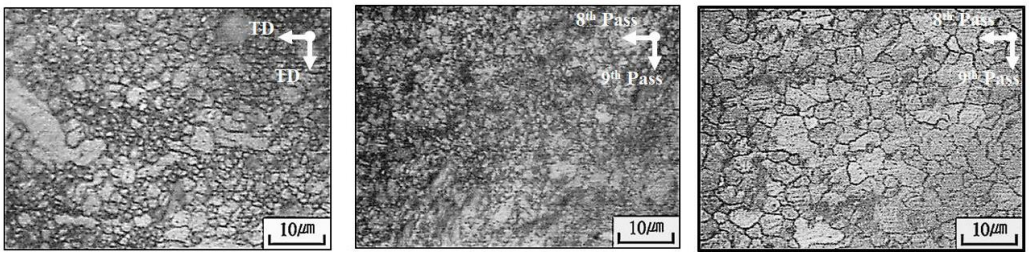

(a) (b) (c)

Fig. 44. The microstructure of ZAXM4411 alloy: (a) Extrusion (b) MDF180 and (c) DF300.

Grains distribution of the samples has been presented in Fig. 44. Extruded sample includes some fine grains which are dynamic recrystallized (DRX) grains and some large grains which are worked grains deformed alongside the extrusion direction. The grains distribution has been uniformed after MDF. In addition, grains have been refined effectively at 180 ^{o}C and grown at 300 ^{o}C due to dynamic recrystallization and growth. The worked grains formed during extrusion can be found in MDF180, but with smaller size comparing to the extruded sample. However, they have been almost removed from MDF300. The intermetallic compounds, as shown in the Fig. 43, hinder grains to be enlarged and make the grains uniform through the MDF process. However, during MDF at 300 ^{o}C, precipitates dissolves in the grain boundaries and lattice defects by decreasing the lattice energy, so less precipitate and larger grains observed in MDF300.

3.9.2 Mechanical properties

The tensile and compression curves are illustrated in Fig. 9 and the related properties are listed in Table 15. Tensile yield strength values has been increased by grain size reduction after MDF at 180 ^{o}C and slightly decreased after MDF at 300 ^{o}C. Grain boundaries and intermetallic compounds impede dislocations propagation and since MDF180 having the most grain boundaries and finest intermetallic compounds, showed the highest tensile yield strength. However, tensile to

compression proportion being called yield anisotropy has been approached to 1.0 for the MDF300. The value of 1.0 stands for completely isotropic yield strength. Since the texture has been randomized through MDF, the yield isotropy has been improved. Moreover, regarding to more randomization of texture at elevated temperature, MDF300, the yield anisotropy factor approached more to 1.0. The extruded sample has the lowest anisotropy regarding to directional deformation. The strain hardening exponent in MDF300 is higher than that of extruded sample while the related value of extruded sample is also higher than that of MDF180 which can be explained through the grain size while large grain size can be broken in to smaller grains by formation of twins during tension in larger grain boundaries.

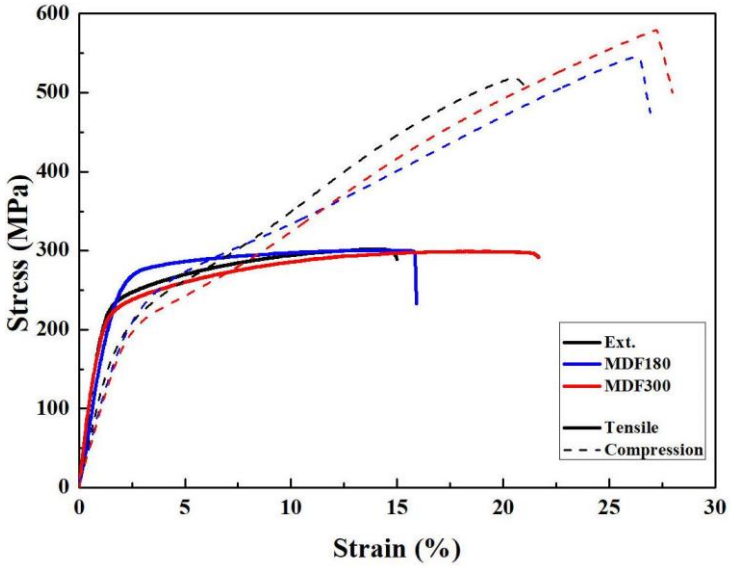

Fig. 45. Tensile and compression tests of MDF samples.

Table 15. Mechanical properties of studied alloy.

			Tensile Properties			Compression Properties		
Sample	Grain Size (μm)	Yield Anisotropy (TYS/CYS)	TYS	UTS	El	CYS	UCS	El
Extruded	2.11	0.77	211.52	302.16	14.99	162.86	517.87	21.00
MDF180	1.10	0.83	234.45	300.82	15.93	195.60	544.29	26.50
MDF300	3.07	0.88	203.53	299.08	21.68	179.11	579.03	27.26

3.9.3 Corrosion behavior

The overall Mg corrosion reaction is [4]:

$$Mg + 2H_2O \rightarrow Mg^{2+} + 2(OH)^- + H_2 \rightarrow Mg(OH)_2 + H_2 \quad (4)$$

Here the metallic Mg converted to its ion, Mg^{2+}, which is stable in aqueous solutions. One molecule of hydrogen, H_2, is liberated for every atom of Mg that corrodes. Thus, the measurement of the evolved hydrogen allows a direct measurement of Mg corrosion. The cathodic partial reaction is hydrogen evolution, which for a neutral or alkaline solution can be written as follows:

$$2H_2O + 2e^- \rightarrow H_2 + 2(OH)^- \quad (5)$$

The cathodic reaction produces OH^-, and local alkalization, leading to a tendency for local passivation. The overall anodic reaction is:

$$Mg \rightarrow Mg^{2+} + 2e^- \quad (6)$$

In principle, the corrosion rate can be evaluated by measuring the quantity of Mg ions, Mg^{2+}, in solution. Eq. 6 indicates that for each atom of Mg that is corroded, there is one produced Mg^{2+} ion. In practice however, a significant fraction of the Mg^{2+} produced are precipitated as $Mg(OH)_2$ because of the low solubility of $Mg(OH)_2$ [79].

Fig. 46 shows the hydrogen evolution and corresponding corrosion rate of extruded and MDF alloys for seven days. The evolved hydrogen and hence corrosion rate of MDF samples are obviously less than that of extruded alloy and among two MDF alloys, the samples produced at higher temperature show lower hydrogen evolution and corrosion rate.

The corrosion rate of the alloys using hydrogen evolution and weight loss methods have been listed in Table 16 showing same trend of corrosion rate.

Photographic images of the immersed samples after removing corrosion products and also SEM images of corroded surfaces before removing corrosion products have been shown in Fig. 47. It can be seen that the extruded and MDF180 samples have corroded more and pitting sites can be found on these two samples. SEM

Images show that the corrosion products at the surface of MDF300 sample is less voluminous. Here, some areas without any corrosion products can be observed.

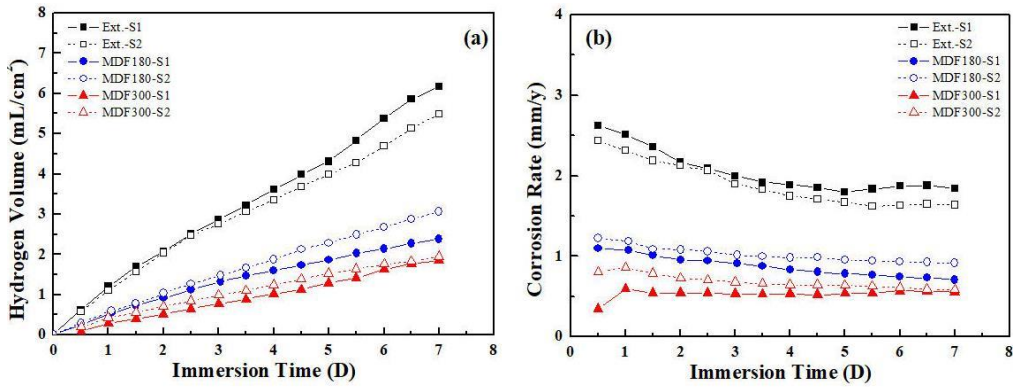

Fig. 46. Corrosion rate values for different alloys using hydrogen evolution method; (a) volume of hydrogen evolved and (b) corrosion rate during immersion in 3.5 wt.% NaCl with saturated $Mg(OH)_2$.

Table 16. Hydrogen evolution volume and weight loss study data for extruded and MDF samples (P_H and P_W are the corrosion rates measured by hydrogen evolution and weight loss methods, respectively).

Sample	Evolved Hydrogen (ml/cm^2)	Corrosion Rate P_H (mm/y)	Weight Loss (mg/cm^2)	Corrosion Rate P_W (mm/y)
Ext.	**6.18**	**1.84**	**1.60**	**3.36**
	5.48	**1.64**	**1.48**	**3.10**
MDF180	**2.36**	**0.71**	**1.22**	**2.55**
	3.06	**0.91**	**1.38**	**2.85**
MDF300	**1.85**	**0.55**	**0.92**	**1.94**
	1.95	**0.58**	**0.97**	**2.03**

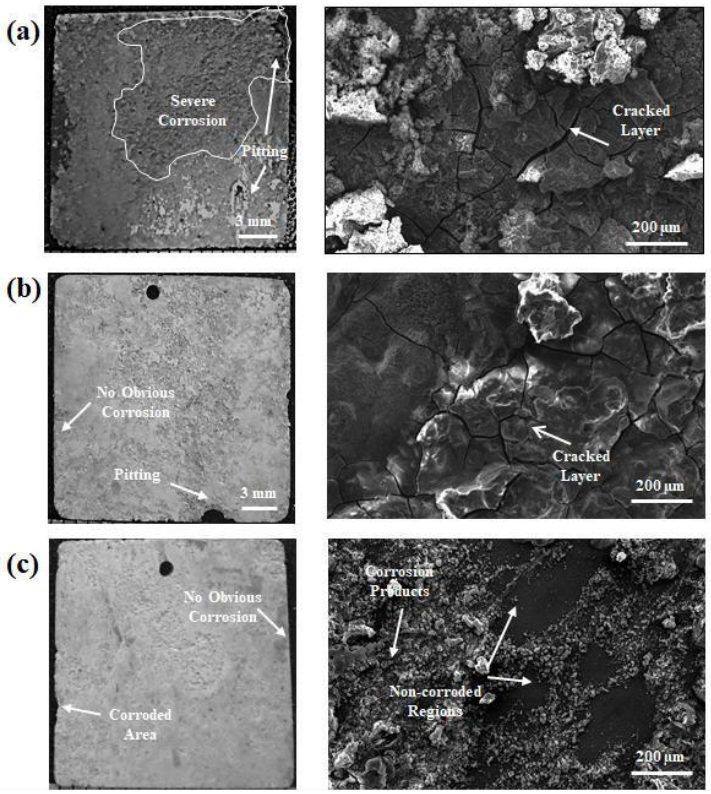

Fig. 47. Photographic and SEM images of corroded surfaces; (a) Extruded, (b) MDF180 and (c) MDF300.

The Nyquist plots are shown in Fig. 48 (a). The capacitive loop at the high frequency region indicates the charge transfer reaction at surface, and the dimension of capacitance loop determines the charge transfer resistance [71]. The diameter of high frequency capacitance loop of MDF samples is larger than that of the extruded, indicating that the charge transfer resistance has remarkably increased after MDF and in particular after high temperature MDF. The Bode plot (Fig. 48 (b)) shows a drop for all three samples in low frequencies which is related to passive layers being locally destroyed. Data scattering can be observed for all samples in both Nyquist and Bode plots relating to the nature of this material against passive layer destruction at low frequencies.

Potentiodynamic polarization studies were carried out and the Tafel plots are shown in Fig. 48 (c). The related values including corrosion current density (i_{corr}), corrosion potential (E_{corr}), and corrosion rate (P_i) have been listed in the table. i_{corr} values were obtained extrapolating the cathodic region. As it was mentioned through the Equation 1, i_{corr} shows alloy corrosion rate related to degradation of Mg. The i_{corr} values obtained from Tafel show that MDF significantly improved the corrosion resistance of this alloy as proved through hydrogen evolution and weight loss studies (

Table 16). It can be seen that the extruded and MDF180 samples suffered more from pitting resulting higher corrosion current density and corrosion rate. The pitting retardation is related to the reduction of the secondary phases and uniformity of microstructure. So the surface passive layer was more stable for the MDF300 than that of MDF180 and extruded samples.

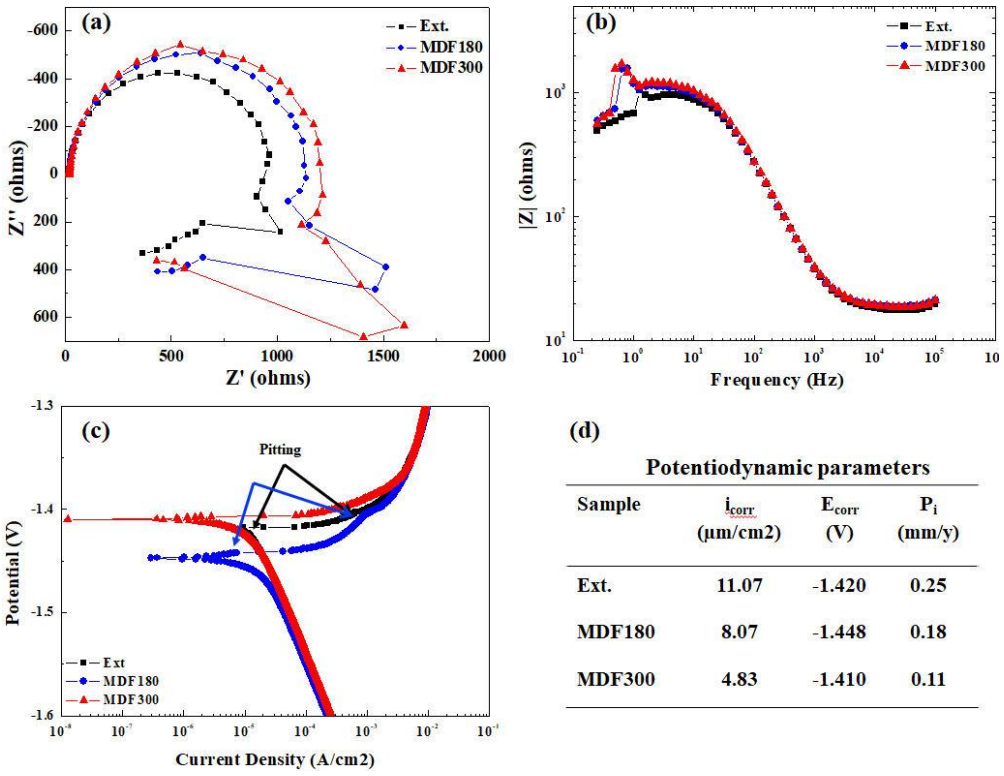

(d)

Potentiodynamic parameters

Sample	i_{corr} (µm/cm2)	E_{corr} (V)	P_i (mm/y)
Ext.	11.07	-1.420	0.25
MDF180	8.07	-1.448	0.18
MDF300	4.83	-1.410	0.11

Fig. 48. EIS and polarization curves of samples after 30 min immersion in 3.5 wt.% NaCl saturated with Mg(OH); (a) Nyquist plot, (b) bode plot, (c) potentiodynamic polarization curves and (d) polarization parameters.

3.9.4 SKPFM

In order to identify surface potential differences of secondary phases and matrix, scanning kelvin probe force microscopy (SKPFM) technique was used. Secondary p

hases are generally detrimental to corrosion of the matrix, therefore the potential +difference between the secondary phases and matrix, their fraction, and distribution play a key role in determining Mg corrosion. Fig. 49 shows the SKPFM surface of the matrix and intermetallics and the Volta-potential are given in the Table 17. All intermetallics are cathodic relative to the matrix while each phase has different Volta-potential difference. No specific Volta-potential difference was observed in different samples. The average Volta-potential difference of Φ+$(Mg,Al)_2Ca$ relative to the matrix is 195 mV. The average Volta-potential difference of Al_8Mn_5 (Fig. 49 (d)) with matrix is 230 which is higher than that of Φ+$(Mg,Al)_2Ca$. Since all intermetallic are cathodic relative to the matrix, they act as initiation sites of corrosion and the adjacent matrix is corroded during immersion.

3.9.5 Short time immersion

Short time immersion was studied to observe the corrosion propagation at initial stages. In this regard samples were immersed for 0.5 and 3 h in 3.5 wt.% NaCl with saturated $Mg(OH)_2$. The photographic images after 3 h immersion showed in Fig. 50 (a). The exposed surface has been completely corroded while the corroded area was reduced for MDF180 and MDF300 samples, respectively.

Since the second phases are cathodic against the matrix, as proved by the SKPFM analysis, it can be expected that distribution of these phases can change the corrosion behavior. Fig. 50 (b) depicts the cross section of the 3 h immersed samples showing the matrix has been dissolved adjacent to the second phases. Furthermore, not only the intermetallic phases play the role in the corrosion behavior, but also the matrix also has an important role in corrosion behavior. Fig. 50 (c) shows the cross section of 3 h immersed samples after etching with picric

acid. Large grains, so called worked grains deformed alongside the extrusion direction, have been corroded more comparing to the fine DRX grains. The quantitative analysis of the extruded sample shows that 81% of observed worked grains have been corroded more than the adjacent DRX grains. The worked grains with the average width of 10.85±6.77 μm in the extruded sample has the average corroded depth of 8.30±2.79 μm, while the average corroded depth of DRX grains were 5.82±2.21 μm. Multi directional deformation, dynamic recrystallization and then growth, especially at higher temperatures resulted in more uniform structure and the fraction of long worked grains has been significantly reduced. In the case of MDF180, 83% of observed worked grains have been corroded more than the adjacent DRX grains. The worked grains remained from extrusion process had the average width of 3.84±0.81 μm with the average corrosion depth of 6.69±3.85 μm, while the average corroded depth in DRX zone was 5.82±2.21 μm. Worked grains were not identified in the cross section of MDF300 and the average corroded depth of MDF300 in DRX zone were 3.70±1.87 μm.

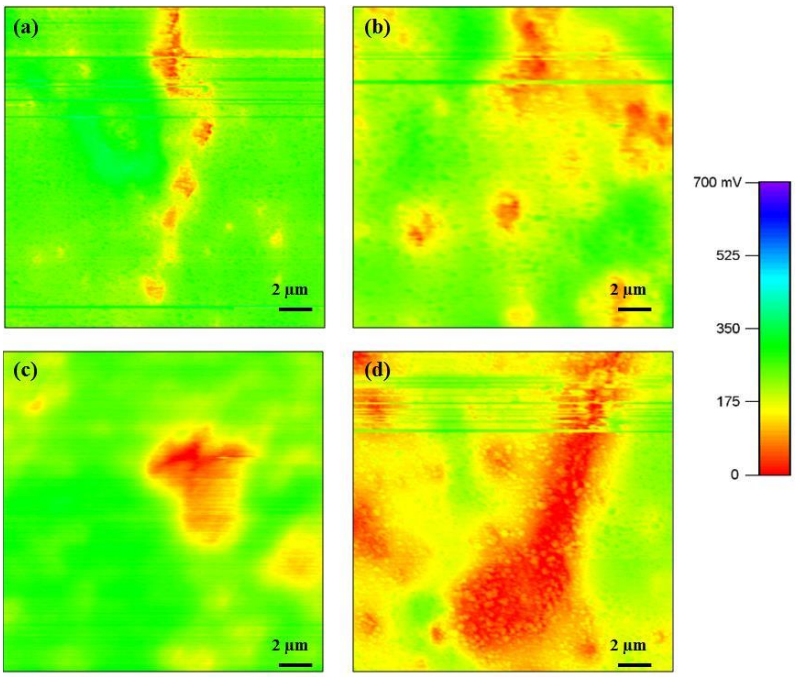

Fig. 49. SKPFM images of Φ+$(Mg,Al)_2Ca$ phase in (a) Extruded (b) MDF180 and (c) MDF300, and (d) Al_8Mn_5 compound in MDF180.

Table 17. Volta Potential difference of second phase precipitates.

	Extruded	MDF180	MDF300
Φ+$(Mg,Al)_2Ca$	181.8±39	205±52	198±28
Al_8Mn_5	-	230±29	-

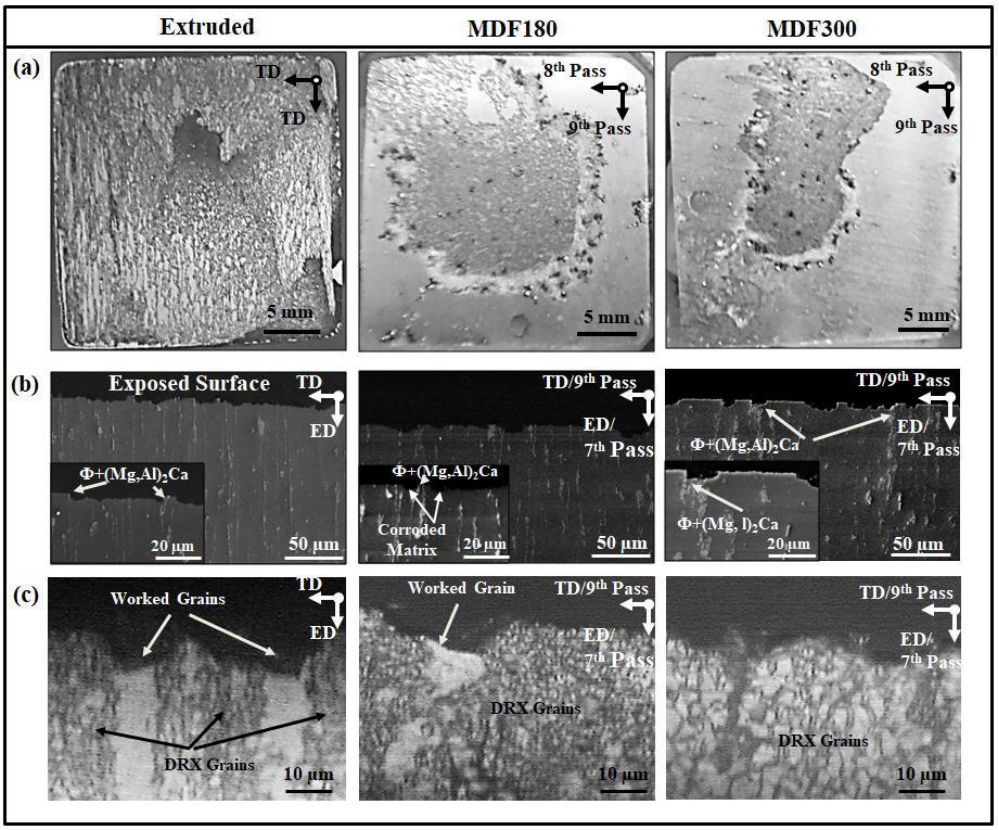

Fig. 50. Corroded surfaces after 3 h immersion; (a) photographic images of the exposed surfaces, (b) SEM images from cross section view and (c) optical micrographs of cross section after etching.

Fig. 51 depicts the SEM images of 0.5 h immersed samples after removing corrosion products. Corrosion initiated by a pitting adjacent to the intermetallic compounds (Fig. 51 (a) and (b)) and then propagated as filiform corrosion on the matrix. An island shape matrix surrounded by the intermetallic compounds in the Fig. 51 (c) shows the corrosive solution ingress around the cathodic intermetallic phases. Fig. 51 (e-h) and Fig. 51 (i-l) show the SEM images of MDF180 and MDF300, respectively. Nano-grains are obviously distinguishable in the MDF180 (Fig. 51 (g) and (h)) especially when they are compared with the size of grains in the extruded (Fig. 51 (d)) and MDF300 (Fig. 51 (k)) where the corrosive solution has attacked to grain boundaries of DRX grains and grains have been corroded preferentially.

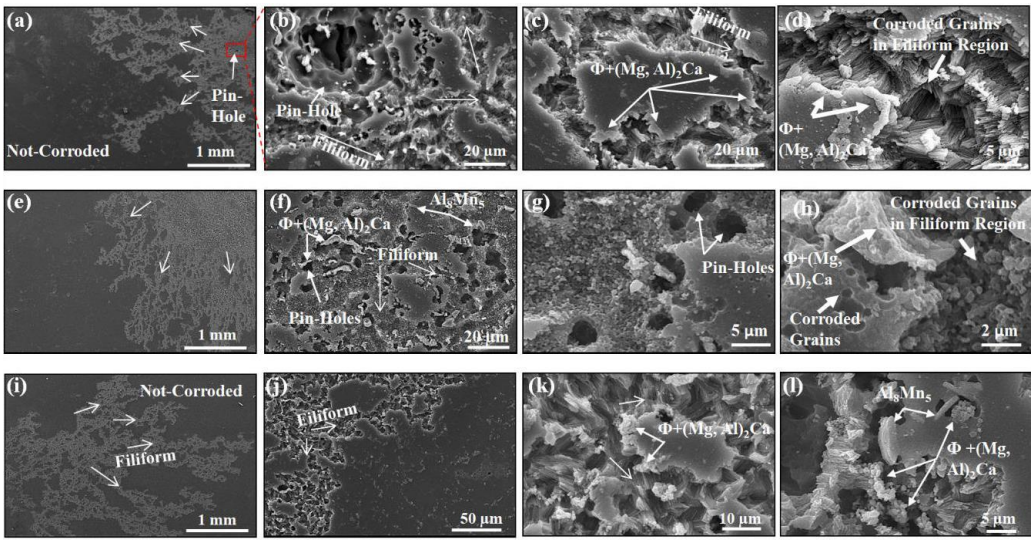

Fig. 51. SEM images of 0.5 h immersed ZAXM4411 alloy with different magnifications; (a-d) Extruded: (a) Lowest magnification showing the pit and filiform corrosion, (b) higher magnification image with the pit and filiform corrosion, (c) island-shape matrix surrounded by cathodic phases (d) filiform corrosion through the grains and between the secondary cathodic phases. (e-h) MDF180: (e) lowest magnification showing pits and filiform corrosion, (f) higher magnification image with several pits formed adjacent to the cathodic intermetallics and filiform corrosion, (g) high magnification image showing the nano-grains and (h) filiform corrosion through the grains and between the secondary cathodic phases. (i-l) MDF300: (i) lowest magnification showing the corroded site with pits and filiform corrosion, (j) higher magnification image showing the filiform corrosion on the matrix (k) filiform corrosion through the grains and between the secondary cathodic phases; and (l), globular Φ+(Mg, Al)$_2$Ca phase and Al_8Mn_5 phases caused the anodic matrix to be dissolved.

3.10 Effect of multi directional forging on mechanical properties and corrosion behavior of ZAXM4211 alloy

3.10.1 Microstructures

Steady state thermodynamic calculations in Fig. 52 shows ZAXM4211 alloy contains $(Mg,Al)_2Ca$, MgZn and Al-Mn compounds. MgZn phase is not stable at high temperature and it disappears at temperature higher that 180 ^oC while $(Mg,Al)_2Ca$ and Al-Mn compounds are stable at high temperatures and their fraction is almost same in MDFed temperature.

Grains distribution of the samples has been presented in Fig. 53. Extruded sample includes some fine grains which are dynamic recrystallized (DRX) grains and some large grains which are worked grains deformed alongside the extrusion direction. The grains distribution has been uniformed after MDF. In addition, grains size has been enlarged from 180 ^oC to 300 ^oC samples. The worked grains formed during extrusion can be found in MDF180, but with smaller size comparing to the extruded sample, showing nonhomogeneous microstructure in the extruded and MDF180 samples. However, large grains formed during extrusion alongside the extrusion direction have been almost removed for high temperature MDF, so the microstructure is more uniform.

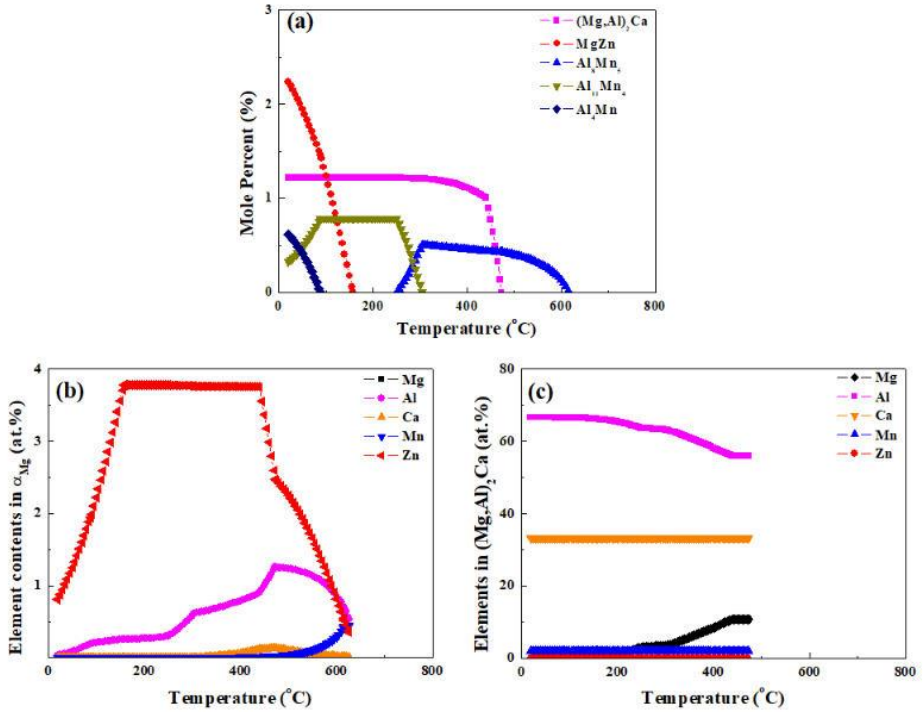

Fig. 52. Phase fraction prediction using thermodynamic calculation.

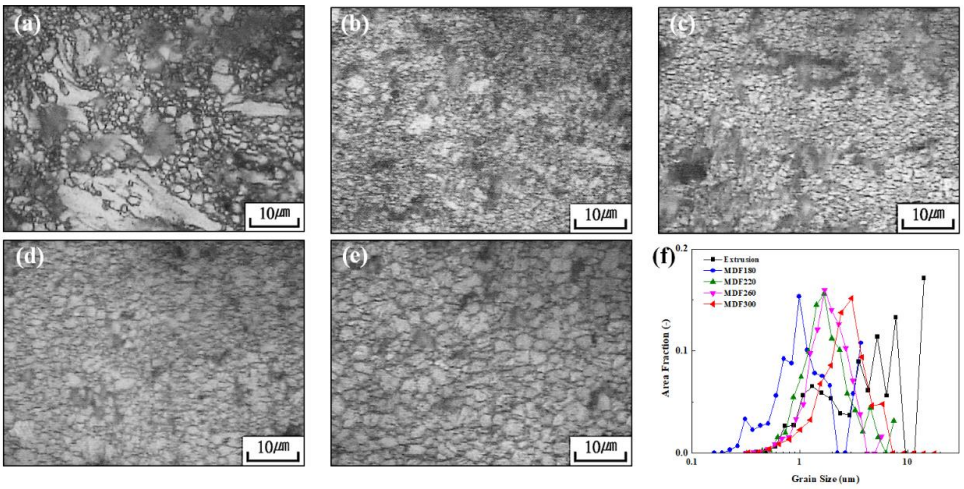

Fig. 53. The microstructure of samples: (a) Extruded, (b) MDF180, (c) MDF220, (d) MDF260, (e) MDF300, and (f) grain size fraction distribution.

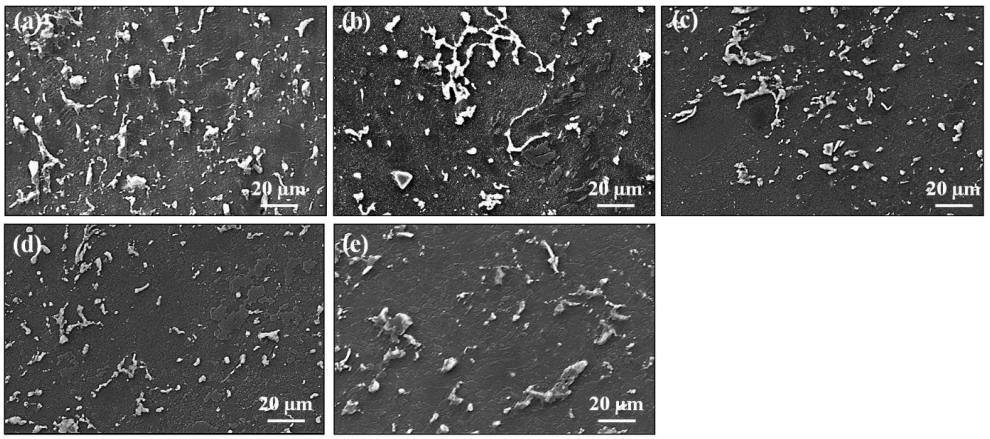

Fig. 54. Second phase distribution of the ZAXM4211 alloy: (a) Extruded, (b) MDF180, (c) MDF220, (d) MDF260, (e) MDF300, and (f) grain size fraction distribution.

3.10.2 Mechanical properties

The mechanical properties, including compression and tension yield strength, ultimate strength and elongation of the alloy can be controlled by choosing the temperature of MDF. The tensile and compression curves are illustrated in Fig. 55 and the related properties are listed in

Table 18. Tensile and compression yield strength values have been increased significantly by grain size reduction after MDF at all temperatures. Grain boundaries and intermetallic compounds impede dislocations propagation and since large worked grains have been removed after MDF, yield strength has been improved, however, MDF180 having the most grain boundaries and finest intermetallic compounds, showed the highest tensile yield strength. But the yield strength has been gradually decreased by increasing the MDF temperature due to reduction of grain boundaries.

The tensile to compression proportion being called yield anisotropy has been approached to 1.0 for the MDF260 and MDF300. The value of 1.0 stands for completely isotropic yield strength. Since the texture has been randomized through MDF, the yield isotropy has been improved. Moreover, regarding to more randomization of texture at elevated temperature, MDF260 and MDF300, the yield anisotropy factor approached more to 1.0. The extruded sample has the lowest anisotropy regarding to directional deformation.

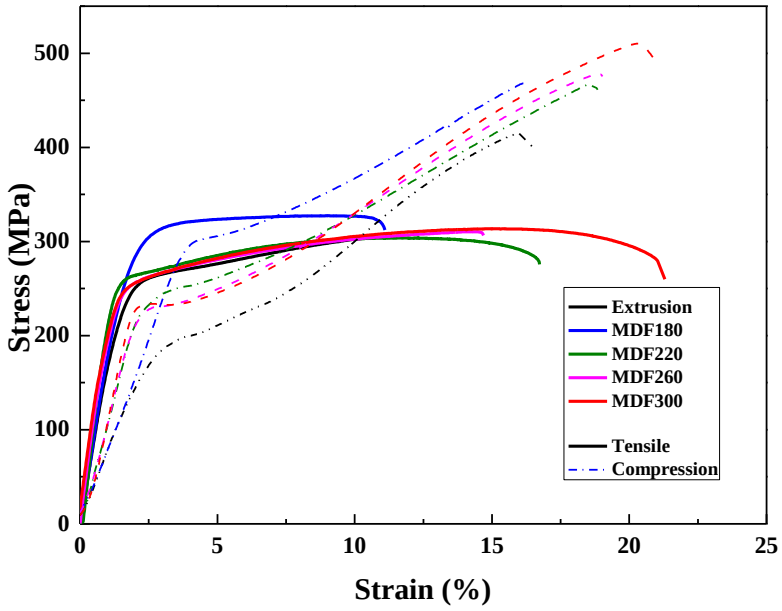

Fig. 55. Tensile and compression tests of MDF samples.

Table 18. Mechanical properties of studied alloy.

	Tensile Test			Compression Test		
Sample	**TYS (MPa)**	**UTS (MPa)**	**El. (%)**	**CYS (MPa)**	**UCS (MPa)**	**El. (%)**
Extruded	205.43	303.85	10.72	170.24	415.36	16.50
MDF180	269.36	327.41	11.14	295.63	468.20	16.29
MDF220	256.42	303.86	16.73	230.86	466.91	18.85
MDF260	221.23	310.48	14.69	218.39	477.86	19.03
MDF300	218.19	313.59	21.30	220.21	510.24	21.05

3.10.3 Corrosion behavior

The overall Mg corrosion reaction is [79]:

$$Mg + 2H_2O \rightarrow Mg^{2+} + 2(OH)^- + H_2 \rightarrow Mg(OH)_2 + H_2 \quad (4)$$

Here the metallic Mg converted to its ion, Mg^{2+}, which is stable in aqueous solutions. One molecule of hydrogen, H_2, is liberated for every atom of Mg that corrodes. Thus, the measurement of the evolved hydrogen allows a direct measurement of Mg corrosion.

Fig. 56 shows the hydrogen evolution and corresponding corrosion rate of extruded and MDF alloys for seven days. The evolved hydrogen and hence corrosion rate of MDF samples are obviously less than that of extruded alloy and among MDF alloys, the samples produced at higher temperature show lower hydrogen evolution and corrosion rate.
The corrosion rate of the alloys using hydrogen evolution and weight loss methods have been listed in Table 19 showing same trend of corrosion rate.

Photographic and SEM images of the immersed samples before removing corrosion products have been shown in Fig. 57. It can be seen that the extruded and MDF180 samples have been corroded more while severe corrosion can be observed on their surface while the corrosion products on the surface of MDF260 and MDF300 is less voluminous.

Potentiodynamic polarization studies were carried out and the Tafel plots are shown in Fig. 58. The related values including corrosion current density (i_{corr}), corrosion potential (E_{corr}), and corrosion rate (P_i) have been listed in the Table 20. As it was mentioned through the Equation 1, i_{corr} corresponds to the corrosion rate which is related to degradation of Mg. The i_{corr} values obtained from Tafel show that MDF significantly improved the corrosion resistance of this alloy as proved through hydrogen evolution and weight loss studies (Table 19).

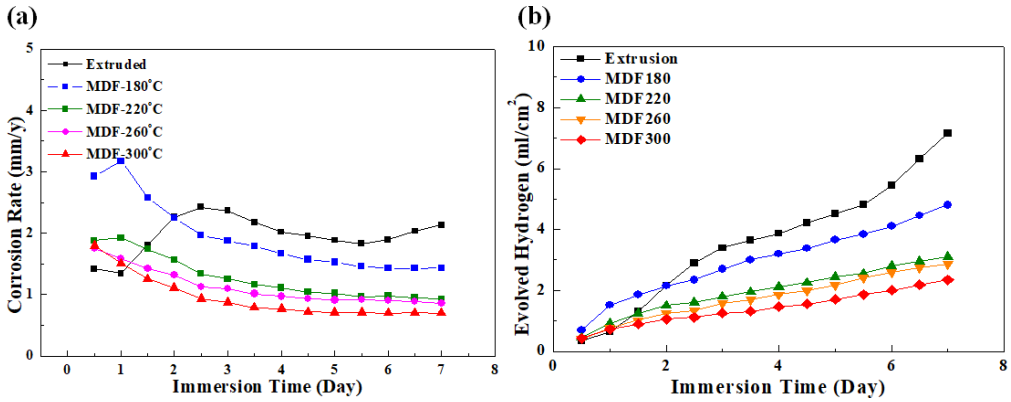

Fig. 56. Corrosion rate values for different alloys using hydrogen evolution method; (a) volume of hydrogen evolved and (b) corrosion rate during immersion in 3.5 wt.% NaCl with saturated $Mg(OH)_2$.

Table 19. Hydrogen evolution volume and weight loss study data for extruded and MDF samples (P_H and P_W are the corrosion rates measured by hydrogen evolution and weight loss methods, respectively).

Alloy	Evolved Hydrogen (ml/cm^2)	Corrosion Rate: P_H (mm/y)	Weight Loss ($mg/cm^2/d$)	Corrosion Rate P_W (mm/y)
Extrusion	7.15	2.13	1.23	2.56
MDF180	4.41	1.32	0.74	1.56
MDF220	2.80	0.84	0.67	1.40
MDF260	2.75	0.82	0.61	1.23
MDF300	2.41	0.72	0.57	1.13

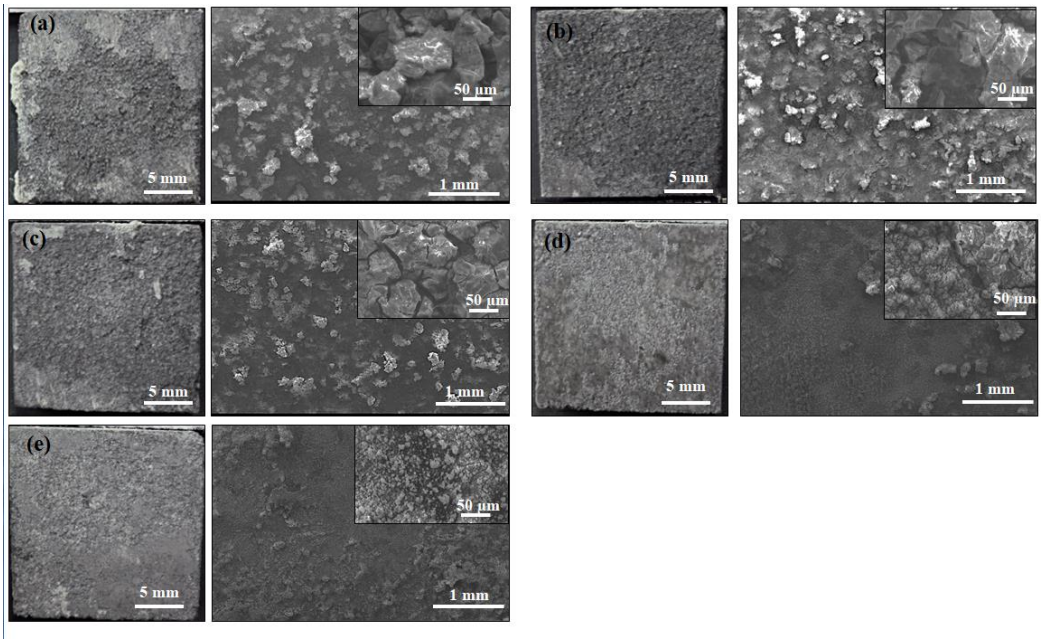

Fig. 57. Photographic and SEM images of corroded surfaces: (a) Extruded, (b) MDF180, (c) MDF220, (c) MDF260 and (e) MDF300.

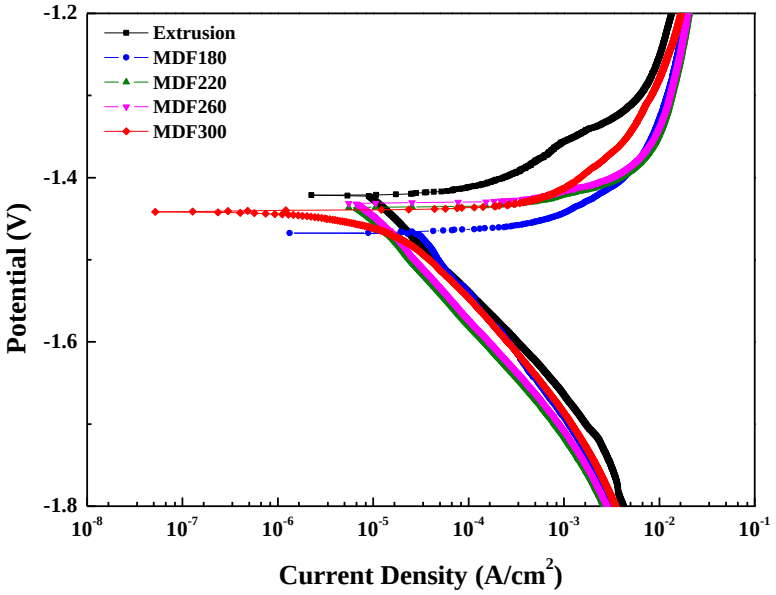

Fig. 58. Potentiodynamic polarization curves of ZAXM4211 alloy in the 3.5 wt.% NaCl saturated with $Mg(OH)_2$.

Table 20. The potentiodynamic values of extruded and MDF alloy in the 3.5 wt.% NaCl saturated with $Mg(OH)_2$.

Sample	i_{corr} (μm/cm^2)	E_{corr} (V)	Corrosion Rate (mm/y)
Extrusion	25.33	-1.43	0.58
MDF180	30.91	-1.47	0.71
MDF220	10.28	-1.44	0.23
MDF260	7.36	-1.45	0.17
MDF300	5.13	-1.44	0.10

For analyzing the corrosion modification, galvanic corrosion behavior and then quantifying the corrosion rate of the studied alloys, SKPFM method was utilized to measure the volta-potential difference of the intermetallics and matrix. Moreover, image analysis technique using ImageTools software was used to measure the phase fraction of the intermetallics. The volta-potential profile of the ZAXM4211 alloy has been shown in the Fig. 59. The potential difference of the (Mg, $Al)_2Ca$+MgZn and Al_8Mn_5 compounds with the matrix can be obtained by making a line scan from the images (Fig. 59 (c)). The related values have been shown in the Table 5 comparing the result with a pure Mg and Pt. It can be seen that both types of precipitates are nobler than matrix and so they function as a cathode against matrix.

To see the corrosion progress and their reaction with the intermetallic phases, a short time immersion study in a 3.5 wt.% NaCl solution saturated with $Mg(OH)_2$ was carries out and the corrosion products was removed using a solution of 200 g/l CrO_3 and 10g/l (Fig. 60). The results for different samples confirm SKPFM results while both (Mg, $Al)_2Ca$+MgZn and Al_8Mn_5 precipitates are cathodic against the matrix and cause the matrix to be corroded. So corrosion initiates from the intermetallics and α_{Mg} interface, then hydroxide layer form on the exposed surface and hence decreases the corrosion rate of that region. Therefore corrosion propagates on the matrix surface as a filiform corrosion by passing through the intermetallic phases. After the surface was fully covered by the protective hydroxide film, the corrosion rate reduces and get stable.

Based upon the galvanic corrosion between intermetallic compounds and matrix, the corrosion rate obtained from hydrogen evolution technique after seven day immersion versus the $\sum (f_{A,i} \times |\Delta E|)$ value was drawn in the Fig. 61 where $f_{A,i}$ is the fraction of the intermetallic phase (Table 22) and $|\Delta E|$ is the absolute value of the volta-potential difference between the related intermetallic and matrix. Based upon the area fraction of the second phase and volta-potential difference, the $\sum (f_{A,i} \times |\Delta E|)$ values were obtained. Finally the corrosion rate values which was obtained by the hydrogen evolution technique after seven day immersion were drawn versus $\sum (f_{A,i} \times |\Delta E|)$ and a linear curve was fitted to these data. It was obtained that a

proportionally good agreement can be find between the corrosion rate and $\sum(f_{A,i}\times|\Delta E|)$. The results show the main reason for improving the corrosion rate is reducing the fraction of the second phases and hence reducing the galvanic corrosion effect.

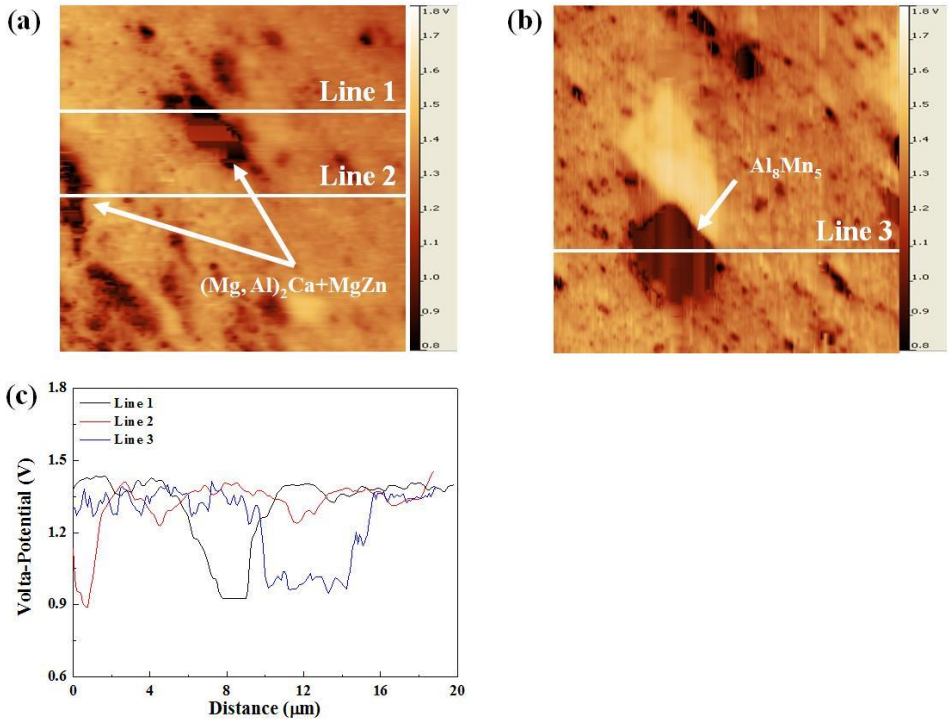

Fig. 59. SKPFM image of the ZAXM4211 alloy showing (a) $(Mg, Al)_2Ca+MgZn$, (b) Al_8Mn_5 intermetallics and (c) corresponding Volta-potential profiles.

Table 21. Volta-potential of matrix and intermetallic phases in ZAXM4211 alloy.

	E_α (mV)	Intermetallic	E_i	$\Delta E=E_\alpha-E_i$
Platinum	210.26±10	-	-	-
Pure Mg	1704.40±15	-	-	-
ZAXM4211	1298.30±44	$(Mg, Al)_2Ca+MgZn$	906±29	392
		Al_8Mn_5	991±35	307

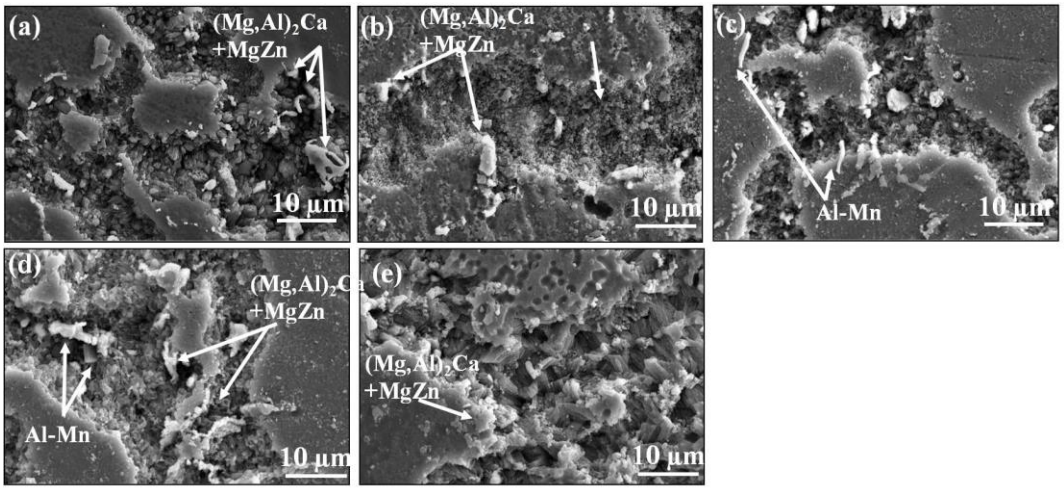

Fig. 60. SEM images of the 0.5 h immersed samples in 3.5 wt. % NaCl with saturated $Mg(OH)_2$, (a) extruded, (b) MDF180, (c) MDF220, (d) MDF260 and (e) MDF300.

Table 22. Phase fraction in the extruded and MDFed alloy.

	Area Fraction of $(Mg, Al)_2Ca$+MgZn	Area Fraction of Al_8Mn_5	$\sum (f_{A,i} \times \lvert\Delta E\rvert)$
Extrusion	0.0658	0.0052	27.26
MDF180	0.0535	0.0049	22.38
MDF220	0.0509	0.0038	21.01
MDF260	0.0442	0.0044	18.57
MDF300	0.0333	0.0049	14.47

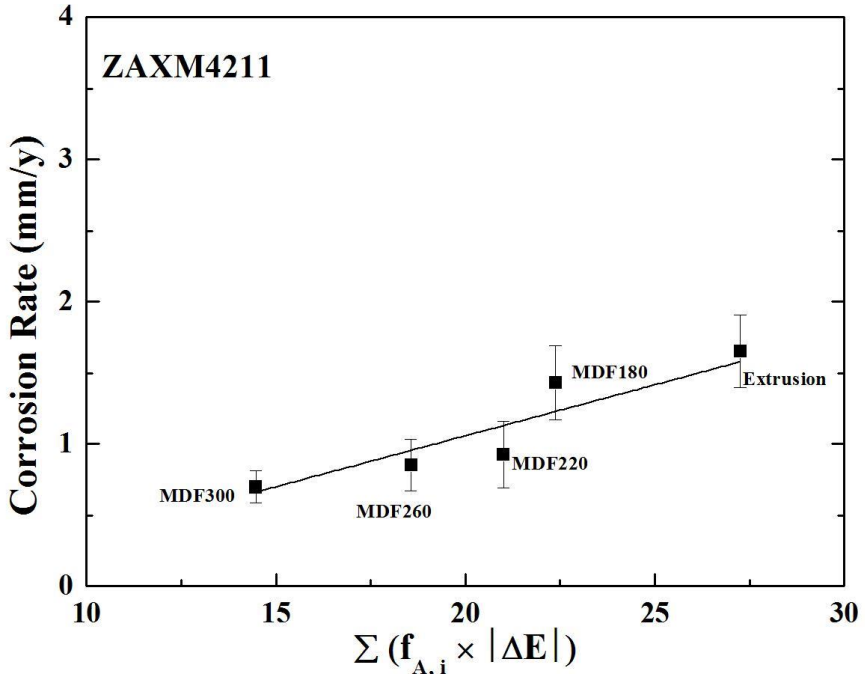

Fig. 61. Relationship between corrosion rate and Volta-potential difference and intermetallic phase fraction of extruded and MDFed ZAXM4211 alloy.

3.10.4 Summary

The ZAXM4211 alloy produced by extrusion and multi directional forging and their mechanical properties and corrosion behavior were studied. The following conclusions were made:

1. Mechanical properties and corrosion behavior of the MDF samples were remarkably improved after MDF and processing temperature played an important role in both mechanical properties and corrosion behavior.

2. The microstructure of ZAXM4211 extruded alloy was uniformed after MDF at all temperatures due to dynamic recrystallization and multi directional deformation. The grain size was reduced after MDF while increasing the MDF temperature increased the grain size.

3. Tensile yield strength was increased after MDF due to grains refinement while they were decreased by increasing the MDF temperature, regarding to grain growth and dissolution of the second phases.

4. A linear line with a good agreement was fitted to the curve of corrosion rate versus $\sum (f_{A,i} \times |\Delta E|)$ and it was found that the corrosion rate reduction at higher MDF temperature is mainly attributed to the dissolution of the second phases into the matrix and then reduction of the $\sum (f_{A,i} \times |\Delta E|)$ value.

3.11 Manufacturing a low corrosion rate alloy using MDF (XM11)

Grains distribution of the extruded and MDFed XM11 samples has been presented in Fig. 62. Since, normal picral acid was not able to detect the grains in the XM11 alloy, the EBSD technique was utilized to show the grain distribution. Extruded sample includes some fine grains which are dynamic recrystallized (DRX) grains and some large grains which are worked grains deformed alongside the extrusion direction. The grains distribution has been uniformed after MDF. In addition, grains size has been enlarged from MDF220 to MDF340 samples.

The phase distribution on the samples has been shown in the Fig. 63. The alloy contains mainly Mg_2Ca and some fine α_{Mn} particles.

Fig. 64 shows the phase percent in the XM11 alloy versus the temperature. Fig. 64 (a) shows the steady state calculation of the XM11 at different temperatures. It can be seen that Mg_2Ca will be dissolved into the matrix and so the phase percent of this phase will be reduced from 220 to 340 ^{o}C. In a same way the experimental measurement of the phase percent using SEM image analysis by ImageTools software shows the phase percent of the Mg_2Ca is reduced gradually by increasing the MDF temperature. While Mn particles containing Fe is so small comparing to the Mg_2Ca and their percentage is not detectible exactly.

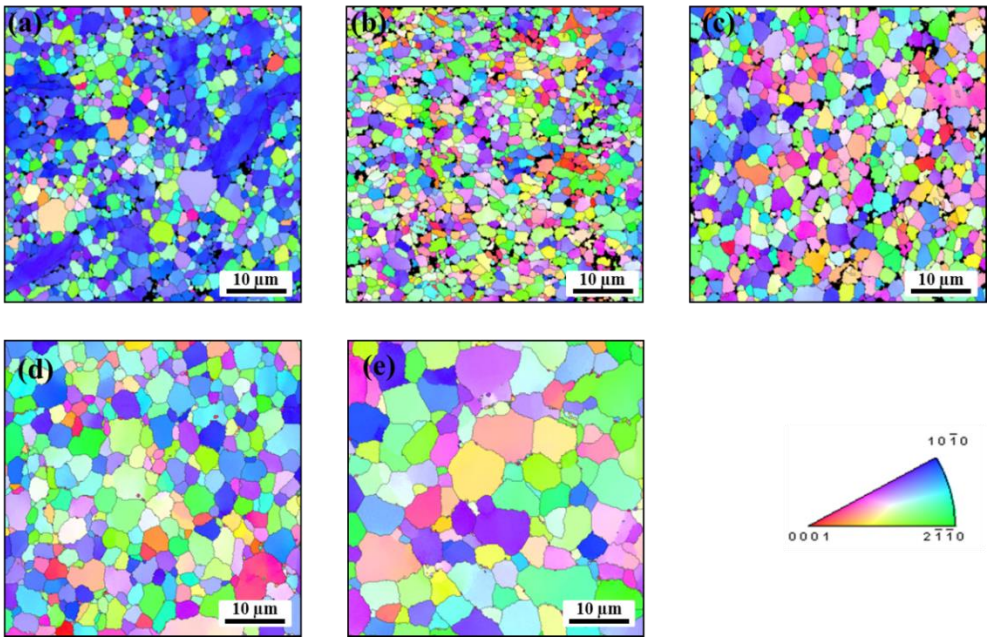

Fig. 62. Grain distribution using EBSD analysis: (a) Extrusion, (b) MDF220, (c) MDF260, (d) MDF300 and (e) MDF340.

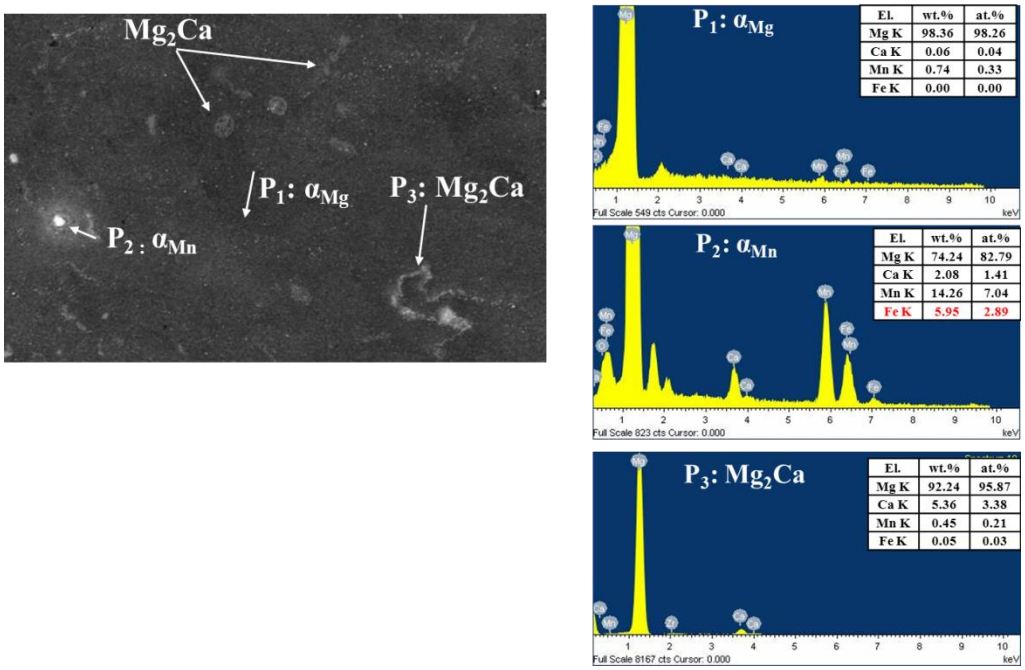

Fig. 63. SEM/EDS image showing the formed phases.

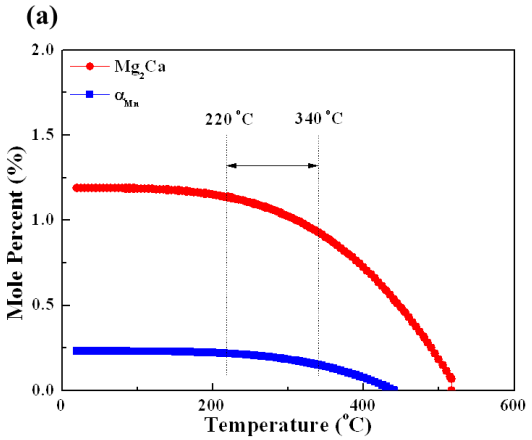

(b)

Sample	$f_{A,\ Mg_2Ca}$ (%)	$f_{A,\ Mn\text{-}Fe}$ (%)
Extrusion	2.01	0.053
MDF220	1.85	0.051
MDF260	1.58	0.061
MDF300	1.38	0.051
MDF340	1.28	0.067

Fig. 64. Phases percent in different temperatures: (a) steady state thermodynamic calculation using JMatPro commercial software, (b) phases percent obtained by image analysis technique using ImageTools software.

3.11.1 Corrosion behavior

Fig. 65 shows the hydrogen evolution and corresponding corrosion rate of extruded and MDF alloys for seven days. The evolved hydrogen and hence corrosion rate of MDF samples are less than that of extruded alloy and increasing the temperature form 220 to 300 ^{o}C results in lower corrosion rate while increasing the temperature from 300 to 340 ^{o}C, corrosion rate sharply increases.

The corrosion rate of the alloys using hydrogen evolution and weight loss methods have been listed in Table 23 showing same trend of corrosion rate.

Photographic and SEM images of the immersed samples after removing corrosion products have been shown in Fig. 66. It can be seen that the extruded and MDF220 and MDF340 samples have been corroded more while severe corrosion can be observed on their surface and MDF300 has the less affected surface.

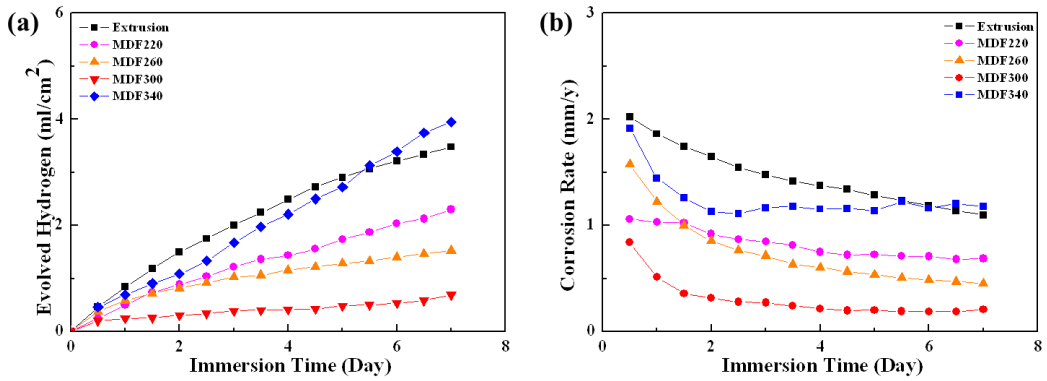

Fig. 65. Immersion study of XM11 alloy: (a) volume of hydrogen and (b) corrosion rate.

Table 23. Immersion corrosion rate values for using hydrogen evolution method: (a) volume of hydrogen and (b) corrosion rate.

Alloy	Hydrogen Volume (ml/cm^2)	Corrosion Rate P_H (mm/y)	Loss Weight ($mg/cm^2/d$)	Corrosion Rate P_W (mm/y)
Extrusion	3.48	1.10	0.56	1.15
MDF220	2.03	0.61	0.42	0.88
MDF260	1.57	0.47	0.38	0.81
MDF300	0.87	0.26	0.26	0.55
MDF340	5.41	1.31	0.94	2.29

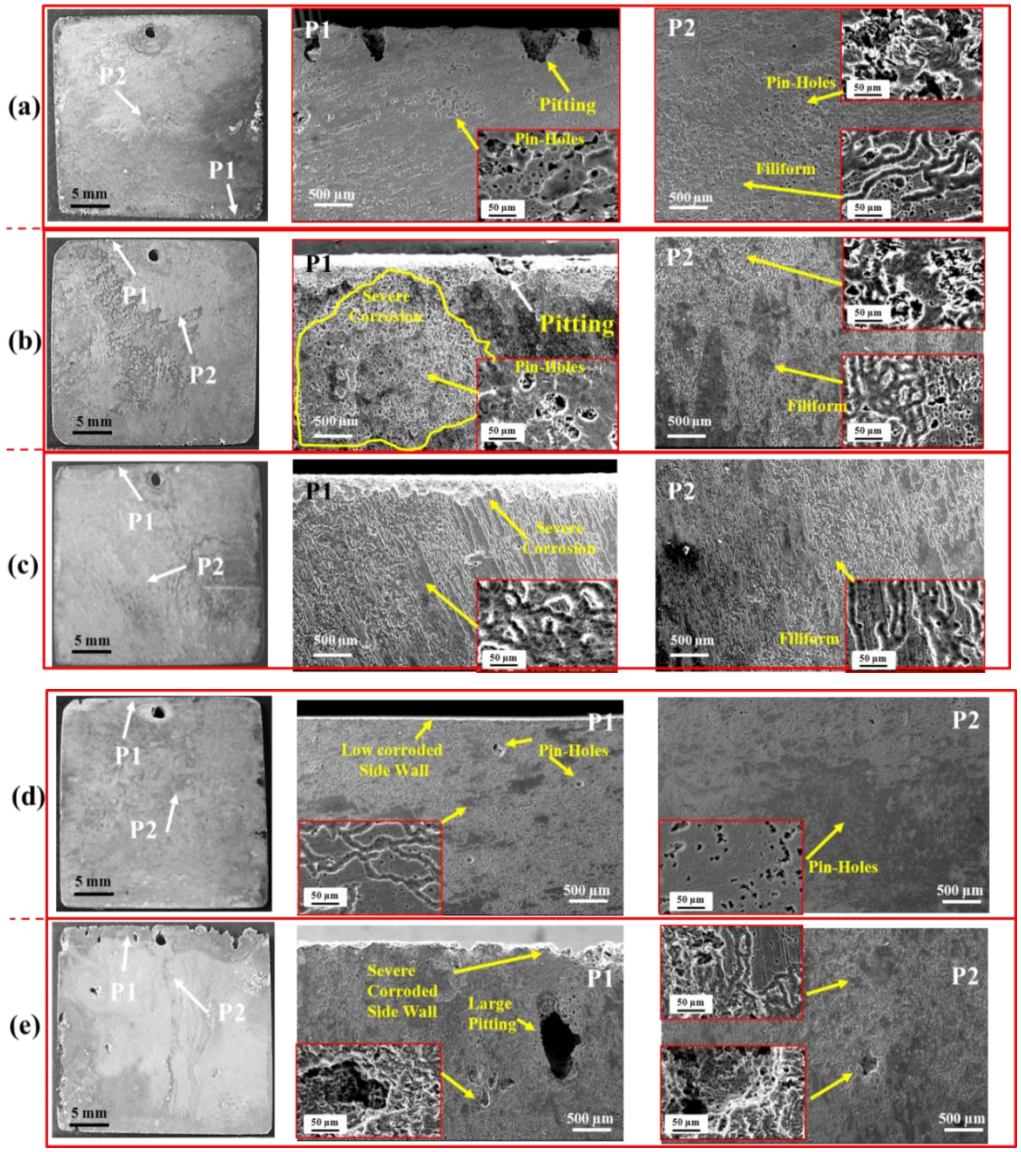

Fig. 66. Photographic and SEM images of corroded surfaces. (a) Extrusion, (b) MDF220, (c) MDF260, (d) MDF300 and (d) MDF340.

The electrochemical study of the extruded and MDFed XM11 during seven days of immersion has been presented in the Fig. 67. The study has been done at the initial stage (0d), first, second, fourth and seventh day of immersion. These plots include OCP (left side) and nyquist plots. The initial stage of OCP for all materials during first 1800 s of immersion shows OCP curves for all materials have fluctuation showing no stable layer has been formed on them; moreover the potential gradually has shifted to the nobler direction showing the formation of the hydroxide layer on the surface of all materials. It can be seen that the potential values is gradually increasing also during the immersion days, however, in some cases the potential decreases after few days. For example, Fig. 67 (a) shows the potential of the extruded alloy has been stabled after four days, where the fluctuations are not appeared on the curve, but after 7 day, the fluctuation still happened on the OCP showing the protective layer has been broken. Fig. 67 (b) shows the same trend while before 4 days, all graphs shows one curve which is related to the matrix, electrochemical analysis after 4 day depicts the second curve which is related to the protective layer. But this layer was broken later on and after seven days, only one curve was distinguished. In the case of MDF220 and MDF340, no stable phase layer was formed on the surface showing no passive layer forms on these two materials. However, the case of MDF260 and MDF300 show the OCP fluctuation-less curves after two days, so there are stable layer forming on them and regarding to not-localized corrosion the passive layer progress properly and protect the entire materials. Specially in the case of MDF300 the enlargement of the Nyquist curves as-well as shifting potential to the nobler values depict that the best uniform corrosion is happening on this material while the passive layer protect the MDF300 material better than the other materials produced under other conditions.

To compare all the studied XM11 alloys the XRD before immersion with Nyquist plots just after 1800 s immersion and XRD and Nyquist curves after seven day immersion were drawn in the Fig. 68. The XRD graphs of bare samples show that all materials include α_{Mg}, α_{Mn} and Mg_2Ca. However a sharp peaks of $MgO/Mg(OH)_2$ has been formed on the MDF260 and MDF300 showing the formation of the

passive layer on these two materials. Comparing the nyquist plots of the initial stage of the corrosion, Fig. 68 (b), shows that at the 0.5h immersion no passive layer has been formed for any material, however the corrosion rate of the MDF300 material is lower than all other materials and the trend is same as the hydrogen evolution and mass loss techniques where corrosion rate decreases from 220 to 300 ^{o}C and it suddenly increases for the MDF340.

For understanding the corrosion behavior of the materials, some other experiments have been done. Here we studied the corrosion behavior of the extruded and MDFed pure Mg to understand the effect of temperature on the samples corrosion. The electrochemical study of the pure Mg including, Tafel, Nyquist and Bod plots have been shown in the Fig. 69. Moreover the electrochemical study values with seven day immersion study values have been shown in the Table 24. All of the results show that increase in the temperature increases the corrosion rate. As previously mentioned in the introduction, majority of the researches shows that corrosion rate increases with increasing the grain size. Here it is in same trend with the pure Mg. But in the case of XM11, another trend was observed while the corrosion rate was decreased from 220 to 300 ^{o}C and increased from 300 to 340 ^{o}C. To understand this behavior effect of galvanic corrosion between matrix and second phase was considered by volta-potential study using SKPFM method and phase fraction measurement using SEM image analysis.

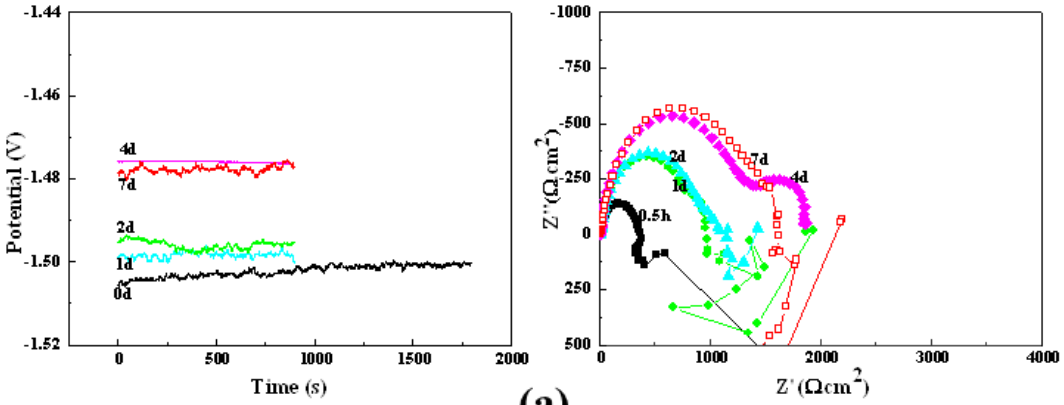
Potential (V)
Time (s)
4d
7d
2d
1d
0d
Z''(Ωcm²)
Z'(Ωcm²)
0.5h

(a)

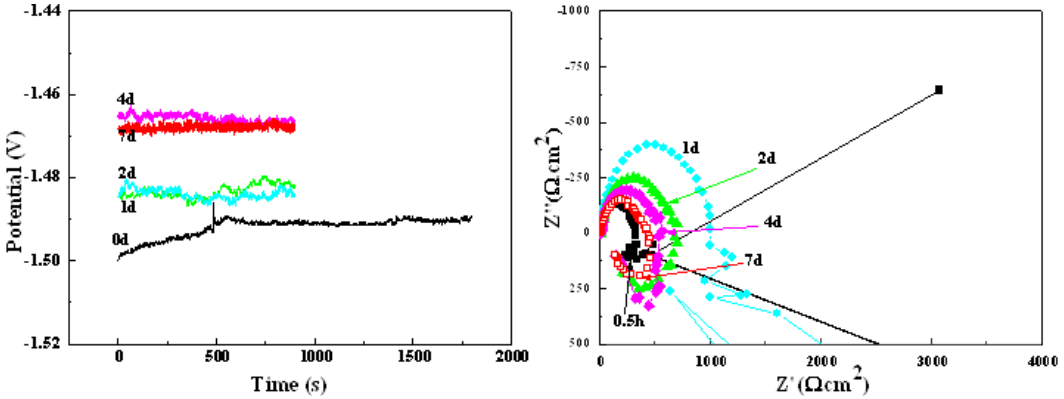
Potential (V)
Time (s)
4d
7d
2d
1d
0d
Z''(Ωcm²)
Z'(Ωcm²)
0.5h

(b)

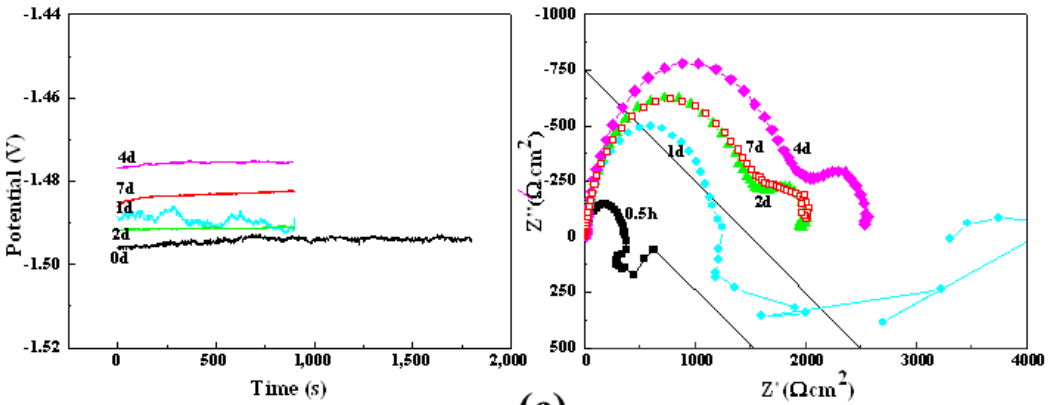
Potential (V)
Time (s)
4d
7d
1d
2d
0d
Z''(Ωcm²)
Z'(Ωcm²)
0.5h

(c)

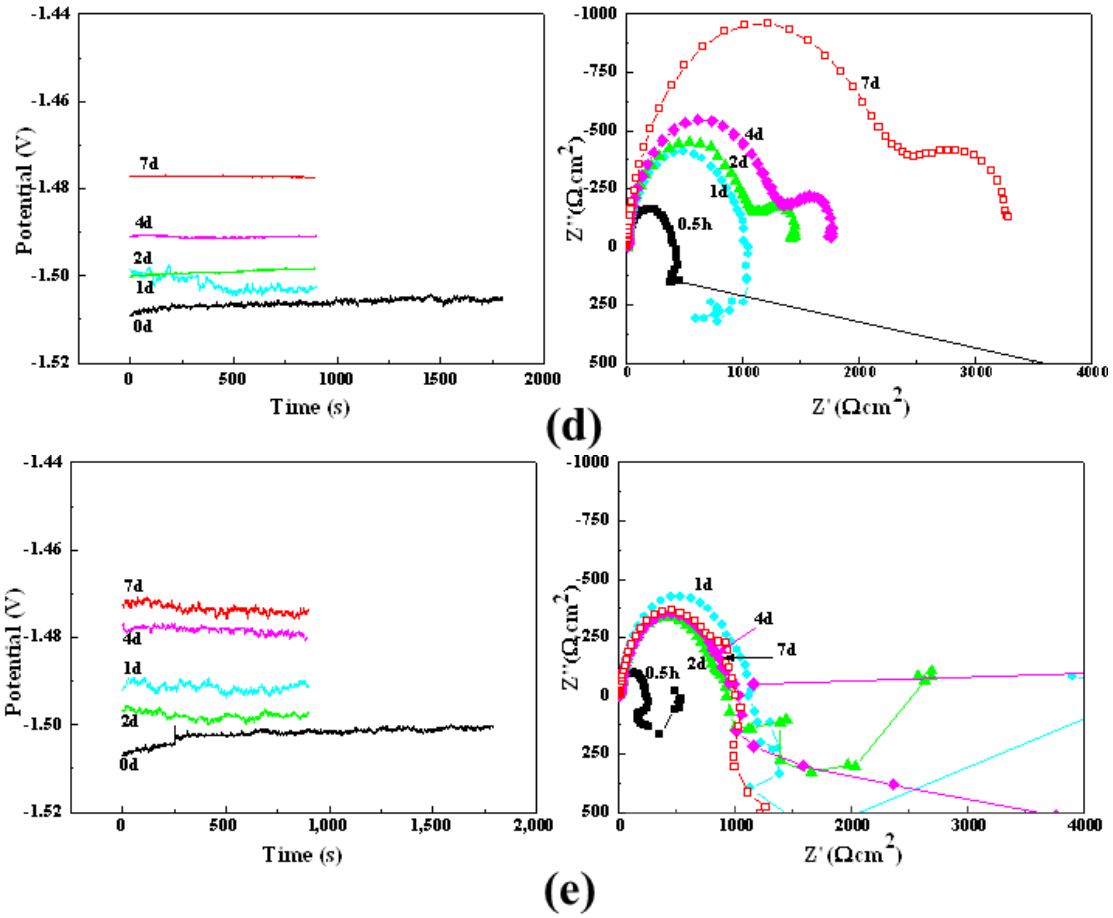

Fig. 67. Electrochemical study of XM11 samples during 7 day immersion in 3.5 wt.% NaCl saturated with Mg(OH). (a) Extrusion, (b) MDF220, (c) MDF260, (d) MDF300 and (e) MDF340.

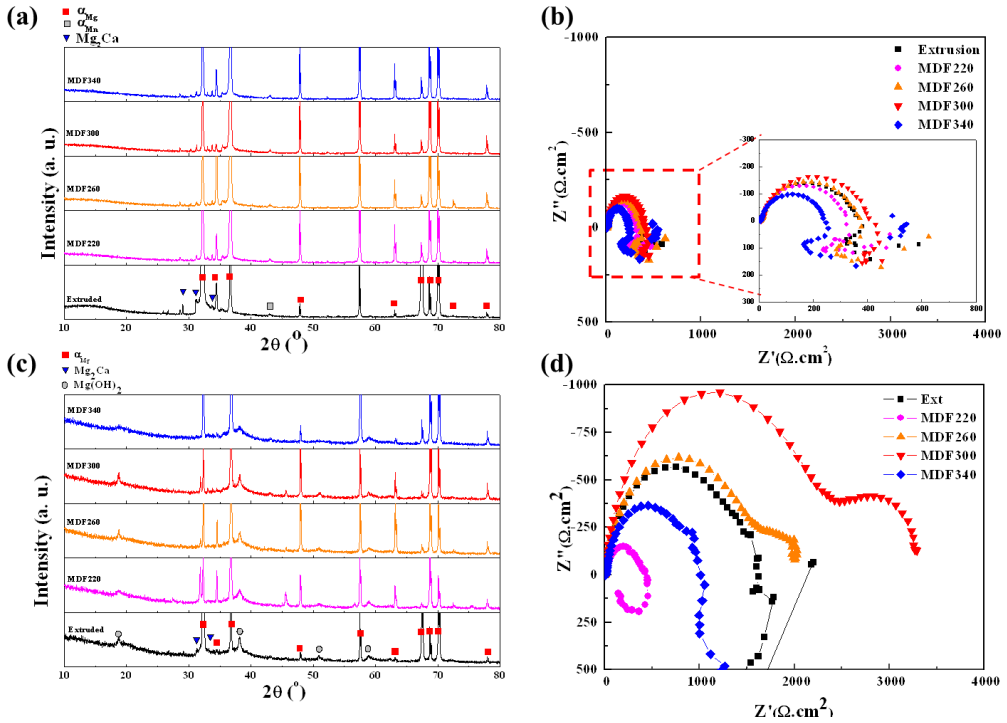

Fig. 68. XRD and Nyquist plots. (a) XRD results of the bared samples (b) Nyquist plots after 0.5 h immersion, (c) XRD results after 7 day immersion and (d) Nyquist plots after 7 day immersion.

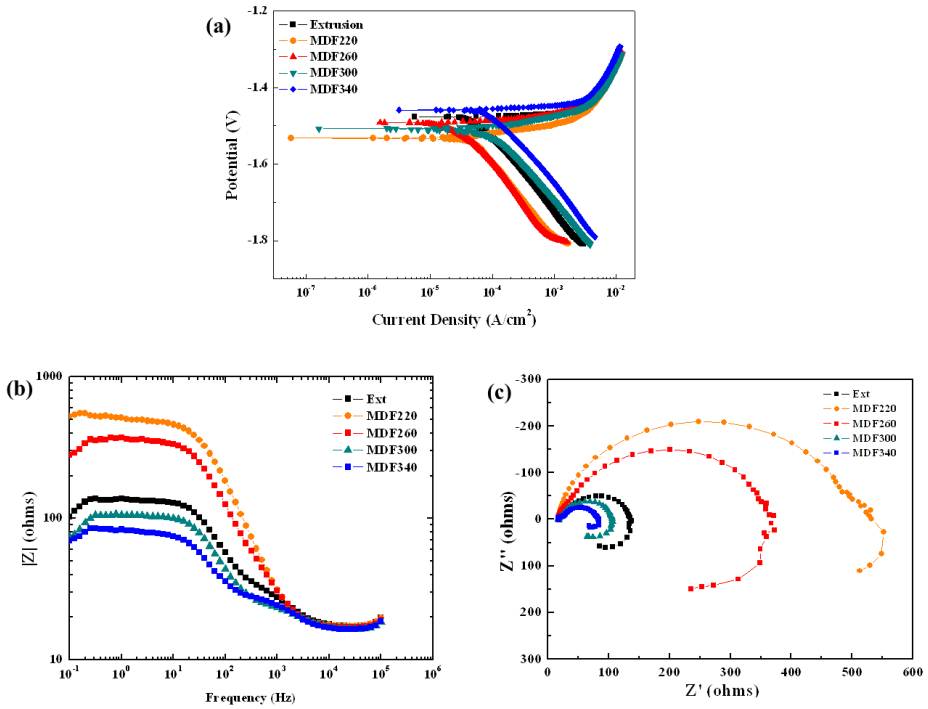

Fig. 69. Electrochemical study of extruded and MDF pure Mg. (a) tafel, (b) bode and (c) nyquist plots.

Table 24. Corrosion rate values of pure Mg obtained by hydrogen evolution technique and electrochemical study.

Sample	**Grain Size (µm)**	**Hydrogen Volume (ml/cm^2)**	**P_H (mm/y)**	**i_{corr} (A/cm^2)**	**E_{corr} (V)**	**P_i (mm/y)**
Extrusion	7.91	9.92	2.97±0.05	52.109	-1.476	1.191
MDF220	3.61	11.38	3.41±0.40	22.701	-1.491	0.519
MDF260	6.20	8.52	2.55±0.05	52.083	-1.532	1.190
MDF300	7.93	15.11	4.55±0.73	79.083	-1.507	1.807
MDF340	12.46	24.01	7.19±0.80	87.847	-1.458	2.007

In order to quantify galvanic corrosion, surface potential differences of secondary phases and matrix, scanning kelvin probe force microscopy (SKPFM) technique was used. Secondary phases are generally detrimental to corrosion of the matrix, therefore the potential difference between the secondary phases and matrix, their fraction, and distribution play a key role in determining Mg corrosion. Fig. 70 shows the SKPFM surface of the matrix and intermetallics and the Volta-potential are given in the Table 25. Mg_2Ca which is the dominant phase by the concentration (Fig. 64) is anodic which is due to the low work function of Ca while α_{Mn} intermetallics are cathodic to the matrix however this phase amount is very low comparing to the Mg_2Ca. As previously mentioned the fraction of the Mg_2Ca is reducing by increasing the MDF temperature, because the Ca can be dissolved into the matrix more, so the area fraction of the galvanic cells is reducing and so the corrosion rate is reducing but from other side, the grain size is increasing. As it was mentioned, the pure Mg which is free of second phase, increasing the grain size results in increasing thee corrosion rate. So it can be mentioned that changing the temperature results in changing two parameters simultaneously which they have opposite effect on the corrosion rate. To quantify these two different parameters it was tried to model the effect of both parameters including galvanic cells and grain size. Galvanic cells as previously mentioned can be explained through the effect of volta-potentiual difference and intermetallics fraction. Grain size effects also can be mentioned through a hall-petch type equation [87]. So finally the following equation was made.

$$CR = CR_0 + b \times f_{A,m} \times D^{-0.5} + c \times \sum(f_{A,i} \times |\Delta E|) \quad (7)$$

Where CR is the corrosion rate which is obtained from hydrogen evolution method, $f_{A,\,i}$ is the area fraction of the each intermerallic, $|\Delta E|$ is the absolute value of the volta-potential difference of the given intermetllic with the matrix and D is the grain size in μm. The grain size, phase fraction and and $\sum f_{Ai} \times |\Delta E|$ is also has been listed in the Table 25.

Fig. 71 depicts the relationship between corrosion rate and the extruded and MDF pure Mg and XM11 alloy the model which is used here and it can be seen that the behavior of the second phase containing materials and second phase material was fitted in a same line showing that MDF temperature increase dissolve the second phases and hence decreases the corrosion rate for the XM11 alloy but for the MDF340 the effect of grain size would be dominant like the behavior of the pure Mg. So the optimum conditions were obtained for the MDF300.

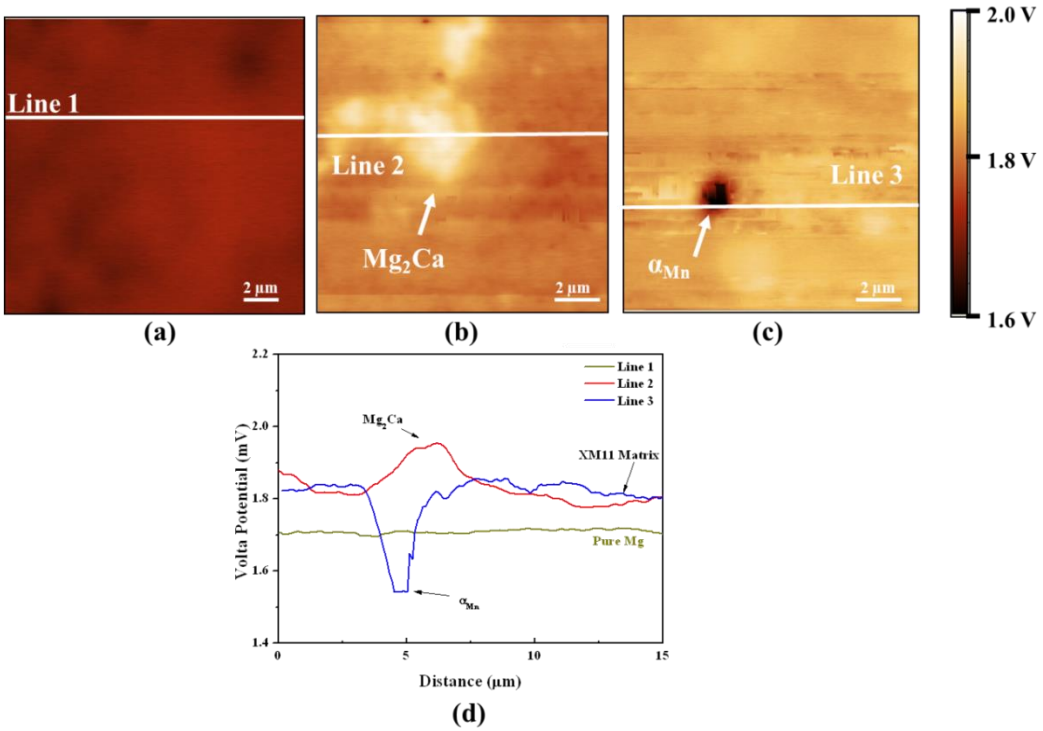

Fig. 70. Volta-potential distribution on the samples surface: (a) Pure Mg, (b) Mg_2Ca in XM11 and (c) α_{Mn} particles and (d) line scans of the SKPFM images.

Table 25. Volta-potential values obtained from SKPFM analysis.

	E_α	Intermetallic	E_i	$\Delta E = E_\alpha - E_i$
Pt	210.26±10	-	-	-
Pure Mg	1704.40±15	-	-	-
XM11	1806.28±27	Mg_2Ca	1932±13	-126
		α_{Mn}	1540±05	266

Table 26. Grain size, fraction of the intermetallic and volta-potential difference of intermetallics relative to the matrix for the studied materials.

		Grain Size	$f_{A, Mg2Ca}$	$f_{A, Mn}$	$\sum f_{A,i} \times \lvert\Delta E\rvert$
Pure Mg	Extrusion	16.5	-		-
	MDF220	8.5	-		-
	MDF260	13.8	-		-
	MDF300	36.3	-		-
	MDF340	81.5	-		-
XM11	Extrusion	2.8	0.020	0.00053	2.52
	MDF220	2.0	0.019	0.00051	2.33
	MDF260	2.7	0.016	0.00061	1.99
	MDF300	3.5	0.014	0.00051	1.74
	MDF340	6.7	0.013	0.00067	1.61

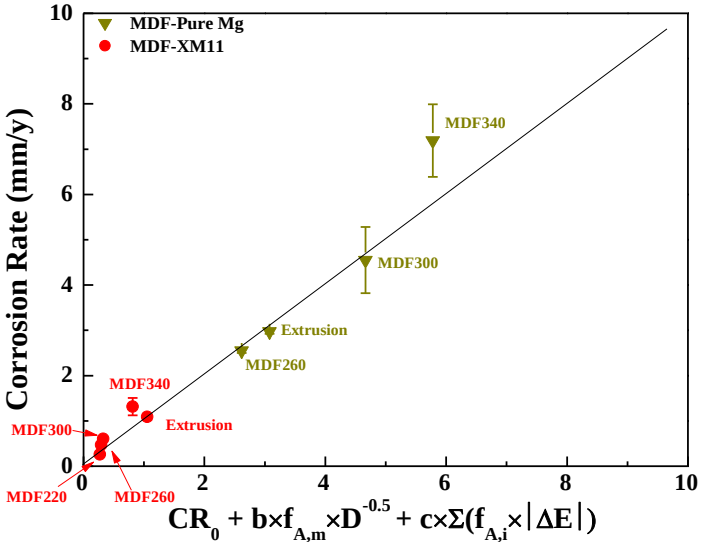

Fig. 71. Corrosion rate modeling of XM11 alloy and pure Mg using phase fraction, Volta-potential difference and grain size.

3.11.2 Summary

Corrosion rate of the XM11 alloy after extrusion and MDF at different temperatures were analyzed and also compared with pure Mg. The following results were obtained:

In the case of XM11, increase in MDF temperature from 220 ^{o}C to 300 ^{o}C decreased the corrosion rate while increase in the temperature from 300 ^{o}C to 340 ^{o}C increased the corrosion rate suddenly. So the lowest corrosion rate was obtained at 300 ^{o}C.

In the case of pure Mg, increase in the MDF temperature increased the corrosion rate which is in agreement with the literature (See: the effect of grain size in page 9)

Image analysis and thermodynamic calculations shows increase in the MDF temperature decreased the fraction of Mg_2Ca. SKPFM results show that Mg_2Ca has an anodic effect. The reduction of the Mg_2Ca results in decrease of galvanic cell.

A model was suggested based upon the grain size, fraction of secondary phase and Volta-potential difference with the matrix.

4 Data analysis

The position of the corrosion rate and yield strength of the studied alloys are compared with the literature and shown in Fig. 72. A good combination of the yield strength and corrosion rate has been achieved in this work where the corrosion rate of XM11-MDF300 is (0.26 mm/y) lower than high purity Mg [7, 133] and yield strength is 170 MPa which is almost 6.5 times higher than that of pure Mg [134]. Moreover, by decreasing the processing (SR or MDF) temperature, high yield strength material has been obtained. The yield strength of ZAXM4211 alloy screw rolled at 220 ^{o}C (SR220) was achieved to the 315 MPa.

4.1 Mechanical properties

The yield strength relationship against grain size ($\mu m^{-0.5}$) has been drawn in the Fig. 73. The hall-petch equation ($YS=YS_0+K/\sqrt{D}$) for all series has been shown in the graph. As can be seen, SR samples have the highest strengthening coefficient showing the remarkable effect of SR in the mechanical properties.

Addition of alloying elements to the XM11 alloy increased the materials constant for the starting stress for dislocation movement (YS_0) due to precipitation hardening and improved the yield strength. However, Sn containing alloy has low strengthening coefficient which is related to instability of these phases on the formed second phases.

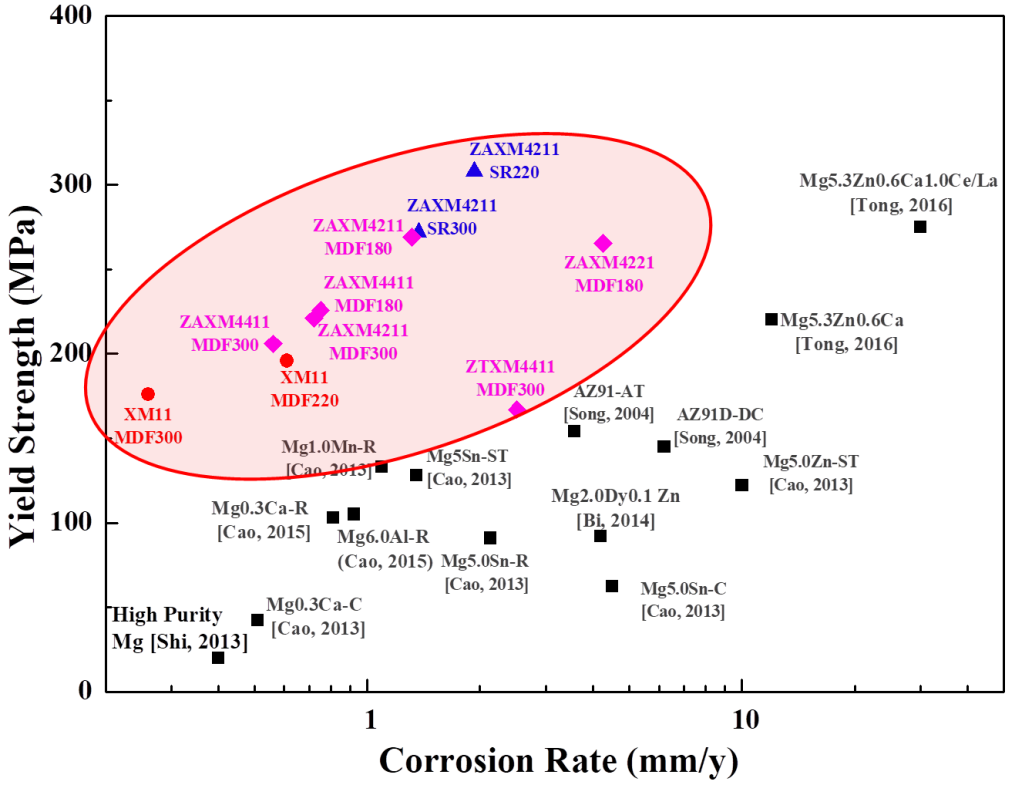

Fig. 72. Corrosion rate vs. yield strength of the studied alloys compared with the literature.

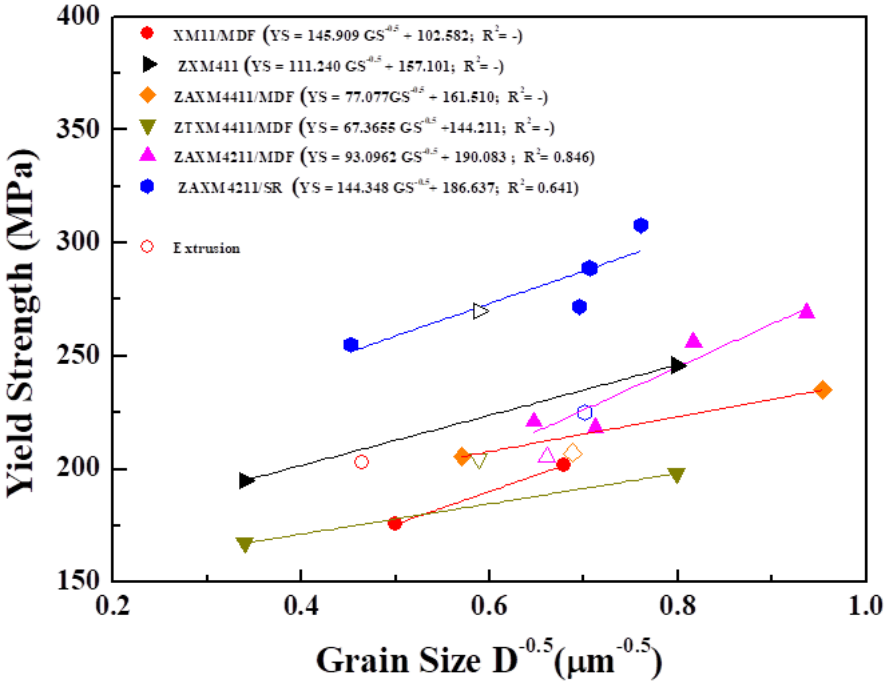

Fig. 73. The relationship between yield strength and grain size.

4.2 Corrosion behavior

To quantitatively analysis of the effect of parameters influencing the corrosion rate, it was tried to correlate corrosion rate with the several parameters as explained in the introduction section (See: section 1.3). Microstructural parameters including alloy composition, grain size, fraction of second phase, volta-potential difference between second phase and matrix.

All the obtained corrosion values including some of the available literature data were drawn versus $\Sigma(f_{A,i}\times|\Delta E|)$ as shown in the Fig. 74. The corrosion rate can be explained by this parameter for most of the alloys, but there is no way to explain the corrosion behavior of Pure Mg.

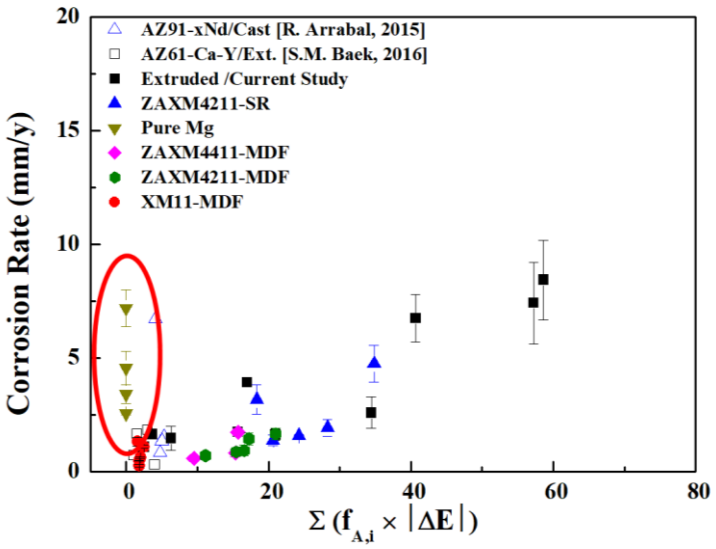

Fig. 74. The relationship between the corrosion rate and fraction of the second phase (intermetallic) and volta-potential difference [123, 128, 137].

To derive a generalized equation, the parameters affecting the corrosion rate was individually discussed and quantified. As mentioned in the introduction part, the corrosion rate might be influenced by the microstructure. The microstructure parameters can be classified as composition, matrix, grain boundaries and second phases.

4.2.1 Composition:

Composition has two aspects of influencing on the corrosion rate as follows:

4.2.1.1. Intrinsic Effect:

- **Surface energy**: the surface energy (showing surface nobility or weakness) of the matrix can be changed by dissolution of solutes into the matrix), this value might be also changed by changing the lattice strain (dislocation density). This value can be obtained by SKPFM method which has been previously discussed. OCP also can be used but it should be considered that OCP includes other effects like grain boundary and second phases.
- **Secondary phases**: changing the alloy composition will produce different secondary phases with different fractions. (This effect will be discussed later).
- **Orientation (Texture Effect)**: The corrosion rate of various orientations will be affected by changing the composition ($CR_{T,C}$). For the alloys directionally has been deformed and have intense texture, this term need to be considered. Different crystallographic orientations have different corrosion rate. Hence, the corrosion rate related to the effect of orientation can be considered as $a_C \times (\sum f_{A,or} \times CR_{or})$ where $a_{C,}$ $f_{A,ori,}$ and CR_{or} are the effects of solutes and dislocation density in changing the corrosion rate of each orientation, the area fraction of each orientation and corrosion rate of the related orientation, respectively.

4.2.1.2. Extrinsic Effect (Passivation:$CR_{P,C}$)

Passivation is the creation of an outer layer of shield material that is applied as a micro-coating, created by chemical reaction with the base material. The passivity behavior is related to the several parameters, where the most important ones are their formation gibbs free energy (or enthalpy in a fixed temperature), cohesive energy which shows their stability [86], pilling-bedworth ratio which shows their compactness and also their coherency with the matrix. This value has been assumed constant for each alloy here.

4.2.2 Matrix

4.2.2.1. Grain Size Effect

Corrosion rate is related to the grain boundary length (GBL) and grain boundary length is linearly related to $D^{-0.5}$, where D is the grain size. Therefore the Eq. (8) can be changed to:

$$CR = a + b \times D^{-0.5} \quad (8)$$

Since grain size effect should be applied just on the matrix, so area fraction of matrix, $f_{A,m}$ (=1- $\Sigma f_{A,i}$) was multiplied to the D term. It means the mentioned equation could be changed as:

$$CR = a + b \times f_{A,m} \times D^{-0.5} \quad (9)$$

As explained in the introduction section, grain size may affect in two different ways [90, 93, 96, 138]:

5. Stabilization of the surface film (extrinsic effect) ($-b_1 \times f_{A,m} \times D^{-0.5}$) (for small grains or solutions providing passivation. "-" depicts that corrosion rate increases with increasing grain size) [90, 93, 139, 140]
6. Initiation site of corrosion (intrinsic effect) ($+b_2 \times f_{A,m} \times D^{-0.5}$) (for very large grains including single- or bi-crystals or in solutions where passivation is

not possible. “+” depicts that corrosion rate decreases with increasing grain size) [40, 96, 138].

4.2.3 Second phase (Intermetallic)

One of the most important factors influencing the corrosion rate of the alloys is the galvanic corrosion. Galvanic corrosion happens between the intermetallic phases and matrix. The potential difference between the second phase (intermetallic) and matrix is the driving force for the electrons to move from anode to cathode and form the galvanic cells. In addition, the area fraction of the intermetallic phase determines the effective surface involved in the electron current density. The anodic second phase in contact with the nobler matrix in a galvanic cell degrades whereas the matrix degrades when the second phase is nobler to the matrix. Hence, the second phase effect was divided into two mechanisms including anodic second phase ($c_a \times \Sigma(f_{A,a} \times |\Delta E_a|)$) and cathodic second phase ($c_c \times \Sigma(f_{A,c} \times |\Delta E_c|)$) and the corrosion rate related to the second phase (intermetallics) was defined as:

$$CR_i = A + [c_a \times \Sigma(f_{A,a} \times |\Delta E_a|] + [c_c \times \Sigma(f_{A,c} \times |\Delta E_c|] \quad (10)$$

Where A, c_a , c_c, $f_{A,a}$, $f_{A,c}$, $|\Delta E_a|$ and $|\Delta E_c|$ are the corrosion rate of the material without any second phase, contribution of anodic second phases, contribution of cathodic second phases, area fraction of anodic phase, area fraction of cathodic phase, absolute value of volta-potential difference of matrix relative to the anodic second phase and volta-potential difference of matrix relative to the cathodic second phase, respectively.

Since, increase in ΔE, regardless of cathodic or anodic phase, increases the corrosion rate, we can use $|\Delta E|$ and simplify this terms as: $[c \times \Sigma(f_{A,i} \times |\Delta E|)]$ where c and $f_{A,i}$ are the contribution of second phase and area fraction of the second phase (intermetallic).

4.2.4 Total corrosion rate

The total corrosion rate equation can be written as:

$$CR = a_C \times (\sum f_{or} \times CR_{or}) - CR_{P,C} - b_1 \times f_{A,m} \times D^{-0.5} + b_2 \times f_{A,m} \times D^{-0.5} + c \times \Sigma (f_{A,i} \times |\Delta E|) \qquad (11)$$

Where the first term ($a_C \times (\sum f_{or} \times CR_{or})$) is the corrosion rate of grains related to the texture, change in surface energy by the addition of alloying elements to pure metal or changing the dislocation density of grains. $CR_{P,C}$ is the passivation effect which can be changed by the composition change. In the present study, the texture effect has been assumed constant due to randomized texture (see the supplementary data). However, when the basal planes fraction changes, the area fraction of each orientation should be considered to analyze the corrosion results. Therefore, the above-mentioned equation can be rewritten as:

$$CR = [CR_{T,C} - CR_{P,C}] - b_1 \times f_{A,m} \times D^{-0.5} + b_2 \times f_{A,m} \times D^{-0.5} + c \times \Sigma (f_{A,i} \times |\Delta E|) \qquad (12)$$

Considering $CR_{T,C} - CR_{P,C} = CR_0$:

$$CR = CR_0 - b_1 \times f_{A,m} \times D^{-0.5} + b_2 \times f_{A,m} \times D^{-0.5} + c \times \Sigma (f_{A,i} \times |\Delta E|) \qquad (13)$$

For unifying the effect of grain size, we may consider $b = b_2 - b_1$ and rewrite the equation as Equaiton (14) which is the final equation:

$$CR = CR_0 + b \times f_{A,m} \times D^{-0.5} + c \times \Sigma (f_{A,i} \times |\Delta E|) \qquad (14)$$

CR_0 is related to the matrix surface energy (changing by concentration of the solute atoms and density of dislocations), distribution of different orientations. b is the contribution of the grain size on corrosion rate which is related to the solution media. It should be considered that this value is positive for very large grains, and negative for fine grains (the critical point is related to the solution). c is the contribution of the second phases and could be changed by the type of secondary phases (anodic, cathodic) and also the solution type and concentration.

It can finally be mentioned that, considering the effect of alloy composition, grain size and galvanic cell can predict the corrosion rate with a good agreement as it was shown in the Fig. 75.

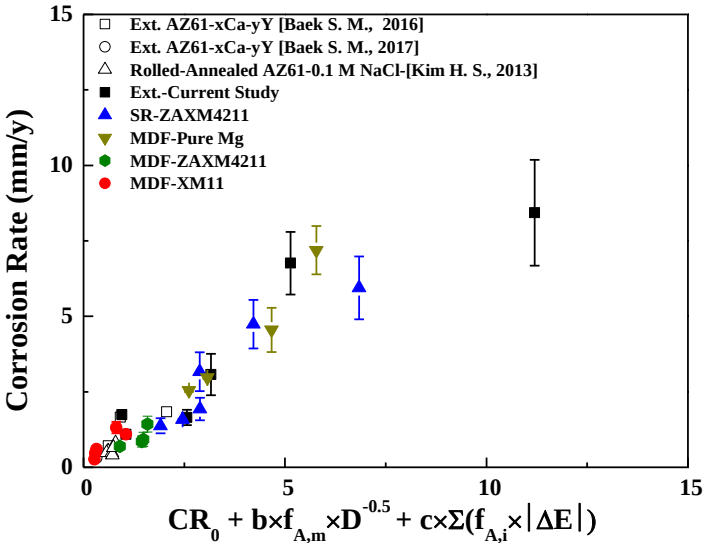

(a)

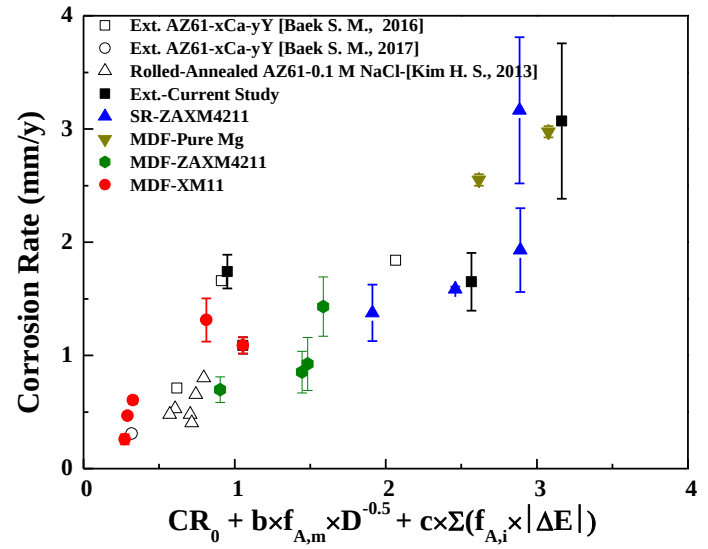

(b)

Fig. 75. (a) the relationship between experimental corrosion rate results with the proposed corrosion rate model $CR = CR_0 + b \times f_{A,m} \times D^{-0.5} + c \times \Sigma(f_{A,i} \times |\Delta E|)$; (b) the magnified portion for the lower corrosion rate materials.

5 Conclusions

Several Mg alloys as well as pure Mg were produced through different processes including casting, extrusion, screw rolling (SR) and multi directional forging (MDF). The mechanical properties and corrosion behavior of the extruded materials were studied and materials with the best mechanical properties and corrosion resistance were further subjected to the SR and MDF. The related processing conditions of the lateral processes, SR and MDF were changed and mechanical properties and corrosion behavior of the produced materials were evaluated. The following conclusions were made:

- Increasing Mn content up to 0.5 wt. % decreased the corrosion rate and increased the hardness value.
- Ca addition to ZM41 and ZAM421 alloy decreased the grain size and increased the fraction of second phase and hence yield strength, hardness and UTS increased. However, Ca addition decreased the tensile elongation. Addition of Ca in the ZAM421 from 0.0 to 0.6 wt. % didn't change the corrosion rate significantly while its addition from 0.6 to 1.2 wt.%, suddenly increased the corrosion rate which is attributed to the increase of the second phase fraction and hence galvanic corrosion.
- Al addition in the ZXM411 alloy marginally decreased the grain size and decreased the yield strength from 0.0 to 2.0 wt.% Al due to texture randomization. The yield strength and elongation increased from 2.0 to 4.0 wt.% Al, however UTS was not changed significantly.
- Sn addition to ZXM411 alloy marginally increased the grain size and hence decreased the yield strength and UTS but increased the elongation and increased the corrosion rate.
- Zn addition in XM11 alloy decreased the grain size and hence increased the yield strength, UTS and elongation. Actually, no plasticity was observed in the XM11 extruded alloy and so addition of Zn, like Al and Sn enhanced the plasticity. However the corrosion rate of the XM11 alloy after addition of Zn was increased due to the formation of the second phases.

- The ZAXM4211 alloy was produced by extrusion and screw rolling and its mechanical properties and corrosion behavior were studied. The samples processed at lower temperatures have finer microstructure. Decreasing the temperature of screw rolling increased the hardness, UTS and YS due to the grain refinement and dissolution of the second phases. Area fraction of intermetallics gradually decreased with increasing the SR temperature. Increase in the temperature had two controversial effects including (i) dissolution of the secondary phase into the matrix and (ii) increase in the grain size. Dissolution of the secondary phases into the matrix results in decreasing the number of galvanic cells effect and corrosion rate, while increasing the grain size results in increasing the corrosion rate. Based upon the results of current study, to produce lowest corrosion rate material, best combination of grain size and fraction of the secondary phase can be achieved at 300 ^{o}C.

- The extruded ZAXM4211 alloy was subjected to multi directional forging and their mechanical properties and corrosion behavior were also studied. Mechanical properties and corrosion behavior of the MDF samples were remarkably improved after MDF and processing temperature played an important role controlling both mechanical properties and corrosion behavior. The microstructure of ZAXM4211 extruded alloy was uniformed after MDF at all temperatures due to dynamic recrystallization and multi directional deformation. The grain size reduced after MDF while increasing the MDF temperature increased the grain size. Tensile yield strength was increased after MDF due to grains refinement while they were decreased by increasing the MDF temperature, regarding to grain growth and dissolution of the second phases. Several alloys were also subjected to MDF at different temperatures and same trend as SR and MDF were obtained. The yield strength of XM11 was decreased by increasing MDF temperature but, corrosion rate was decreased from 220 to 300 ^{o}C and increased from 300 to 340 ^{o}C.
- A very low corrosion rate material was obtained from XM11 alloy MDFed at 300 ^{o}C. The corrosion rate of this material was 0.26 mm/y which is much lower than that of the high purity Mg (0.39 mm/y).

- An experimental model was suggested based upon the composition, grain size (D), volta-potential difference of the second phase and matrix ($|\Delta E|$) and fraction of the second phase ($f_{A,i}$). Then mentioned terms were mixed and the [$CR_0 + b \times f_{A,i} \times D^{-0.5} + c \times \Sigma(f_{A,i} \times |\Delta E|)$] equation was obtained. The corrosion rate of the all alloys as well as pure Mg produced through different processes was applied to this equation and a good agreement was obtained.

6 Bibliography

[1] F. Cao, Z. Shi, G.-L. Song, M. Liu, M.S. Dargusch, A. Atrens, Influence of hot rolling on the corrosion behavior of several Mg–X alloys, Corrosion Science 90 (2015) 176-191.

[2] F. Witte, The history of biodegradable magnesium implants: a review, Acta Biomater 6(5) (2010) 1680-92.

[3] T. Abu Leil, N. Hort, W. Dietzel, C. Blawert, Y. Huang, K.U. Kainer, K.P. Rao, Microstructure and corrosion behavior of Mg-Sn-Ca alloys after extrusion, Transactions of Nonferrous Metals Society of China 19(1) (2009) 40-44.

[4] M. Ben-Haroush, G. Ben-Hamu, D. Eliezer, L. Wagner, The relation between microstructure and corrosion behavior of AZ80 Mg alloy following different extrusion temperatures, Corrosion Science 50(6) (2008) 1766-1778.

[5] H.R. Bakhsheshi-Rad, M.H. Idris, M.R. Abdul-Kadir, A. Ourdjini, M. Medraj, M. Daroonparvar, E. Hamzah, Mechanical and bio-corrosion properties of quaternary Mg–Ca–Mn–Zn alloys compared with binary Mg–Ca alloys, Materials & Design 53 (2014) 283-292.

[6] G. Song, A. Atrens, Understanding Magnesium Corrosion—A Framework for Improved Alloy Performance, Advanced Engineering Materials 5(12) (2003) 837-858.

[7] F. Cao, Z. Shi, G.-L. Song, M. Liu, A. Atrens, Corrosion behaviour in salt spray and in 3.5% NaCl solution saturated with Mg(OH)2 of as-cast and solution heat-treated binary Mg–X alloys: X=Mn, Sn, Ca, Zn, Al, Zr, Si, Sr, Corrosion Science 76 (2013) 60-97.

[8] M.P. Staiger, A.M. Pietak, J. Huadmai, G. Dias, Magnesium and its alloys as orthopedic biomaterials: a review, Biomaterials 27(9) (2006) 1728-34.

[9] M. Diez, H.-E. Kim, V. Serebryany, S. Dobatkin, Y. Estrin, Improving the mechanical properties of pure magnesium by three-roll planetary milling, Materials Science and Engineering: A 612 (2014) 287-292.

[10] F. Cao, G.-L. Song, A. Atrens, Corrosion and passivation of magnesium alloys, Corrosion Science 111 (2016) 835-845.

[11] A. Baghani, A. Bahmani, D. Parviz, V. Naser, M.O. Shabani, Application of Computational Fluid Dynamics to study the effects of Sprue Base Geometry on the Surface and Internal Turbulence in gravity casting, Proceedings of the Institution of Mechanical Engineers, Part L: Journal of Materials: Design and Applications 229(2) (2013) 106-116.
[12] A. Bahmani, N. Hatami, N. Varahram, P. Davami, M.O. Shabani, A mathematical model for prediction of microporosity in aluminum alloy A356, The International Journal of Advanced Manufacturing Technology 64(9) (2013) 1313-1321.
[13] A. Bahmani, G.B. Eisaabadi, P. Davami, N. Varahram, M.O. Shabani, Effects of hydrogen level and cooling rate on ultimate tensile strength of Al A319 alloy, Russian Journal of Non-Ferrous Metals 55(4) (2014) 365-370.
[14] J. Campbell, castings practice: the 10 rules of casting, castings practice: the 10 rules of casting, Butterworth-Heinemann, Oxford, 2004.
[15] G. Song, Corrosion mechanisms of magnesium alloys, Adv Eng Mech 1 (2000) 11-33.
[16] K. Gusieva, C.H.J. Davies, J.R. Scully, N. Birbilis, Corrosion of magnesium alloys: the role of alloying, International Materials Reviews 60(3) (2014) 169-194.
[17] F. Witte, N. Hort, C. Vogt, S. Cohen, K.U. Kainer, R. Willumeit, F. Feyerabend, Degradable biomaterials based on magnesium corrosion, Current Opinion in Solid State and Materials Science 12(5-6) (2008) 63-72.
[18] N.D. Nam, M. Mathesh, M. Forsyth, D.S. Jo, Effect of manganese additions on the corrosion behavior of an extruded Mg–5Al based alloy, Journal of Alloys and Compounds 542 (2012) 199-206.
[19] S.A. Khan, Y. Miyashita, Y. Mutoh, Z.B. Sajuri, Influence of Mn content on mechanical properties and fatigue behavior of extruded Mg alloys, Materials Science and Engineering: A 420(1-2) (2006) 315-321.
[20] J. Zhang, K. Liu, D. Fang, X. Qiu, P. Yu, D. Tang, J. Meng, Microstructures, mechanical properties and corrosion behavior of high-pressure die-cast Mg–4Al–0.4Mn–xPr (x=1, 2, 4, 6) alloys, Journal of Alloys and Compounds 480(2) (2009) 810-819.

[21] J.D. Robson, D.T. Henry, B. Davis, Particle effects on recrystallization in magnesium–manganese alloys: Particle pinning, Materials Science and Engineering: A 528(12) (2011) 4239-4247.
[22] M. Liu, P.J. Uggowitzer, A.V. Nagasekhar, P. Schmutz, M. Easton, G.-L. Song, A. Atrens, Calculated phase diagrams and the corrosion of die-cast Mg–Al alloys, Corrosion Science 51(3) (2009) 602-619.
[23] M. Liu, G.-L. Song, Impurity control and corrosion resistance of magnesium–aluminum alloy, Corrosion Science 77 (2013) 143-150.
[24] D.H. Cho, B.W. Lee, J.Y. Park, K.M. Cho, I.M. Park, Effect of Mn addition on corrosion properties of biodegradable Mg-4Zn-0.5Ca-xMn alloys, Journal of Alloys and Compounds 695 (2017) 1166-1174.
[25] Z. Li, X. Gu, S. Lou, Y. Zheng, The development of binary Mg-Ca alloys for use as biodegradable materials within bone, Biomaterials 29(10) (2008) 1329-44.
[26] A.A. Luo, Creep and microstructure of magnesium-aluminum-calcium based alloys, Met and Mat Trans A 33 (2002) 567-575.
[27] H.R. Bakhsheshi Rad, M.H. Idris, M.R.A. Kadir, S. Farahany, A. Fereidouni, M.Y. Yahya, Characterization and Corrosion Behavior of Biodegradable Mg-Ca and Mg-Ca-Zn Implant Alloys, Applied Mechanics and Materials 121-126 (2011) 568-572.
[28] H.R. Bakhsheshi-Rad, M.R. Abdul-Kadir, M.H. Idris, S. Farahany, Relationship between the corrosion behavior and the thermal characteristics and microstructure of Mg–0.5Ca–xZn alloys, Corrosion Science 64 (2012) 184-197.
[29] Y. Zhang, J. Li, J. Li, Effects of calcium addition on phase characteristics and corrosion behaviors of Mg-2Zn-0.2Mn-xCa in simulated body fluid, Journal of Alloys and Compounds 728(Supplement C) (2017) 37-46.
[30] C.D. Yim, J. Yang, S.K. Woo, H.-Y. Ha, B.S. You, The effects of microstructural factors on the corrosion behaviour of Mg–5Sn–xZn (x=1, 3wt%) extrusions, Corrosion Science 90 (2015) 597-605.
[31] S.D. Mathew, The effect of aluminium content on the mechanical properties and microstructure of die cast binary magnesium-aluminium alloys, Mat. Trans. 4 (2006) 977-982.

[32] C.D. Lee, C.S. Kang, K.S. Shin, Effect of galvanic corrosion between precipitate and matrix on corrosion behavior of As-cast magnesium-aluminum alloys, Metals and Materials 6(4) (2000) 351-358.
[33] Y. Sun, B. Zhang, Y. Wang, L. Geng, X. Jiao, Preparation and characterization of a new biomedical Mg–Zn–Ca alloy, Materials & Design 34 (2012) 58-64.
[34] N. Li, Y. Zheng, Novel Magnesium Alloys Developed for Biomedical Application: A Review, Journal of Materials Science & Technology 29(6) (2013) 489-502.
[35] S. Zhang, X. Zhang, C. Zhao, J. Li, Y. Song, C. Xie, H. Tao, Y. Zhang, Y. He, Y. Jiang, Y. Bian, Research on an Mg-Zn alloy as a degradable biomaterial, Acta Biomater 6(2) (2010) 626-40.
[36] X. Zhang, G. Yuan, L. Mao, J. Niu, P. Fu, W. Ding, Effects of extrusion and heat treatment on the mechanical properties and biocorrosion behaviors of a Mg-Nd-Zn-Zr alloy, J Mech Behav Biomed Mater 7 (2012) 77-86.
[37] G. Ben-Hamu, D. Eliezer, K.S. Shin, The role of Si and Ca on new wrought Mg–Zn–Mn based alloy, Materials Science and Engineering: A 447(1-2) (2007) 35-43.
[38] E. Mostaed, M. Vedani, M. Hashempour, M. Bestetti, Influence of ECAP process on mechanical and corrosion properties of pure Mg and ZK60 magnesium alloy for biodegradable stent applications, Biomatter 4 (2014) e28283.
[39] G.B. Hamu, D. Eliezer, L. Wagner, The relation between severe plastic deformation microstructure and corrosion behavior of AZ31 magnesium alloy, Journal of Alloys and Compounds 468(1-2) (2009) 222-229.
[40] Z. Li, S.-j. Zhou, N. Huang, Effects of ECAE processing temperature on the microstructure, mechanical properties, and corrosion behavior of pure Mg, International Journal of Minerals, Metallurgy, and Materials 22(6) (2015) 639-647.
[41] D. Song, A.B. Ma, J.H. Jiang, P.H. Lin, D.H. Yang, J.F. Fan, Corrosion behaviour of bulk ultra-fine grained AZ91D magnesium alloy fabricated by equal-channel angular pressing, Corrosion Science 53(1) (2011) 362-373.

[42] M.-K. Chung, Y.-S. Choi, J.-G. Kim, Y.-M. Kim, J.-C. Lee, Effect of the number of ECAP pass time on the electrochemical properties of 1050 Al alloys, Materials Science and Engineering: A 366(2) (2004) 282-291.
[43] E. Mostaed, M. Hashempour, A. Fabrizi, D. Dellasega, M. Bestetti, F. Bonollo, M. Vedani, Microstructure, texture evolution, mechanical properties and corrosion behavior of ECAP processed ZK60 magnesium alloy for biodegradable applications, J Mech Behav Biomed Mater 37 (2014) 307-22.
[44] F.S.J. Poggiali, C.L.P. Silva, P.H.R. Pereira, R.B. Figueiredo, P.R. Cetlin, Determination of mechanical anisotropy of magnesium processed by ECAP, Journal of Materials Research and Technology 3(4) (2014) 331-337.
[45] Y. Yuan, A. Ma, X. Gou, J. Jiang, G. Arhin, D. Song, H. Liu, Effect of heat treatment and deformation temperature on the mechanical properties of ECAP processed ZK60 magnesium alloy, Materials Science and Engineering: A 677(Supplement C) (2016) 125-132.
[46] P. Minárik, J. Veselý, R. Král, J. Bohlen, J. Kubásek, M. Janeček, J. Stráská, Exceptional mechanical properties of ultra-fine grain Mg-4Y-3RE alloy processed by ECAP, Materials Science and Engineering: A 708(Supplement C) (2017) 193-198.
[47] A.M. Jorge Jr, E. Prokofiev, M.R.M. Triques, V. Roche, W.J. Botta, C.S. Kiminami, G.I. Raab, R.Z. Valiev, T.G. Langdon, Effect of cold rolling on the structure and hydrogen properties of AZ91 and AM60D magnesium alloys processed by ECAP, International Journal of Hydrogen Energy 42(34) (2017) 21822-21831.
[48] A. Nikfahm, I. Danaee, A. Ashrafi, M.R. Toroghinejad, Effect of grain size changes on corrosion behavior of copper produced by accumulative roll bonding process, Materials Research 16 (2013) 1379-1386.
[49] M. Karimi, M.R. Toroghinejad, J. Dutkiewicz, Nanostructure formation during accumulative roll bonding of commercial purity titanium, Materials Characterization 122(Supplement C) (2016) 98-103.
[50] A. Mashhadi, A. Atrian, L. Ghalandari, Mechanical and microstructural investigation of Zn/Sn multilayered composites fabricated by accumulative roll

bonding (ARB) process, Journal of Alloys and Compounds 727(Supplement C) (2017) 1314-1323.
[51] M.R. Morovvati, B.M. Dariani, The effect of annealing on the formability of aluminum 1200 after accumulative roll bonding, Journal of Manufacturing Processes 30(Supplement C) (2017) 241-254.
[52] S.M. Fatemi-Varzaneh, A. Zarei-Hanzaki, Processing of AZ31 magnesium alloy by a new noble severe plastic deformation method, Materials Science and Engineering: A 528(3) (2011) 1334-1339.
[53] S. Asqardoust, A. Zarei Hanzaki, H.R. Abedi, T. Krajnak, P. Minárik, Enhancing the strength and ductility in accumulative back extruded WE43 magnesium alloy through achieving bimodal grain size distribution and texture weakening, Materials Science and Engineering: A 698(Supplement C) (2017) 218-229.
[54] S.M. Fatemi-Varzaneh, A. Zarei-Hanzaki, Accumulative back extrusion (ABE) processing as a novel bulk deformation method, Materials Science and Engineering: A 504(1) (2009) 104-106.
[55] H. Alihosseini, G. Faraji, A.F. Dizaji, K. Dehghani, Characterization of ultra-fine grained aluminum produced by accumulative back extrusion (ABE), Materials Characterization 68(Supplement C) (2012) 14-21.
[56] N. Haghdadi, A. Zarei-Hanzaki, H.R. Abedi, D. Abou-Ras, M. Kawasaki, A.P. Zhilyaev, Evolution of microstructure and mechanical properties in a hypoeutectic Al–Si–Mg alloy processed by accumulative back extrusion, Materials Science and Engineering: A 651(Supplement C) (2016) 269-279.
[57] Y.-M. Hwang, W.M. Tsai, F.H. Tsai, I. Her, Analytical and experimental study on the spiral marks of the rolled product during three-roll planetary rolling processes, International Journal of Machine Tools and Manufacture 46(12-13) (2006) 1555-1562.
[58] Y. Li Wang, A. Molotnikov, M. Diez, R. Lapovok, H.-E. Kim, J. Tao Wang, Y. Estrin, Gradient structure produced by three roll planetary milling: Numerical simulation and microstructural observations, Materials Science and Engineering: A 639(Supplement C) (2015) 165-172.

[59] T.S. Mahmoud, Effect of friction stir processing on electrical conductivity and corrosion resistance of AA6063-T6 Al alloy, Proceedings of the Institution of Mechanical Engineers, Part C: Journal of Mechanical Engineering Science 222(7) (2008) 1117-1123.
[60] Y.H. Jang, S.S. Kim, C.D. Yim, C.G. Lee, S.J. Kim, Corrosion behaviour of friction stir welded AZ31B Mg in 3·5%NaCl solution, Corrosion Engineering, Science and Technology 42(2) (2013) 119-122.
[61] G. Rambabu, D. Balaji Naik, C.H. Venkata Rao, K. Srinivasa Rao, G. Madhusudan Reddy, Optimization of friction stir welding parameters for improved corrosion resistance of AA2219 aluminum alloy joints, Defence Technology 11(4) (2015) 330-337.
[62] B. Ratna Sunil, G. Pradeep Kumar Reddy, Corrosion behavior of friction stir welded AZ31B Mg alloy - Al6063 alloy joint, Cogent Engineering 3(1) (2016) 1145565.
[63] J.H. Gao, S.K. Guan, Z.W. Ren, Y.F. Sun, S.J. Zhu, B. Wang, Homogeneous corrosion of high pressure torsion treated Mg–Zn–Ca alloy in simulated body fluid, Materials Letters 65(4) (2011) 691-693.
[64] Y. Ivanisenko, R. Kulagin, V. Fedorov, A. Mazilkin, T. Scherer, B. Baretzky, H. Hahn, High Pressure Torsion Extrusion as a new severe plastic deformation process, Materials Science and Engineering: A 664(Supplement C) (2016) 247-256.
[65] X. Wang, M. Nie, C.T. Wang, S.C. Wang, N. Gao, Microhardness and corrosion properties of hypoeutectic Al–7Si alloy processed by high-pressure torsion, Materials & Design 83(Supplement C) (2015) 193-202.
[66] A. Hohenwarter, Incremental high pressure torsion as a novel severe plastic deformation process: Processing features and application to copper, Materials Science and Engineering: A 626(Supplement C) (2015) 80-85.
[67] X. Yang, H. Miura, T. Sakai, Structural development at severely high strain in AZ31 magnesium alloy processed by cold forging and subsequent annealing, Materials & Design 44 (2013) 573-579.

[68] H. Miura, G. Yu, X. Yang, Multi-directional forging of AZ61Mg alloy under decreasing temperature conditions and improvement of its mechanical properties, Materials Science and Engineering: A 528(22-23) (2011) 6981-6992.
[69] J. Li, J. Liu, Z. Cui, Microstructures and mechanical properties of AZ61 magnesium alloy after isothermal multidirectional forging with increasing strain rate, Materials Science and Engineering: A 643(Supplement C) (2015) 32-36.
[70] M.R. Jandaghi, H. Pouraliakbar, M.K.G. Shiran, G. Khalaj, M. Shirazi, On the effect of non-isothermal annealing and multi-directional forging on the microstructural evolutions and correlated mechanical and electrical characteristics of hot-deformed Al-Mg alloy, Materials Science and Engineering: A 657(Supplement C) (2016) 431-440.
[71] K.B. Nie, K.K. Deng, X.J. Wang, F.J. Xu, K. Wu, M.Y. Zheng, Multidirectional forging of AZ91 magnesium alloy and its effects on microstructures and mechanical properties, Materials Science and Engineering: A 624 (2015) 157-168.
[72] C. Cai, S. LingHui, D. XingHao, W. BaoLin, Enhanced mechanical property of AZ31B magnesium alloy processed by multi-directional forging method, Materials Characterization 131 (2017) 72-77.
[73] B. Wang, C. Liu, Y. Gao, S. Jiang, Z. Chen, Z. Luo, Microstructure evolution and mechanical properties of Mg-Gd-Y-Ag-Zr alloy fabricated by multidirectional forging and ageing treatment, Materials Science and Engineering: A 702 (2017) 22-28.
[74] H. Miura, T. Maruoka, J.J. Jonas, Effect of ageing on microstructure and mechanical properties of a multi-directionally forged Mg–6Al–1Zn alloy, Materials Science and Engineering: A 563 (2013) 53-59.
[75] Y. Uematsu, T. Kakiuchi, H. Miura, T. Nozaki, Effect of Grain Size on Fatigue Behavior in AZ61 Mg Alloys Fabricated by MDFing, Materials Transactions 57(9) (2016) 1454-1461.
[76] X. Liu, L. Xiao, C. Wei, X. Xu, M. Luo, W. Yan, Effect of multi-directional forging and annealing on abrasive wear behavior in a medium carbon low alloy steel, Tribology International 119 (2018) 608-613.

[77] R. Zhang, D. Wang, S. Yuan, Effect of multi-directional forging on the microstructure and mechanical properties of TiBw/TA15 composite with network architecture, Materials & Design 134(Supplement C) (2017) 250-258.
[78] A. Prasad, P.J. Uggowitzer, Z. Shi, A. Atrens, Production of High Purity Magnesium Alloys by Melt Purification with Zr, Advanced Engineering Materials 14(7) (2012) 477-490.
[79] A. Atrens, G.-L. Song, F. Cao, Z. Shi, P.K. Bowen, Advances in Mg corrosion and research suggestions, Journal of Magnesium and Alloys 1(3) (2013) 177-200.
[80] L. Fairman, H.J. Bray, Transgranular see in Mg-Al alloys, Corrosion Science 11(7) (1971) 533-541.
[81] A. Samaniego, K. Gusieva, I. Llorente, S. Feliu, N. Birbilis, Exploring the possibility of protective surface oxides upon Mg alloy AZ31 via lutetium additions, Corrosion Science 89 (2014) 101-110.
[82] K. Hagihara, M. Okubo, M. Yamasaki, T. Nakano, Crystal-orientation-dependent corrosion behaviour of single crystals of a pure Mg and Mg-Al and Mg-Cu solid solutions, Corrosion Science 109 (2016) 68-85.
[83] N. Birbilis, G. Williams, K. Gusieva, A. Samaniego, M.A. Gibson, H.N. McMurray, Poisoning the corrosion of magnesium, Electrochemistry Communications 34 (2013) 295-298.
[84] G. Song, A. Atrens, D.S. John, X. Wu, J. Nairn, The anodic dissolution of magnesium in chloride and sulphate solutions, Corrosion Science 39(10) (1997) 1981-2004.
[85] F. Cao, Z. Shi, J. Hofstetter, P.J. Uggowitzer, G. Song, M. Liu, A. Atrens, Corrosion of ultra-high-purity Mg in 3.5% NaCl solution saturated with Mg(OH)2, Corrosion Science 75 (2013) 78-99.
[86] O.I. Velikokhatnyi, P.N. Kumta, First-principles studies on alloying and simplified thermodynamic aqueous chemical stability of calcium-, zinc-, aluminum-, yttrium- and iron-doped magnesium alloys, Acta Biomater 6(5) (2010) 1698-704.
[87] K.D. Ralston, N. Birbilis, Effect of Grain Size on Corrosion: A Review, CORROSION 66(7) (2010) 075005-075005-13.

[88] R. Gupta, K.P. Sanjay, S. Srivastava, Assessmen of various properties evolved during grain refinement through multi-directional forging, 46 (2016) 70-85.
[89] K. Venkateswarlu, M. Sandhyarani, T.A. Nellaippan, N. Rameshbabu, Estimation of Crystallite Size, Lattice Strain and Dislocation Density of Nanocrystalline Carbonate Substituted Hydroxyapatite by X-ray Peak Variance Analysis, Procedia Materials Science 5 (2014) 212-221.
[90] N. Birbilis, K.D. Ralston, S. Virtanen, H.L. Fraser, C.H.J. Davies, Grain character influences on corrosion of ECAPed pure magnesium, Corrosion Engineering, Science and Technology 45(3) (2010) 224-230.
[91] N.N. Aung, W. Zhou, Effect of grain size and twins on corrosion behaviour of AZ31B magnesium alloy, Corrosion Science 52(2) (2010) 589-594.
[92] D. Orlov, K.D. Ralston, N. Birbilis, Y. Estrin, Enhanced corrosion resistance of Mg alloy ZK60 after processing by integrated extrusion and equal channel angular pressing, Acta Materialia 59(15) (2011) 6176-6186.
[93] K.D. Ralston, N. Birbilis, C.H.J. Davies, Revealing the relationship between grain size and corrosion rate of metals, Scripta Materialia 63(12) (2010) 1201-1204.
[94] Y. Liu, D. Liu, C. You, M. Chen, Effects of grain size on the corrosion resistance of pure magnesium by cooling rate-controlled solidification, Frontiers of Materials Science 9(3) (2015) 247-253.
[95] L. Jinlong, L. Hongyun, The effects of cold rolling temperature on corrosion resistance of pure iron, Applied Surface Science 317 (2014) 125-130.
[96] D. Song, A.-b. Ma, J.-h. Jiang, P.-h. Lin, D.-h. Yang, Corrosion behavior of ultra-fine grained industrial pure Al fabricated by ECAP, Transactions of Nonferrous Metals Society of China 19(5) (2009) 1065-1070.
[97] V. Afshari, C. Dehghanian, Effects of grain size on the electrochemical corrosion behaviour of electrodeposited nanocrystalline Fe coatings in alkaline solution, Corrosion Science 51(8) (2009) 1844-1849.
[98] I. Roy, H. Yang, L. Dinh, I. Lund, J. Earthman, F. Mohamed, Possible origin of superior corrosion resistance for electrodeposited nanocrystalline Ni, Scripta Materialia 59(3) (2008) 305-308.

[99] S.G. Wang, C.B. Shen, K. Long, F. Zhang, F.H. Wang, Z.D. Zhang, The electrochemical corrosion of bulk nanocrystalline ingot iron in acidic sulfate solution, Journal of Physical Chemistry B 110 (2006) 377-382.
[100] C. op't Hoog, N. Birbilis, Y. Estrin, Corrosion of Pure Mg as a Function of Grain Size and Processing Route, Advanced Engineering Materials 10(6) (2008) 579-582.
[101] T. Zheng, Y. Hu, S. Yang, Effect of grain size on the electrochemical behavior of pure magnesium anode, Journal of Magnesium and Alloys (2017).
[102] G.-L. Song, R. Mishra, Z. Xu, Crystallographic orientation and electrochemical activity of AZ31 Mg alloy, Electrochemistry Communications 12(8) (2010) 1009-1012.
[103] D. Song, A. Ma, J. Jiang, P. Lin, D. Yang, J. Fan, Corrosion behavior of equal-channel-angular-pressed pure magnesium in NaCl aqueous solution, Corrosion Science 52(2) (2010) 481-490.
[104] P.-p. Wu, F.-j. Xu, K.-k. Deng, F.-y. Han, Z.-z. Zhang, R. Gao, Effect of extrusion on corrosion properties of Mg-2Ca-χAl (χ = 0, 2, 3, 5) alloys, Corrosion Science 127 (2017) 280-290.
[105] K.S. Shin, M.Z. Bian, N.D. Nam, Effects of Crystallographic Orientation on Corrosion Behavior of Magnesium Single Crystals, Jom 64(6) (2012) 664-670.
[106] R. Xin, Y. Luo, A. Zuo, J. Gao, Q. Liu, Texture effect on corrosion behavior of AZ31 Mg alloy in simulated physiological environment, Materials Letters 72 (2012) 1-4.
[107] G.-L. Song, The Effect of Texture on the Corrosion Behavior of AZ31 Mg Alloy, Jom 64(6) (2012) 671-679.
[108] S. Bahl, S. Suwas, K. Chatterjee, The control of crystallographic texture in the use of magnesium as a resorbable biomaterial, RSC Adv. 4(99) (2014) 55677-55684.
[109] Q. Jiang, X. Ma, K. Zhang, Y. Li, X. Li, Y. Li, M. Ma, B. Hou, Anisotropy of the crystallographic orientation and corrosion performance of high-strength AZ80 Mg alloy, Journal of Magnesium and Alloys 3(4) (2015) 309-314.

[110] S. Pawar, T.J.A. Slater, T.L. Burnett, X. Zhou, G.M. Scamans, Z. Fan, G.E. Thompson, P.J. Withers, Crystallographic effects on the corrosion of twin roll cast AZ31 Mg alloy sheet, Acta Materialia 133 (2017) 90-99.
[111] Y.-C. Zhao, G.-S. Huang, G.-G. Wang, T.-Z. Han, F.-S. Pan, Influence of Grain Orientation on the Corrosion Behavior of Rolled AZ31 Magnesium Alloy, Acta Metallurgica Sinica (English Letters) 28(11) (2015) 1387-1393.
[112] Z. Pu, G.L. Song, S. Yang, J.C. Outeiro, O.W. Dillon, D.A. Puleo, I.S. Jawahir, Grain refined and basal textured surface produced by burnishing for improved corrosion performance of AZ31B Mg alloy, Corrosion Science 57 (2012) 192-201.
[113] C.D. Lee, C.S. Kang, K.S. Shin, Effect of Galvanic Corrosion between Precipitate and Matrix on Corrosion Behav of As-Cast Mg-Al Alloys, Metals and Materials 6 (2000) 351-358.
[114] W. Melitz, J. Shen, A.C. Kummel, S. Lee, Kelvin probe force microscopy and its application, Surface Science Reports 66(1) (2011) 1-27.
[115] P.R. Cha, H.S. Han, G.F. Yang, Y.C. Kim, K.H. Hong, S.C. Lee, J.Y. Jung, J.P. Ahn, Y.Y. Kim, S.Y. Cho, J.Y. Byun, K.S. Lee, S.J. Yang, H.K. Seok, Biodegradability engineering of biodegradable Mg alloys: tailoring the electrochemical properties and microstructure of constituent phases, Sci Rep 3 (2013) 2367.
[116] I. Apachitei, L.E. Fratila-Apachitei, J. Duszczyk, Microgalvanic activity of an Mg–Al–Ca-based alloy studied by scanning Kelvin probe force microscopy, Scripta Materialia 57(11) (2007) 1012-1015.
[117] A.E. Coy, F. Viejo, P. Skeldon, G.E. Thompson, Susceptibility of rare-earth-magnesium alloys to micro-galvanic corrosion, Corrosion Science 52(12) (2010) 3896-3906.
[118] R. Arrabal, A. Pardo, M.C. Merino, M. Mohedano, P. Casajús, K. Paucar, G. Garcés, Effect of Nd on the corrosion behaviour of AM50 and AZ91D magnesium alloys in 3.5wt.% NaCl solution, Corrosion Science 55 (2012) 301-312.

[119] G. Ben-Hamu, D. Eliezer, C.E. Cross, T. Böllinghaus, The relation between microstructure and corrosion behavior of GTA welded AZ31B magnesium sheet, Materials Science and Engineering: A 452-453 (2007) 210-218.
[120] M.C. Merino, A. Pardo, R. Arrabal, S. Merino, P. Casajús, M. Mohedano, Influence of chloride ion concentration and temperature on the corrosion of Mg–Al alloys in salt fog, Corrosion Science 52(5) (2010) 1696-1704.
[121] R. Arrabal, A. Pardo, M.C. Merino, K. Paucar, M. Mohedano, P. Casajús, G. Garcés, Influence of Gd on the Corrosion Behavior of AM50 and AZ91D Magnesium Alloys, CORROSION 68(5) (2012) 398-410.
[122] M. Mohedano, R. Arrabal, Á. Pardo, M.C. Merino, K. Paucar, P. Casajús, E. Matykina, Salt spray corrosion behaviour of new Mg–Al alloys containing Nd or Gd, Corrosion Engineering, Science and Technology 48(3) (2013) 183-193.
[123] R. Arrabal, B. Mingo, A. Pardo, E. Matykina, M. Mohedano, M.C. Merino, A. Rivas, A. Maroto, Role of alloyed Nd in the microstructure and atmospheric corrosion of as-cast magnesium alloy AZ91, Corrosion Science 97 (2015) 38-48.
[124] M.F. Hurley, C.M. Efaw, P.H. Davis, J.R. Croteau, E. Graugnard, N. Birbilis, Volta Potentials Measured by Scanning Kelvin Probe Force Microscopy as Relevant to Corrosion of Magnesium Alloys, Corrosion 71(2) (2015) 160-170.
[125] R. Arrabal, E. Matykina, A. Pardo, M.C. Merino, K. Paucar, M. Mohedano, P. Casajús, Corrosion behaviour of AZ91D and AM50 magnesium alloys with Nd and Gd additions in humid environments, Corrosion Science 55 (2012) 351-362.
[126] J. Liu, Y. Song, J. Chen, P. Chen, D. Shan, E.-H. Han, The Special Role of Anodic Second Phases in the Micro-galvanic Corrosion of EW75 Mg Alloy, Electrochimica Acta 189 (2016) 190-195.
[127] W. Liu, F. Cao, A. Chen, L. Chang, J. Zhang, C. Cao, Corrosion behaviour of AM60 magnesium alloys containing Ce or La under thin electrolyte layers. Part 1: Microstructural characterization and electrochemical behaviour, Corrosion Science 52(2) (2010) 627-638.
[128] S.-M. Baek, J.S. Kang, H.-J. Shin, C.D. Yim, B.S. You, H.-Y. Ha, S.S. Park, Role of alloyed Y in improving the corrosion resistance of extruded Mg–Al–Ca-based alloy, Corrosion Science 118 (2017) 227-232.

[129] G. Williams, K. Gusieva, N. Birbilis, Localized Corrosion of Binary Mg-Nd Alloys in Chloride-Containing Electrolyte Using a Scanning Vibrating Electrode Technique, CORROSION 68(6) (2012) 489-498.
[130] F. Andreatta, I. Apachitei, A.A. Kodentsov, J. Dzwonczyk, J. Duszczyk, Volta potential of second phase particles in extruded AZ80 magnesium alloy, Electrochimica Acta 51(17) (2006) 3551-3557.
[131] P. Bindu, S. Thomas, Estimation of lattice strain in ZnO nanoparticles: X-ray peak profile analysis, Journal of Theoretical and Applied Physics 8(4) (2014) 123-134.
[132] S. Arthanari, J.C. Jang, K.S. Shin, Corrosion Behavior of High Pressure Die Cast Al-Ni and Al-Ni-Ca Alloys, Corrosion Science and Technology 3 (2017) 100-108.
[133] Z. Shi, F. Cao, G.-L. Song, M. Liu, A. Atrens, Corrosion behaviour in salt spray and in 3.5% NaCl solution saturated with Mg(OH)2 of as-cast and solution heat-treated binary Mg–RE alloys: RE=Ce, La, Nd, Y, Gd, Corrosion Science 76 (2013) 98-118.
[134] F. Cao, Corrosion and Stress Corrosion Cracking of Magnesium Alloys, University of Queensland PhD Thesis (2015).
[135] L.B. Tong, Q.X. Zhang, Z.H. Jiang, J.B. Zhang, J. Meng, L.R. Cheng, H.J. Zhang, Microstructures, mechanical properties and corrosion resistances of extruded Mg-Zn-Ca-xCe/La alloys, J Mech Behav Biomed Mater 62 (2016) 57-70.
[136] G. Bi, Y. Li, S. Zang, J. Zhang, Y. Ma, Y. Hao, Microstructure, mechanical and corrosion properties of Mg–2Dy–xZn (x=0, 0.1, 0.5 and 1 at.%) alloys, Journal of Magnesium and Alloys 2(1) (2014) 64-71.
[137] S.-M. Baek, H.J. Kim, H.Y. Jeong, S.-D. Sohn, H.-J. Shin, K.-J. Choi, K.-S. Lee, J.G. Lee, C.D. Yim, B.S. You, H.-Y. Ha, S.S. Park, Effect of alloyed Ca on the microstructure and corrosion properties of extruded AZ61 Mg alloy, Corrosion Science 112 (2016) 44-53.
[138] S. Gollapudi, Grain size distribution effects on the corrosion behaviour of materials, Corrosion Science 62 (2012) 90-94.

[139] H.S. Kim, G.H. Kim, H. Kim, W.J. Kim, Enhanced corrosion resistance of high strength Mg–3Al–1Zn alloy sheets with ultrafine grains in a phosphate-buffered saline solution, Corrosion Science 74 (2013) 139-148.
[140] H.S. Kim, W.J. Kim, Enhanced corrosion resistance of ultrafine-grained AZ61 alloy containing very fine particles of Mg17Al12 phase, Corrosion Science 75 (2013) 228-238.
[141] G. Han, J.-Y. Lee, Y.-C. Kim, J.H. Park, D.-I. Kim, H.-S. Han, S.-J. Yang, H.-K. Seok, Preferred crystallographic pitting corrosion of pure magnesium in Hanks' solution, Corrosion Science 63 (2012) 316-322.
[142] D. Ahmadkhaniha, A. Jarvenpaa, M. Jaskari, M.H. Sohi, A. Zarei-Hanzaki, M. Fedel, F. Deflorian, L.P. Karjalainen, Microstructural modification of pure Mg for improving mechanical and biocorrosion properties, J Mech Behav Biomed Mater 61 (2016) 360-370.
[143] D. Ahmadkhaniha, M. Fedel, M. Heydarzadeh Sohi, F. Deflorian, Corrosion behavior of severely plastic deformed magnesium based alloys: A review, Surface Engineering and Applied Electrochemistry 53(5) (2017) 439-448.
[144] A. Balyanov, Corrosion resistance of ultra fine-grained Ti, Scripta Materialia 51(3) (2004) 225-229.
[145] R. Mishra, R. Balasubramaniam, Effect of nanocrystalline grain size on the electrochemical and corrosion behavior of nickel, Corrosion Science 46(12) (2004) 3019-3029.
[146] G.R. Argade, S.K. Panigrahi, R.S. Mishra, Effects of grain size on the corrosion resistance of wrought magnesium alloys containing neodymium, Corrosion Science 58 (2012) 145-151.
[147] J. Liao, M. Hotta, N. Yamamoto, Corrosion behavior of fine-grained AZ31B magnesium alloy, Corrosion Science 61 (2012) 208-214.
[148] H.S. Kim, W.J. Kim, Annealing effects on the corrosion resistance of ultrafine-grained pure titanium, Corrosion Science 89 (2014) 331-337.

7 Supplementary Information

7.1 Texture and dislocation density analysis

7.1.1 Extruded and screw rolled ZAXM4211 alloy

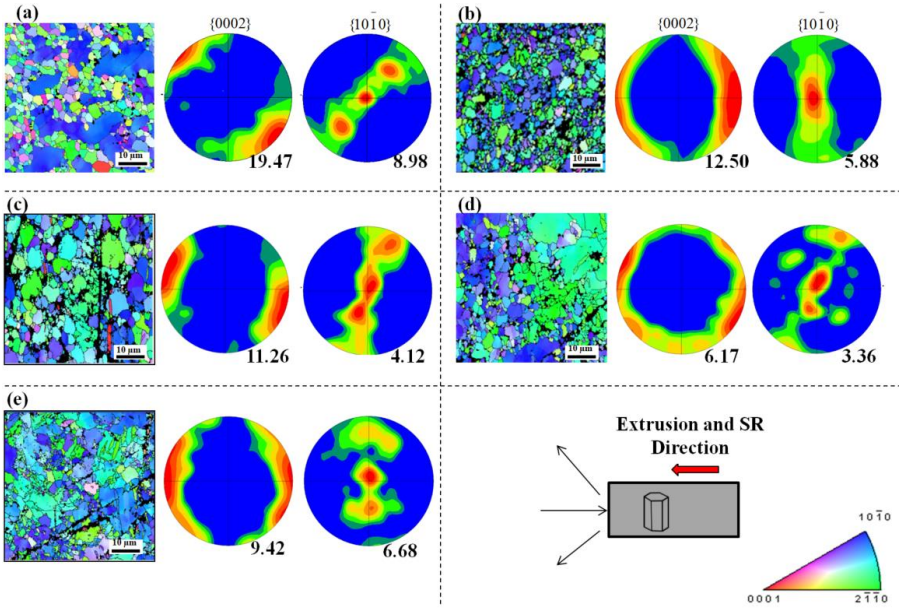

Fig. S1. Texture analysis of the ZAXM4211 alloy processed through extrusion and screw rolling at various temperatures (a) extrusion, (b) SR220, (c) SR260, (d) SR300 and (e) SR340.

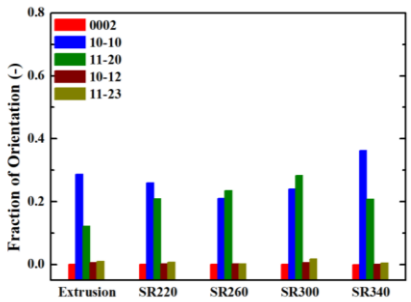

	(0002)	(10-10)	(11-20)	(10-12)	(11-23)	Rem.
Extrusion	0.001	0.287	0.122	0.007	0.010	0.570
SR220	0.001	0.260	0.209	0.003	0.008	0.518
SR260	0.001	0.210	0.235	0.003	0.003	0.547
SR300	0.001	0.240	0.284	0.007	0.018	0.449
SR340	0.000	0.363	0.208	0.001	0.004	0.423

Fig. S2. The fraction of various orientations in extruded and SRed ZAXM4211 alloy.

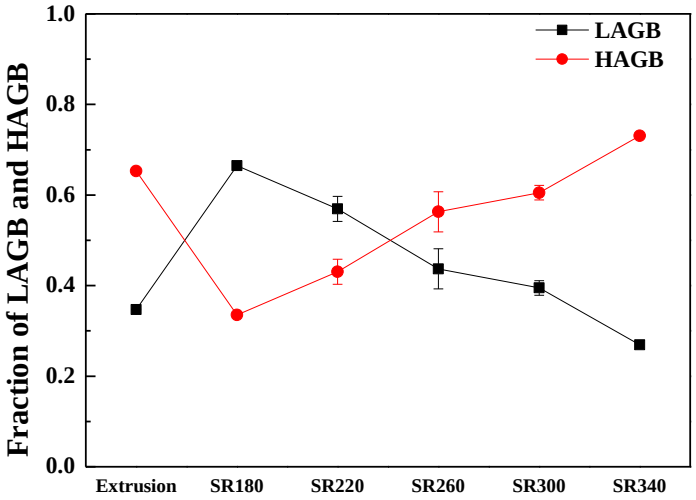

Fig. S3. Texture analysis of the ZAXM4211 alloy processed through Extrusion and screw rolling at various temperatures (a) extrusion, (b) SR220, (c) SR260, (d) SR300 and (e) SR340.

Table S1. XRD analysis of extruded and screw rolled ZAXM4211 alloy for measuring dislocation density and lattice strain of ($\mathbf{10\bar{1}0}$) peak.

Sample	FWHM (^{o})	Lattice Strain	Crystallite Size ($\dot{A}$)	Dislocation Density (m^{-2})
Annealed	0.080	-	-	-
Extrusion	0.140	0.173	1378	5.27E+13
SR180	0.155	0.169	1381	5.24E+13
SR220	0.145	0.178	1275	6.15E+13
SR260	0.140	0.173	1378	5.27E+13
SR300	0.132	0.151	1657	3.64E+13
SR340	0.111	0.111	2763	1.31E+13

7.1.2 Extrusion and MDFed ZAXM4211 alloy

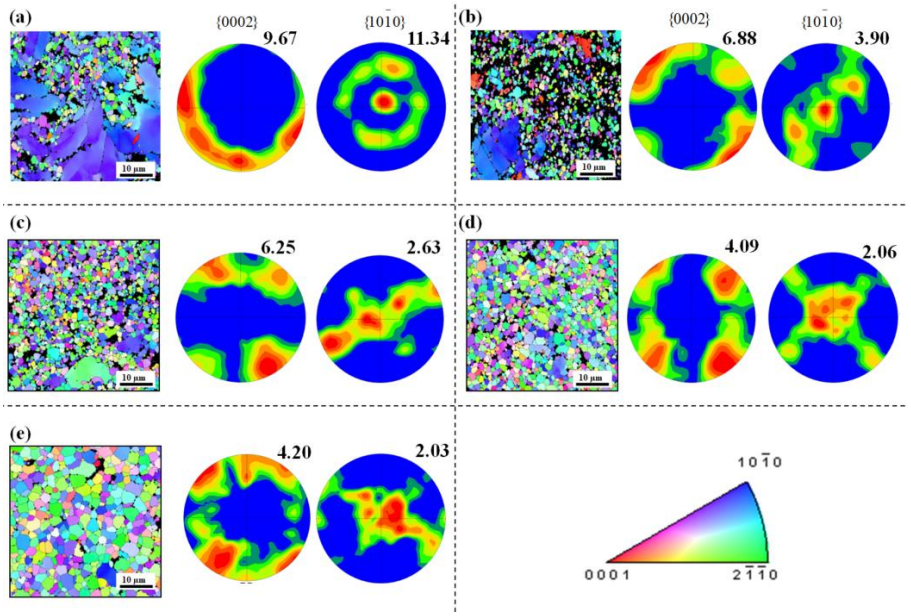

Fig. S4. Texture analysis of the ZAXM4211 alloy manufactured through extrusion and MDF at various temperatures (a) extrusion, (b) MDF180, (c) MDF220, (d) MDF260 and (e) MDF300.

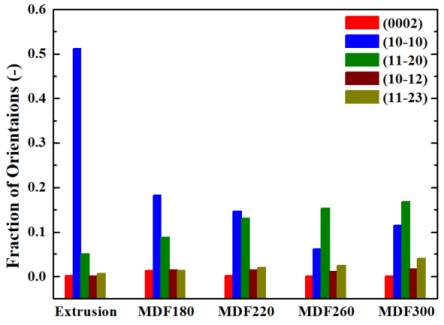

	(0002)	(10-10)	(11-20)	(10-12)	(11-23)	Rem.
Extrusion	0.003	0.512	0.051	0.002	0.006	0.43
MDF180	0.014	0.183	0.088	0.015	0.014	0.69
MDF220	0.002	0.147	0.131	0.015	0.020	0.69
MDF260	0.003	0.062	0.154	0.012	0.025	0.74
MDF300	0.001	0.115	0.167	0.018	0.042	0.66

Fig. S5. The fraction of various orientations in extruded and MDFed ZAXM4211 alloy.

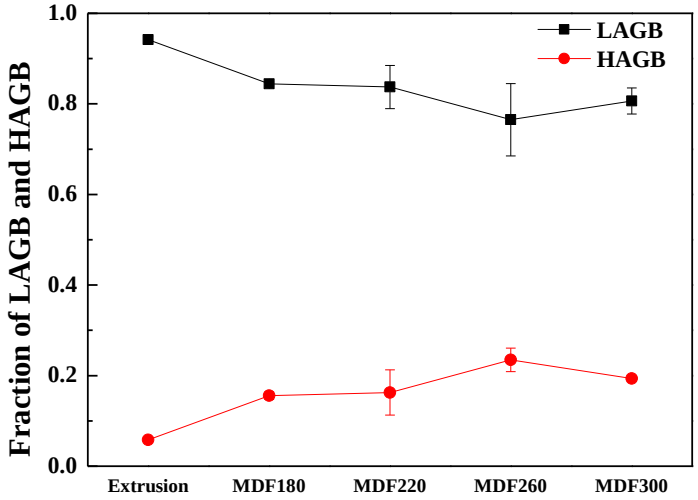

Fig. S6. The fraction of low angle and high angle grain boundaries of extruded and MDFed ZAXM4211 alloy.

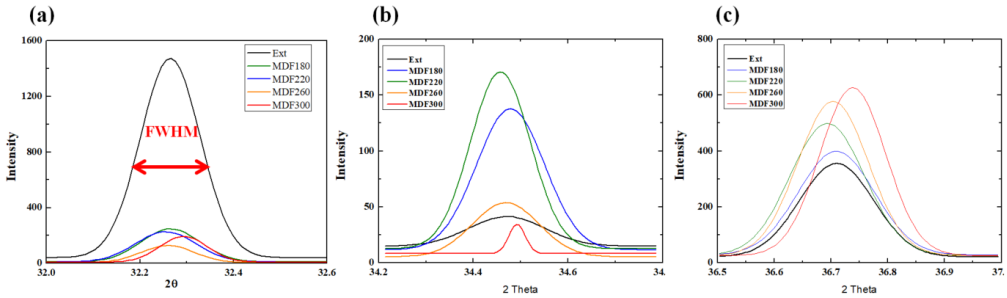

Fig. S7. XRD analysis of ZAXM4211 alloy for measuring dislocation density and lattice strain: (a) $(10\bar{1}0)$, (b) (0002) and (c) $(10\bar{1}2)$ planes and (d) FWHM of $(10\bar{1}0)$ planes, lattice strain and dislocation density.

Table S2. XRD analysis of extruded and MDFed ZAXM4211 alloy for measuring dislocation density and lattice strain of $(10\bar{1}0)$ peak**.**

Sample	FWHM (^{o})	Lattice Strain	Crystallite Size ($\dot{A}$)	Dislocation Density (m^{-2})
Annealed	0.066	-	-	-
Extrusion	0.142	0.194	1008	9.84E+13
MDF180	0.144	0.198	984	1.03E+14
MDF220	0.093	0.107	2506	1.59E+13
MDF260	0.077	0.073	4846	4.26E+12
MDF300	0.068	0.050	9999	1.00E+12

7.1.3 Extrusion and MDFed XM11 alloy

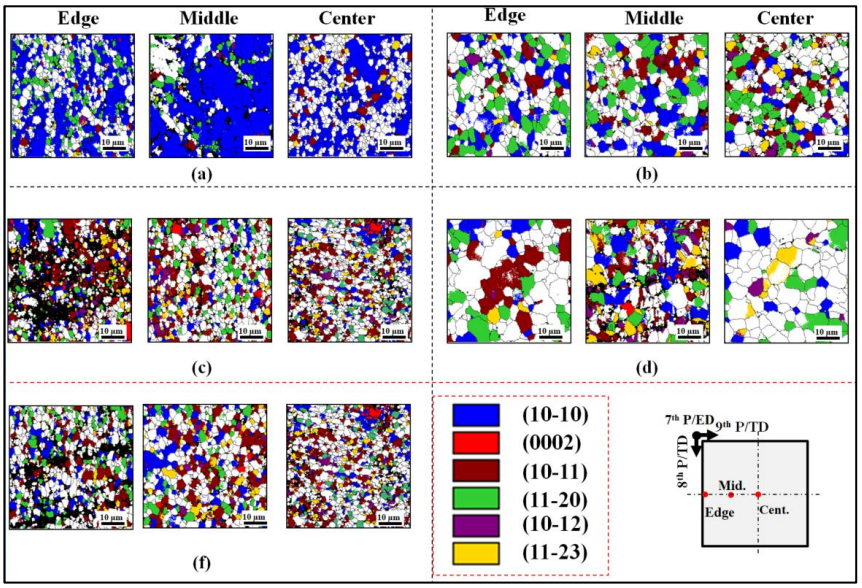

Fig. S8. Texture analysis of the XM11 alloy manufactured through extrusion and MDF at various temperatures: (a) extrusion, (b) MDF220, (c) MDF260, (c) MDF300, and (f) MDF340.

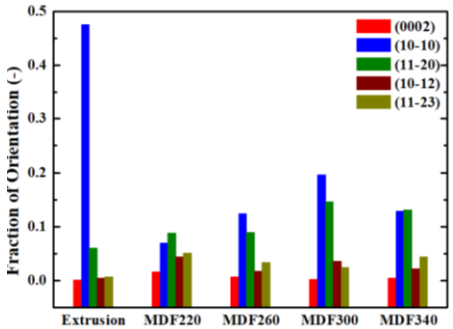

	(0002)	(10-10)	(11-20)	(10-12)	(11-23)	Rem.
Extrusion	0.001	0.475	0.061	0.004	0.007	0.452
MDF220	0.016	0.089	0.088	0.044	0.051	0.731
MDF260	0.006	0.124	0.090	0.017	0.034	0.729
MDF300	0.002	0.195	0.146	0.036	0.024	0.597
MDF340	0.004	0.129	0.131	0.022	0.044	0.670

Fig. S9. The fraction of different orientations in XM11 alloy.

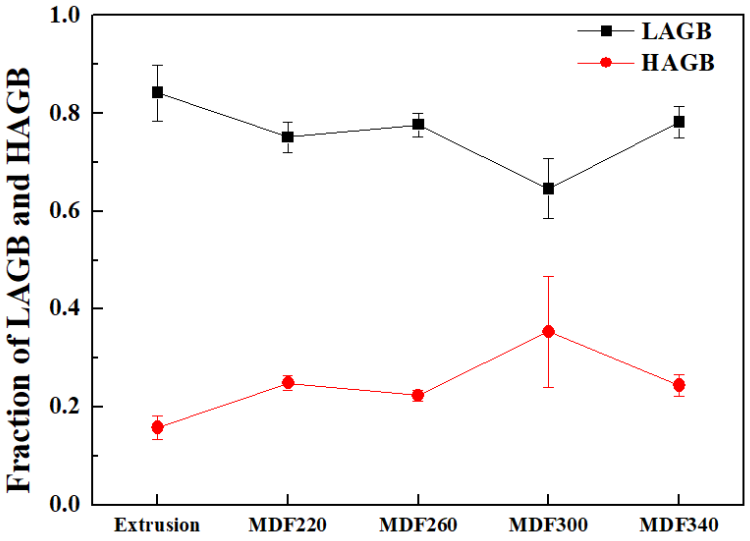

Fig S10. Texture analysis of the ZAXM4211 alloy processed through extrusion and screw rolling at various temperatures (a) extrusion, (b) SR220, (c) SR260, (d) SR300 and (e) SR340.

Table S3. XRD analysis of extruded and screw rolled XM11 alloy for measuring dislocation density and lattice strain of $(10\bar{1}0)$ peak**.**

Sample	**FWHM (^{o})**	**Lattice Strain (%)**	**Crystallite Size ($\dot{A}$)**	**Dislocation Density (m^{-2})**
Annealed	0.060	-	-	-
Extrusion	0.110	0.139	1654	$3.65\times10^{+13}$
MDF220	0.085	0.089	3308	$9.14\times10^{+12}$
MDF260	0.087	0.095	3063	$1.07\times10^{+13}$
MDF300	0.068	0.055	8268	$1.46\times10^{+12}$
MDF340	0.072	0.06	6891	$2.11\times10^{+12}$

7.2 Literature review on the effect of grain size on corrosion rate

Table S4. The literature review on the effect of grain size on corrosion rate

D (µm)	Process	Material	Solution	D decreases ➔ CR ?	How to change D	The Mechanism	Ref.
6000– 30	Hot Extrusion (250°C)	Pure Mg	Hank	Decreases	Extrusion of Cast Material	Preferred crystallographic pitting (PCP) was initiated by Fe precipitates in pure Mg and was propagated along a (0 0 0 1) plane in a grain of the material. The key factor for acceleration of PCP corrosion was the concentration of Fe impurities and large grain size. Refining the grain size of pure Mg by hot extrusion also reduced PCP propagation, indicating that the grain boundary acts as a barrier to pit propagation.	[141]
30-20	Extrusion	Pure Mg	3.5 wt.% NaCl	Decreases	Temp. (180, 220, 250°C)	The R_f of the pure magnesium sample extruded at 250 °C is about 5.17 $\Omega.cm^2$, and the result indicates that the magnesium hydroxide film deposited on the surface of the pure magnesium sample obtained at 250 °C is thinner, so that the electrolyte can penetrate easier and promote the continuous dissolution of the pure magnesium sample at the open circuit potential. The EIS results are consistent with the previous analysis.	[101]
1000-200	Direction. Solidif.	Pure Mg	SBF	Decreases	Solidification Rate	Decreasing the corrosion rate is attributed to refined grains that can produce more uniform and dense film on the surface of pure magnesium sample.	[94]
-	Severe Rolling	Pure Fe	Na_2SO_4	Decreases	Severe Rolling	The main reason for enhanced corrosion properties of BNII (Bulk Nano Crystallined Iron Ingot) in comparison with CPII (Poly Crystalline Iron Ingot) may be related to the difference between their microstructures. (1) The preferential orientation ⟨111⟩ (110) was dominant, and disordered orientation disappeared for BNII. There were a smaller number of dislocations in the rolled surface for BNII than that for CPII, resulting in the decrease of corrosion rates for both anode and cathode.	[99]
1000-11.5	FSP	Pure Mg	SBF	Decreases	Num. of Passes	Increasing the intensity of basal planes by increasing the number of passes	[142, 143]
1500-200	ECAP from Cast	Pure Mg	3.5 wt.% NaCl	Increases	Num. of Passes	The strain-induced grain refinement with more crystalline defects increased corrosion rate of pure Mg, resulting in more and deeper pits after in-situ corrosion, higher mass-loss rate immersed in NaCl solution, larger i_{corr} values in polarization curves and lower fitted R_t values in EIS plots.	[103]
100-2	ECAP	Pure Mg	0.1 M NaCl	Decreases	Num. of Passes	A hypothesis put forward to rationalize decreasing the corrosion rate of grain refined Mg was that the increased number density, coupled with high misorientation angle of grain boundaries that formed as a result of continued ECAP processing help promote a more coherent oxide.	[90]

7.0-0.3	ECAP and Anneal	Pure Ti	HCL-H_2SO_4 (1, 3 and 5M)	Decrease	ECAPed Material was Annealed at 800 ^oC	The decreased corrosion rate of UFG Ti is believed to result from rapid passivation of UFG Ti and the impurity segregation to grain boundaries in CG Ti. Johansen et al. studied Ti oxidation at low current densities and found that Ti oxide film formed on the surfaces of deformed Ti samples (34% plastic strain) at a greater rate than on the surfaces of annealed samples. Tomashov and Ivanov also found lower passivation current, i_{pass}, for deformed Ti (80% strain) than for annealed Ti in H_2SO_4 and HCl. It is believed that the passivation first started on surface crystalline lattice defects of Ti . The UFG Ti has high density of grain boundaries and dislocations inside grains. If the passive films on the sample surfaces were nucleated at surface crystalline defects, as asserted in a previous work, the UFG Ti would have had a high density of nucleation sites for passive films, which leads to high fraction of passive layers and low corrosion rates.	[144]
250-35	Heat Treatment (from As Cast)	AZ31B	3.5 wt.% NaCl	Decrease (Due to Grain Refinement) - Increase(Due to Increase in Twins)	Temp. Change	The results suggest that the effect of grain size was less pronounced in the corrosion of the twinned microstructure (As Rolled and HT200). A higher density of dislocation and twins probably lead to high hardness values and high anodic dissolution. The acceleration of anodic metal dissolution is caused by a local reduction of equilibrium potential in the vicinity of dislocations. The grain boundary acts as a physical corrosion barrier. Small grain size creates more grain boundaries, as a consequence, the rate of corrosion in small-grained microstructure slowed down compared with coarse-grained microstructure. In HT 300 sample, a high density of twins was eliminated, but the grain size did not change significantly, resulting in relatively lower corrosion rate. Due to the less physical barrier, coarse-grained microstructure led to an increase in the corrosion rate of the HT 500 sample	[91]
28-8	Electro-deposition	Pure Fe	H_2SO_4	Decreases		-	[145]
70-0.65	FSP	Mg-Y-RE	3.5 wt.% NaCl	Decreases	HT for Grain Enlargement, and FSP for Refinement	In the ultrafine grained regime, the very high fraction of grain boundaries in the microstructure is likely to reduce corrosion rates in two ways: (1) accelerating the passivation kinetics, and (2) reduce the intensity of galvanic couple between grain interior and grain boundary. Therefore, the UFG microstructure will lead to formation of closely spaced electrochemical batteries of anodic–cathodic regions. Thus the difference between the rates of anodic and cathodic reactions are expected to alter significantly, which leads to more uniform attack and lower corrosion rates.	[146]
11-1.4	Hot Extrusion	AZ31B	0.1M NaCl	Decreases	Process Time	Grain refinement may help to relieve the stress on surface film due to mismatch between magnesium oxide (MgO) and underlaying Mg metal substrate, by producing porosity through vacancy supply via grain boundaries, thus increase the passivity of surface film. This would improve the stability and/or passivity of the surface film of fine-grained magnesium alloys.	[147]

-	ECAP	AZ91D	3.5 wt.% NaCl	Increase	Num. of Passes	The higher corrosion rate of ECAPed AZ91D alloy is closely related to the severe deformed UFG α-phase matrix and the refined β-phase. The strains-induced mass crystalline defects, including energetic high-angle grain boundaries and dislocations, offer the α-phase matrix more corrosion activation and increase the corrosion rate of α-phase matrix. The change from net-like β-phase into isolated and uniformly distributed fine particles bereaves its barrier function to the corrosion propagation in the α-phase matrix. The interaction of two factors also caused the corrosion behavior changing from pitting corrosion into serious uniform corrosion of AZ91D alloy.	[41]
1500-9	ECAE	Pure Mg	SBF	Decrease (As Cast to ECAE, and 250-200°C) - Increase (360-250oC)	ECAE Temp.	ECAE introduces high dislocation density into the microstructure of pure Mg, leading to more energetic crystalline defects in the Mg matrix. A MgO film or $Mg(HO)_2$ passive film is prone to nucleate at the surface defects of pure Mg crystals. Given the large number of energetic crystalline defects, ECAE-processed pure Mg has more nucleation sites for the formation of films	[40]
12.3-0.35	High Ratio Diff. Speed Rolling (HRDSR)	Pure Ti	0.5 M H_2SO_4 solution	Decreases (by forming UFG)-	High Ratio Differential Speed Rolling	1. UFG Ti, which was subjected to severe plastic deformation by HRDSR, exhibited good corrosion resistance compared to CG Ti. This achievement could be attributed to significant grain size reduction and basal texture strengthening obtained during the process. 2. After annealing, the corrosion resistance of the UFG Ti was further increased by a considerable amount. The analysis indicated that reduction of dislocation density and residual stress by annealing increased the corrosion resistance.	[148]
200-0.5	ECAP	Pure Al	0.01 mol/L sodium sulfate (Na_2SO_4) water solution containing 0.01% Cl^-.	Decreases (by forming UFG)-	ECAP (Room Temp.)	The more grain boundaries caused by finer grains, the large fraction of non-equilibrium grain boundaries and high residual stress furnish the UFG industrial pure Al more nucleus to form denser nature oxide film than ordinary CG counterpart. This denser oxide film can be kept relative integral in the aggressive solution and make the UFG sample exhibit better pitting resistance than CG counterpart.	[96]